AFRL-AFOSR-VA-TR-2020-0074

Control of Lagrangian Coherent Structures at Stagnation and Separation Locations on Airfoils

Geoff Spedding
UNIVERSITY OF SOUTHERN CALIFORNIA

12/27/2019
Final Report

Air Force Research Laboratory
AF Office Of Scientific Research (AFOSR)/ RTA1
Arlington, Virginia 22203
Air Force Materiel Command

DISTRIBUTION A: Distribution approved for public release.

REPORT DOCUMENTATION PAGE

Form Approved
OMB No. 0704-0188

1. REPORT DATE *(DD-MM-YYYY)*	2. REPORT TYPE	3. DATES COVERED *(From - To)*
30-06-2020	Final Performance	30 Sep 2016 to 29 Sep 2019

4. TITLE AND SUBTITLE
Control of Lagrangian Coherent Structures at Stagnation and Separation Locations on Airfoils

5a. CONTRACT NUMBER

5b. GRANT NUMBER
FA9550-16-1-0392

5c. PROGRAM ELEMENT NUMBER
61102F

6. AUTHOR(S)
Geoff Spedding

5d. PROJECT NUMBER

5e. TASK NUMBER

5f. WORK UNIT NUMBER

7. PERFORMING ORGANIZATION NAME(S) AND ADDRESS(ES)
UNIVERSITY OF SOUTHERN CALIFORNIA
3720 S FLOWER STREET, THIRD FLOOR
LOS ANGELES, CA 90007 US

8. PERFORMING ORGANIZATION REPORT NUMBER

9. SPONSORING/MONITORING AGENCY NAME(S) AND ADDRESS(ES)
AF Office of Scientific Research
875 N. Randolph St. Room 3112
Arlington, VA 22203

10. SPONSOR/MONITOR'S ACRONYM(S)
AFRL/AFOSR RTA1

11. SPONSOR/MONITOR'S REPORT NUMBER(S)
AFRL-AFOSR-VA-TR-2020-0074

12. DISTRIBUTION/AVAILABILITY STATEMENT
A DISTRIBUTION UNLIMITED: PB Public Release

13. SUPPLEMENTARY NOTES

14. ABSTRACT

A combined numerical, theoretical and experimental program was performed towards a rational control strategy for transitioning and/or separated flows. The model platform was the NACA 65(1)-412, a commonly used turbine blade section. Investigations were made for the basic flows and their stability, in experiment and computations. Studies were conducted in 2D and in 3D. Lagrangian flow descriptors in terms of Finite Time Lyapunov Exponent (FTLE) fields were made in 2D and in 3D, for the first time. The numerical data for pulse actuation of the base flow was used to determine optimal actuator placement, using a frequency-space formulation of a controllability Gramian to determine the most sensitive control regime. The optimal location for separation point and separation streamline angle control were different, as confirmed in the simulations. The separation control can be more closely linked with structures in an LCS-based reduced order model of surface information. DMD modes confirm that those for the two strategies differ in spatial arrangement. Significant computational and theoretical progress was made in examining spike formation in wall-bounded flows. We believe an exciting baseline has been established for explicit LCD-based mode control

15. SUBJECT TERMS
lagragian coherent structures, unsteady airfoil dynamics, LCS based flow control

16. SECURITY CLASSIFICATION OF:			17. LIMITATION OF ABSTRACT	18. NUMBER OF PAGES	19a. NAME OF RESPONSIBLE PERSON
a. REPORT	b. ABSTRACT	c. THIS PAGE			ABATE, GREGG
Unclassified	Unclassified	Unclassified	UU		

Standard Form 298 (Rev. 8/98)
Prescribed by ANSI Std. Z39.18

				19b. TELEPHONE NUMBER *(Include area code)* 703-588-1779

CONTROL OF LAGRANGIAN COHERENT STRUCTURES AT STAGNATION AND SEPARATION LOCATIONS ON AIRFOILS

Geoffrey Spedding, Professor
Department of Aerospace and Mechanical Engineering, University of Southern California

Gustaaf Jacobs, Professor
Department of Aerospace Engineering, San Diego State University

Maziar Hemati, Assistant Professor
Department of Aerospace Engineering and Mechanics, University of Minnesota

December 27, 2019

1 Introduction

1.1 Practical control on wings and airfoils

Flow separation can degrade performance in many engineering systems, through reduced lift, increased drag, and decreased efficiency. To alleviate the effects of flow separation on aerodynamic performance, active flow control has been considered since the inception of the field of aerodynamics [1, 2] and continues to be one of the premier challenges in modern aerodynamics. While classic flow control concepts work by completely removing or re-energizing the separated fluid through suction and blowing (see e.g. Schlichting [3]), more recent techniques take advantage of instabilities and non-linearities in the flow by using more compact zero-net mass flux (ZNMF) devices [4]—such as plasma actuators [5, 6, 7], fluidic oscillators [8, 9, 10, 11, 12], and synthetic jets [13, 14, 15, 16, 17, 18, 19, 20]. These have been shown to effectively alter separated flows, and in some cases to even yield complete reattachment. Oscillatory forcing has also been considered to improve control authority over separation. Actuation at domination frequencies in the shear layer [21, 22, 23, 24] or the separation bubble [25] have been shown to be effective. Nonlinear unsteady flow interactions can result in lock-on effects that influence the optimal forcing frequency [26, 27]. This lock-in can be leveraged to identify candidate actuation frequencies objectively using operator-based and data-driven modal analysis techniques—such as linear stability analysis, resolvent analysis, and dynamic mode decomposition (DMD) [23, 28, 29, 18, 30, 31].

1.2 Flow separation and new Lagrangian perspectives

To control unsteady flow separation requires first and foremost a comprehensive understanding of the intricate physics of separation [32, 33, 34], in itself another mature topic in the field of aerodynamics with many long-standing open questions. While for steady two-dimensional flows separation from a no-slip wall much is known, such as the exact separation location identified by Prandtl's condition through a point of zero skin friction and a negative friction gradient in wall-tangential direction, for unsteady flows, new discoveries continue to be made that radically change the way we think about control. A significant development for unsteady flow separation that inspired the current project, was made by Haller[35]. He derived criteria similar to Prandtl's first-principle criteria but for time periodic flow. Haller proved that an objective separation point can be found using Lagrangian analysis at the time averaged zero-skin-friction location, and then further showed that flow separation from a no-slip boundary starts with an upwelling of Lagrangian fluid tracers upstream of the separation point and that those particles are drawn towards an unstable manifold in the flow while they are ejected from the wall. This so-called asymptotic separation profile is anchored at the separation point and it guides fluid particles as they break away in the vicinity of the wall (see Haller [35] and Weldon *et al.* [36]).

To illustrate this Lagrangian separation behavior, we consider the time periodic flow over a circular cylinder in Figure 1. A set of fluid particle tracers is initialized in a layer parallel to the cylinder wall and is color-coded based on the linear approximation of the dividing asymptotic separation line. As the particles are advected, they undergo an upwelling motion, which is visible through an increasingly sharp spike in the material lines that are initially parallel to the wall. The spikes of particles are asymptotically drawn towards the attracting separation line. Mathematically, these attracting lines are interpreted as unstable manifolds.

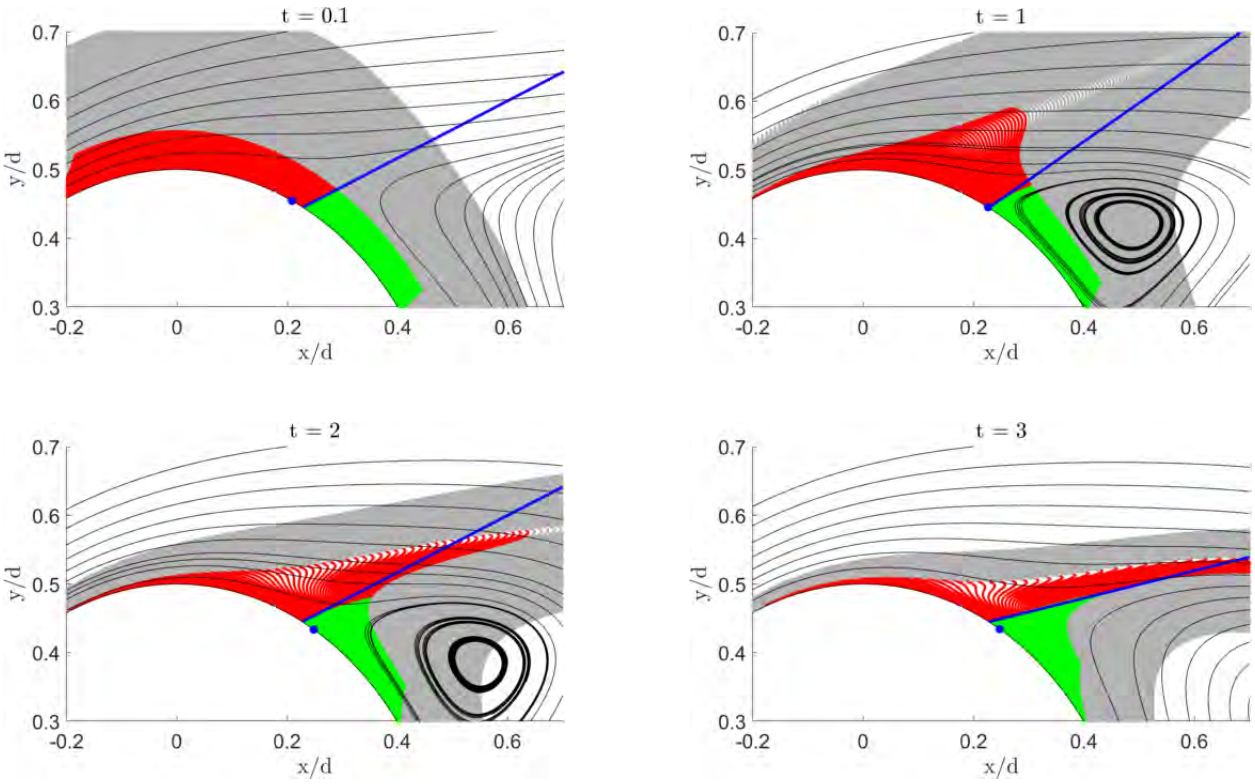

Figure 1: Advection of particles over a cylinder near the separation point. Particles divided by linear separation line (blue) in upstream (red) and downstream (green). Zero-skin-friction point in blue, streamlines in black.

In general, stable and unstable manifolds can be identified by extracting ridges in the Finite-Time Lyapunov Exponent (FTLE) fields. These FTLE fields are determined from the maximum deformations in flow maps that are in turn constructed from integrated particle tracer fields in forward and backward time, respectively. The ridges usually demarcate a hyperbolic Lagrangian Coherent Structure (LCS) [37, 38]. Although a hyperbolic Lagrangian Coherent Structure (LCS) can be identified through local maxima in the FTLE field, Haller [39] shows that the FTLE field has ridges in regions of high shear which are non-hyperbolic [40].

Even though hyperbolic LCS are mostly near zero-flux material lines [41], they fall short in the identification of the start of flow separation at the boundary wall. Because of the zero-velocity no-slip condition, the wall is naturally a set of *non*-hyperbolic fixed points. As a result, the backward time (attracting) FTLE cannot intersect the wall, but envelopes the aerodynamic body, as we show for the circular cylinder flow in Figure 2. The FTLE can, hence, only identify long-term attracting and repelling surfaces away from the wall rather than the onset of separation.

To understand separation we must hence use a combination of separation theory near the wall and FTLE theory away from the wall.

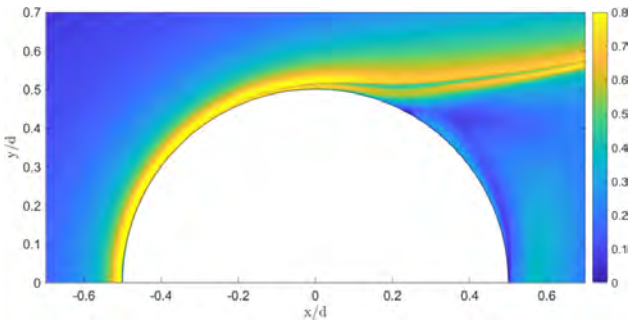

Figure 2: Backward-time FTLE around the upper half of a cylinder.

In this report, we identify distinct asymptotic upwelling events [42]. We also report on optimal controllers that turn out to closely correlate to these early upwellings before significant breakaway takes place.

1.3 A unique opportunity to validate experiment and computation for dynamically rich flows

Because of state-of-the-art of experimental and computational techniques and infrastructure we are at a unique point in time to understand details of unsteady flow separation that hitherto we have not had access to. It is only now that we can use a combination of first principle models and time-resolved, experimental data of the spatial flow fields to obtain high-resolution and high-fidelity time- and space-resolved data for flow separation around airfoils at Reynolds number range of the order 10^4. Coincidentally the flow physics at this Reynolds are dynamically rich combining many of the flow features one would see at much higher Reynolds numbers such a laminar boundary layer development, flow separation, separation bubbles, transition to turbulence, turbulent boundary layer development and turbulent wakes. Numerical simulations solve the Navier-Stokes equations, albeit on a discrete grid. No modelling is used, but convergence is required to obtain a solution that is not affected by numerical errors. If the flow solution is converged in space and time, then the velocity and pressure fields are known exactly throughout the flow field with full resolution. Because of the sensitivities of transitional flows, a high spatial resolution is required over large parts of the near-foil field, and calculations are expensive. By contrast, wind tunnel or water channels have analog Navier-Stokes solutions, but to problems whose specifications are not precisely known. If these can be made sufficiently close to the nominal (ideal) problem geometry, then systematic variations of the Reynolds number and geometry can reveal dependencies and extrapolate control strategies in an efficient way.

1.4 Objectives

The primary objective of this work was to investigate whether a rational local control strategy can be devised using new concepts in Lagrangian flow descriptors, state-of-art experimental and computational techniques, and reduced flow control models. Specifically, we focus on the following goals

1. Generation of a benchmark for cambered airfoils, chosen based on practical application in turbomachinery, at low to moderate Reynolds number, using a mutual validation of computation with first-principle models and accurate experiments.
2. Development of a fundamental understanding of flow instabilities and bifurcations for this benchmark over a range of angles of attack and Reynolds numbers.
3. Development of a fundamental understanding of Lagrangian flow separation dynamics in unsteady external aerodynamics.
4. Development of a data-driven approach to optimal flow control of Lagrangian structures.

The outcome of this work generates the necessary knowledge to develop and test active feedback controllers that can be implemented for a wide range of flow conditions and that can be extended to more complex geometries.

1.5 Approach: Lagrangian theory of separation, DNS, experiment and control

To accomplish these goals, we assembled a team with combined expertise in experimentation, numerical simulation, control theory and Lagrangian separation theory. Experiments and computations were conducted on the 65(1) series NACA airfoil by the PIs Geoffrey Spedding (GS) and Gustaaf Jacobs (GJ). In collaborative efforts with Mattia Serra (MS) from Harvard University, GJ investigated Lagrangian upwelling. Maziar Hemati (MH) investigated control theoretical aspects using high-fidelity data generated by GJ.

GJ used several codes that he has developed over the past twenty years. The codes are based on general high-order discontinuous spectral element methods for Direct Numerical Simulation (DNS) [43, 44, 45, 46, 47] and Large-Eddy Simulation (LES) [48, 49, 50, 51] of turbulent, wall-bounded flows in complex geometries. High-order discontinuous Galerkin (DG) methods [52, 53] are excellent candidates for DNS of flow separation: Because of their high order accuracy, DG methods require few degrees of freedom to resolve the delicate smallest scales of separation. Furthermore, small dispersion errors ensure the long-time accuracy of vortex dynamics. In addition to high accuracy, DG methods provide flexible meshing for complex geometries,

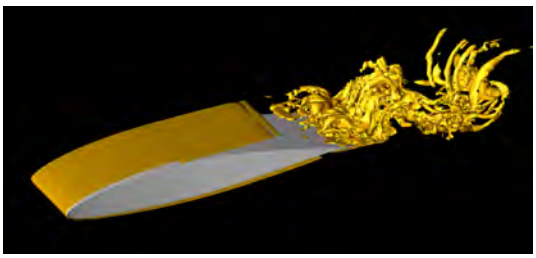

Figure 3: 3D DG-DNS of the flow over a NACA 64(5)-014 airfoil at $Re = 20,000$.

boundary fitted grids, and boundary conditions. An example of early 3D simulations of the NACA 64(5)-014 airfoil, available at the beginning of the project, is given in Fig. Figure 3.

Experiments were conducted on the same 65(1) series NACA airfoil as in the simulations. The tests exploit the availability of the Dryden Wind tunnel, a low-speed, low turbulence wind tunnel at USC ([54, 55], Fig 4(a)). At $U = 4$ m/s, the turbulence levels $T = q/U = 0.03\%$. A 7.5 cm wing chord yields a chord-based Reynolds number = 20,000, as used in initial simulations. Further increases in Re can be achieved up to 8x by increasing flow speed alone. As subsequent tests showed, a number of airfoil sizes were selected for optimal resolution either in direct force measurements, or in PIV-derived quantities. Further details on computations and experiments will be given in the report below.

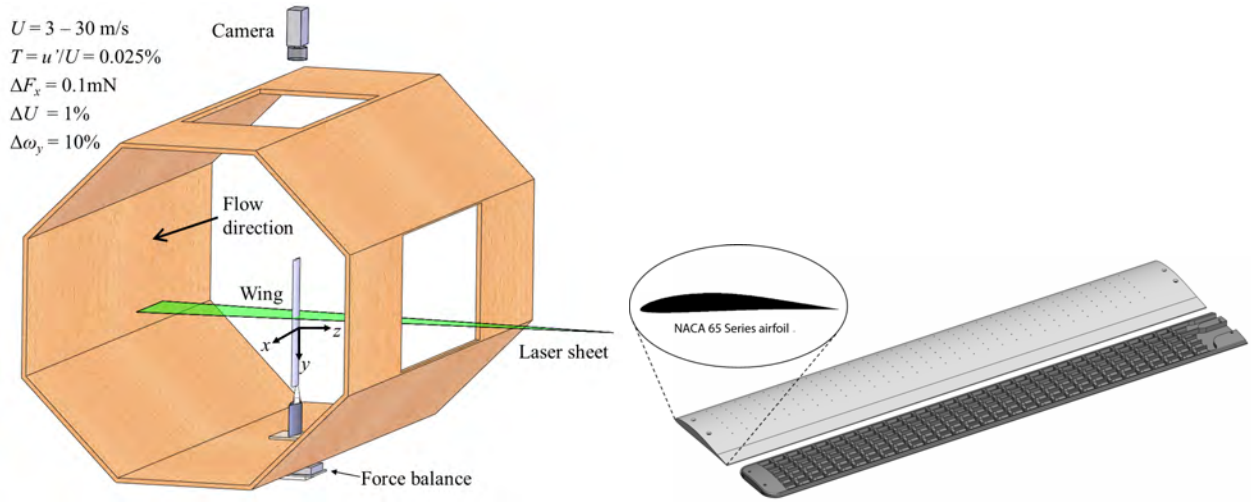

(a) (b)

Figure 4: (a) The Dryden wind tunnel setup, showing the standard PIV interrogation plane and tunnel statistics. (b) The grid of holes on the wing upper surface determines possible locations of sensors and actuators, all of which are located behind a small pinhole. The volume of the backing chamber must be selected to bring Helmholtz resonance away from the frequency range of interest.

We build on pioneering research on unsteady flow separation and Lagrangian dynamics (LCSs) that GJ has conducted in collaborative work [56, 57, 58, 59, 60, 61]. Prominently, GJ has published on the theory of a fixed Lagrangian separation location in time-periodic flows that enables the objective determination of the asymptotic separation location from first principles from a time history of wall velocity gradients and wall pressures. The theory, moreover, can estimate the time behavior of the near-wall separation material to arbitrary order. GJ also developed reduced models [62] to efficiently determine wall-based flow solutions. Another pillar of this project rests on the computational techniques GJ developed to efficiently determine FTLEs Lagrangian Structures [63, 64] with DG Navier–Stokes solvers [65]. GJ's work established the necessary elements for exploiting the LCS perspective for sensor-based feedback control of separation.

The ultimate control objective is to track a reference Lagrangian material line robustly and with good performance, using a feedback controller. Several technical considerations are central to these developments, including

- selection and placement of actuators and sensors
- model reduction on an aggregate system comprising the flow dynamics, actuator/sensor dynamics, Reduced Navier-Stokes (RNS) model, and LCS model
- robust and optimal control design from the reduced-order model
- controller implementation and performance assessment within numerical simulations and physical experiments

MH brought control theory expertise to this project and focused on development of theory for optimal actuator placement. As will be described in subsequent sections, the optimal selection of actuators and sensors is closely tied to the Lagrangian flow dynamics.

1.6 Contributions and report organization

The report is organized as follows. First, (§2) the Navier-Stokes governing equations and basic Lagrangian theory are presented for reference. Solution to the Navier-Stokes equation in discrete form using high-order methods are described in detail in §3. The details are important because, as we shall see, an accurate solution in this Reynolds number domain should be taken for granted in neither computational or experimental work. The experimental methods are described in §4. The first set of results from computations assess stability and accuracy of the method itself (§5), which is tested and demonstrated on some example geometries. In a similar vein, the experimental techniques and reliability were first demonstrated on an ostensibly simple example, and showed it not to be simple (§6). This sets the stage for an extensive combined experimental and computational study of the NACA65(5)-014 airfoil. Lift and drag polars between experiment and computation compare well, except for a shift in the critical angle where the flow transitions from a separated laminar flow to a flow with laminar to turbulent boundary layer transition by means of a separation bubble. We found several bifurcations in flow topology over a range of angles of attack and visualized them using Lagrangian techniques (§7). Lagrangian structures are visualized with dye in water tunnels. In computations, three-dimensional FTLE field over airfoils are generated for the first time and show a rich field of Lagrangian Structures that their genesis in the Lagrangian breakaway of fluid material from a a wall. Preliminary research into the effect of endwalls could explain a mismatch in critical angle of attack between experiment and computation. In section §8, we discuss progress made in the development of comprehensive Lagrangian separation theory and its application to external (airfoil) aerodynamics. Finite time curvature measures highlight early onset of separation that asymptotes towards a significant breakaway of fluid from the wall. Finally, in §9, we discuss techniques based on eigenvalue realization algorithms to identify optimal control location in a data-driven manner using computational results of the airfoil flow with pulse control.

2 Governing Equations

2.1 Conservation laws

We compute solutions to the compressible Navier-Stokes equations, which can be written in non-dimensional form as the system of equations

$$\partial_t \mathbf{U} + \nabla \cdot \mathbf{F} = 0. \tag{1}$$

In (1), $\mathbf{U}$ represents the vector of the conserved variables,

$$\mathbf{U} = \left[\, \rho \quad \rho u \quad \rho v \quad \rho w \quad \rho e \,\right]^T. \tag{2}$$

The flux vector $\mathbf{F}$ is split into an advective (superscript *a*) and a viscous part (superscript *v*),

$$\nabla \cdot \mathbf{F} = \partial_x \mathbf{F}^a + \partial_y \mathbf{G}^a + \partial_z \mathbf{H}^a - \frac{1}{Re_f}\left(\partial_x \mathbf{F}^v + \partial_y \mathbf{G}^v + \partial_z \mathbf{H}^v\right), \tag{3}$$

where

$$\begin{aligned}
\mathbf{F}^a &= \left[\, \rho u \quad p{+}\rho u^2 \quad \rho uv \quad \rho uw \quad u(\rho e{+}p) \,\right]^T, \\
\mathbf{G}^a &= \left[\, \rho v \quad \rho vu \quad p{+}\rho v^2 \quad \rho vw \quad v(\rho e{+}p) \,\right]^T, \\
\mathbf{H}^a &= \left[\, \rho w \quad \rho wu \quad \rho wv \quad p{+}\rho w^2 \quad w(\rho e{+}p) \,\right]^T,
\end{aligned} \tag{4}$$

$$\begin{aligned}
\mathbf{F}^v &= \left[0 \quad \tau_{xx} \quad \tau_{yx} \quad \tau_{zx} \quad u\tau_{xx}{+}v\tau_{yx}{+}w\tau_{zx}{+}\frac{\kappa}{(\gamma-1)\,PrM_f^2}T_x \right]^T, \\
\mathbf{G}^v &= \left[0 \quad \tau_{xy} \quad \tau_{yy} \quad \tau_{zy} \quad u\tau_{xy}{+}v\tau_{yy}{+}w\tau_{zy}{+}\frac{\kappa}{(\gamma-1)\,PrM_f^2}T_y \right]^T, \\
\mathbf{H}^v &= \left[0 \quad \tau_{xz} \quad \tau_{yz} \quad \tau_{zz} \quad u\tau_{xz}{+}v\tau_{yz}{+}w\tau_{zz}{+}\frac{\kappa}{(\gamma-1)\,PrM_f^2}T_z \right]^T.
\end{aligned} \tag{5}$$

ρ, u, v, w, p, and T are the density, velocities, pressure, and temperature respectively. The specific total energy is $\rho e = p/(\gamma-1) + \frac{1}{2}\rho(u^2+v^2+w^2)$ and the system is closed by the equation of state,

$$p = \frac{\rho T}{\gamma M_f^2}. \tag{6}$$

All quantities are non-dimensionalized with respect to a problem specific reference length, velocity, density, and temperature yielding the non-dimensional Reynolds number, Re_f and Mach number, M_f.

2.2 Finite-Time Lyapunov Exponent

We extract structures and patterns from flow field data using a Finite-Time Lyapunov Exponent contour field [41]. The FTLE, which characterizes the maximal stretching of infinitesimal fluid volumes over a given time interval, is determined by tracing fluid particles over time and subsequently computing the deformation tensor induced by the flow map.

We express the particle trajectories as

$$\mathbf{x}\left(\mathbf{x}_0, t_0; T\right) = \mathbf{x}_0 + \int_{t_0}^{t_0+T} \mathbf{v}\left(\mathbf{x}\left(\tau; \mathbf{x}_0, t_0\right), \tau\right) d\tau, \tag{7}$$

from which the flow map $\mathbf{F}$ is defined:

$$\mathbf{F}_{t_0}^{t}\left(\mathbf{x_0}, t_0; T\right) \equiv \mathbf{x}\left(\mathbf{x}_0, t_0; T\right). \tag{8}$$

From the deformation gradient tensor $\nabla \mathbf{F}_{t_0}^{t}$, the right Cauchy-Green strain tensor $\mathbf{C}_{t_0}^{t} = [\nabla \mathbf{F}_{t_0}^{t}]^{*} \nabla \mathbf{F}_{t_0}^{t}$ can be used to compute the strain in the Lagrangian frame. With the largest eigenvalue of the strain tensor $\lambda_2\left(\mathbf{C}_{t_0}^{t}(\mathbf{x}_0)\right)$, the finite-time Lyapunov exponent field is defined as

$$\Lambda_{t_0}^{t}(\mathbf{x}_0) = \frac{1}{|t - t_0|} \ln \sqrt{\lambda_2(\mathbf{x}_0)}. \tag{9}$$

This FTLE identifies the highest Lagrangian rate of stretching in the flow field. Tracing fluid particles forward or backward in time, ridges of the FTLE field can be used to identify hyperbolic repelling and attracting Lagrangian coherent structures (see Haller [37, 39], and Nelson and Jacobs [66] for a more detailed description).

2.3 Separation point and angle

Haller [35] shows that for flows with an asymptotic mean, such as periodic flows, the asymptotic separation point γ is located at the integrated zero-skin-friction point

$$\frac{1}{t_1 - t_0} \int_{t_0}^{t_1} c_f\left(\gamma, t\right) dt = 0. \tag{10}$$

He further derives an analytic expression for the separation profile which is a wall-bounded unsteady manifold along which fluid particles are ejected from the wall into the free-stream. The slope, or separation angle, of this line can be computed just by evaluating integrated values of the pressure and skin friction data at the wall:

$$\tan\left(\alpha\left(t_0\right)\right) = -\lim_{T \to -\infty} \frac{3 \int_{t_0}^{T} \tau_x\left(\gamma, t\right) dt}{\int_{t_0}^{T} \left[p_x\left(\gamma, y_w, t\right) + 3\tau_x\left(\gamma, t\right) \int_{t_0}^{t} \frac{1}{\mu} \tau\left(\gamma, s\right) ds\right] dt}. \tag{11}$$

Here, the *x* coordinate refers to wall tangential direction and *y* points in wall-normal direction. The separation angle α is the angle to the tangent of the wall at the separation point. Using both, the separation point and the separation angle, a linear approximation of the separation profile can be constructed.

3 Numerical Method

We approximate the system, (1), with a discontinuous Galerkin spectral element method (DGSEM). Details can be found in [67, 68] and we only provide a short summary here.

The physical domain is subdivided into hexahedral elements, each of which is mapped from the reference element, $E = [-1, 1]^3$ by a transformation $\vec{x} = \vec{X}\left(\xi, \eta, \zeta\right)$. Under the transformation, the reference space equations become

$$\tilde{\mathbf{U}}_t + \nabla_\xi \cdot \tilde{\mathbf{F}} = 0, \tag{12}$$

where $\tilde{\mathbf{U}} = J\mathbf{U}$, J is the transformation Jacobian, and $\tilde{\mathbf{F}}$ is the contravariant flux.

The DGSEM approximates the conserved variables and the contravariant fluxes as polynomials of arbitrary order *N* within each element. We approximate the vector $\tilde{\mathbf{U}}$ as

$$\tilde{\mathbf{U}}_N = \sum_{i=0}^{N} \sum_{j=0}^{N} \sum_{k=0}^{N} \left(\tilde{\mathbf{U}}_N\right)_{i,j,k} \ell_i(\xi) \ell_j(\eta) \ell_k(\zeta), \tag{13}$$

where the Lagrange interpolating polynomials, $\ell_i(\xi)$ are

$$\ell_i(\xi) = \prod_{\substack{n=0 \\ n\neq i}}^{N} \frac{\xi - \xi_n}{\xi_i - \xi_n}, \tag{14}$$

and similarly for $\ell_j(\eta)$ and $\ell_k(\zeta)$. The nodes ξ_i, η_j, and ζ_k are chosen to be the nodes of a Gauss quadrature.

Weak formulation

The approximation satisfies a weak form the conservation law, constructed by taking the inner product of (12) with a test function ϕ,

$$\int_E \left(\partial_t \tilde{\mathbf{U}} + \nabla \cdot \tilde{\mathbf{F}}\right) \phi \, \mathrm{d}\xi = 0, \tag{15}$$

and integrating by parts

$$\int_E \partial_t \tilde{\mathbf{U}} \phi \, \mathrm{d}\xi + \int_{\partial E} \tilde{\mathbf{F}} \cdot \mathbf{n} \phi \, \mathrm{d}S - \int_E \tilde{\mathbf{F}} \cdot \nabla \phi \, \mathrm{d}\xi = 0. \tag{16}$$

DG approximations do not require the solution to be continuous at the interface, and elements are coupled through the boundary flux in (16). For the majority of the simulations in this report, we use formulation where we replace $\tilde{\mathbf{F}}$ with a numerical flux $\tilde{\mathbf{F}}^*\left(\tilde{\mathbf{U}}^L, \tilde{\mathbf{U}}^R\right)$, which depends only on the solutions on the left and right of the interface between two elements, and is computed through a Riemann solver, e.g. the upwinding scheme by Roe [69].

The integrals in (16) are approximated with a Gauss quadrature of $N+1$ nodes, and two choices have been commonly used. The first is the Legendre-Gauss (LG) quadrature, which approximates the integral exactly for polynomial integrands of order $2N+1$ or less, but whose nodes do not include endpoints. The second is the Legendre-Gauss-Lobatto (LGL) quadrature, whose nodes include endpoints, but is only exact for polynomial integrands of order $2N-1$ or less. For a more detailed discussion of the differences between LG and LGL quadrature we refer to Gassner & Kopriva [70].

By replacing the integrals in (16) with quadrature, and choosing $\phi = \ell_i(\xi)\ell_j(\eta)\ell_k(\zeta)$, the flux derivatives for the Gauss-Lobatto version become

$$\begin{aligned}
\partial_\xi \tilde{\mathbf{F}}\Big|_{ijk} &\approx \left(\delta_{iN}\tilde{\mathbf{F}}^*_{Njk} - \delta_{i0}\tilde{\mathbf{F}}^*_{0jk}\right) + \sum_{m=0}^{N} \hat{D}_{im}\tilde{\mathbf{F}}_{mjk}, \\
\partial_\eta \tilde{\mathbf{G}}\Big|_{ijk} &\approx \left(\delta_{jN}\tilde{\mathbf{G}}^*_{iNk} - \delta_{j0}\tilde{\mathbf{G}}^*_{i0k}\right) + \sum_{m=0}^{N} \hat{D}_{jm}\tilde{\mathbf{G}}_{imk}, \\
\partial_\zeta \tilde{\mathbf{H}}\Big|_{ijk} &\approx \left(\delta_{kN}\tilde{\mathbf{H}}^*_{ijN} - \delta_{k0}\tilde{\mathbf{H}}^*_{ij0}\right) + \sum_{m=0}^{N} \hat{D}_{km}\tilde{\mathbf{H}}_{ijm},
\end{aligned} \tag{17}$$

where $\hat{D}_{ij} = -D_{ji}w_j/w_i$ and $D_{ij} = \ell_j'(\xi_i), i,j = 0,\ldots,N$ is the derivative matrix.

Formulations in strong and split form

Integrating (16) by parts one more time lets us rewrite (16) in what is known as the strong form

$$\int_E \partial_t \tilde{\mathbf{U}} \phi \, \mathrm{d}\xi + \int_{\partial E} \left(\tilde{\mathbf{F}}^* - \tilde{\mathbf{F}}\right) \cdot \mathbf{n} \phi \, \mathrm{d}S + \int_E \nabla \cdot \tilde{\mathbf{F}} \phi \, \mathrm{d}\xi = 0. \tag{18}$$

Again, we replace the integrals with quadrature and choose $\phi = \ell_i(\xi)\ell_j(\eta)\ell_k(\zeta)$, so that for the Gauss-Lobatto version the flux derivatives in (18) become [67]

$$\begin{aligned}
\partial_\xi \tilde{\mathbf{F}}\Big|_{ijk} &\approx \left(\delta_{iN}\left[\tilde{\mathbf{F}}^* - \tilde{\mathbf{F}}\right]_{Njk} - \delta_{i0}\left[\tilde{\mathbf{F}}^* - \tilde{\mathbf{F}}\right]_{0jk}\right) + \sum_{m=0}^{N} D_{im}\tilde{\mathbf{F}}_{mjk}, \\
\partial_\eta \tilde{\mathbf{G}}\Big|_{ijk} &\approx \left(\delta_{jN}\left[\tilde{\mathbf{G}}^* - \tilde{\mathbf{G}}\right]_{iNk} - \delta_{j0}\left[\tilde{\mathbf{G}}^* - \tilde{\mathbf{G}}\right]_{i0k}\right) + \sum_{m=0}^{N} D_{jm}\tilde{\mathbf{G}}_{imk}, \\
\partial_\zeta \tilde{\mathbf{H}}\Big|_{ijk} &\approx \left(\delta_{kN}\left[\tilde{\mathbf{H}}^* - \tilde{\mathbf{H}}\right]_{ijN} - \delta_{k0}\left[\tilde{\mathbf{H}}^* - \tilde{\mathbf{H}}\right]_{ij0}\right) + \sum_{m=0}^{N} D_{km}\tilde{\mathbf{H}}_{ijm},
\end{aligned} \tag{19}$$

where $D_{ij} = \ell'_j(\xi_i), i, j = 0, \ldots, N$ is the derivative matrix. Note that the forms (17) and (19) are algebraically equivalent [71].

The non-linearity of the inviscid Euler fluxes introduces aliasing errors when the fluxes are approximated by polynomials, which can lead to instability. Gassner and collaborators [72, 68] showed that through the SPB property of the derivative operator when using the LGL points, the volume term contributions in (19) can be rewritten as

$$\begin{aligned}
\partial_\xi \tilde{\mathbf{F}}\Big|_{ijk} &\approx \left(\delta_{iN}\left[\tilde{\mathbf{F}}^* - \tilde{\mathbf{F}}\right]_{Njk} - \delta_{i0}\left[\tilde{\mathbf{F}}^* - \tilde{\mathbf{F}}\right]_{0jk}\right) + 2\sum_{m=0}^{N} D_{im}\tilde{\mathbf{F}}^{\#}_{(i,m),j,k}, \\
\partial_\eta \tilde{\mathbf{G}}\Big|_{ijk} &\approx \left(\delta_{jN}\left[\tilde{\mathbf{G}}^* - \tilde{\mathbf{G}}\right]_{iNk} - \delta_{j0}\left[\tilde{\mathbf{G}}^* - \tilde{\mathbf{G}}\right]_{i0k}\right) + 2\sum_{m=0}^{N} D_{jm}\tilde{\mathbf{G}}^{\#}_{i,(j,m),k}, \\
\partial_\eta \tilde{\mathbf{H}}\Big|_{ijk} &\approx \left(\delta_{kN}\left[\tilde{\mathbf{H}}^* - \tilde{\mathbf{H}}\right]_{ijN} - \delta_{k0}\left[\tilde{\mathbf{H}}^* - \tilde{\mathbf{H}}\right]_{ij0}\right) + 2\sum_{m=0}^{N} D_{km}\tilde{\mathbf{H}}^{\#}_{i,j,(k,m)}.
\end{aligned} \tag{20}$$

so that the scheme becomes entropy or energy conserving, depending on the choice of the new two-point fluxes $\mathbf{F}^{a,\#}$, $\mathbf{G}^{a,\#}$, and $\mathbf{H}^{a,\#}$, and the numerical surface fluxes. In this project, we have tested the kinetic energy conserving split form by Pirozzoli [73] for simulation of airfoil flows and found that it aids in the stable computation of the flow with marginal resolution. The split form is given as follows

$$\mathbf{F}^{a,\#} = \begin{bmatrix} \{\{\rho\}\}\{\{u\}\} \\ \{\{\rho\}\}\{\{u\}\}^2 + \{\{p\}\} \\ \{\{\rho\}\}\{\{u\}\}\{\{v\}\} \\ \{\{\rho\}\}\{\{u\}\}\{\{w\}\} \\ \{\{\rho\}\}\{\{u\}\}\{\{h\}\} \end{bmatrix}, \quad \mathbf{G}^{a,\#} = \begin{bmatrix} \{\{\rho\}\}\{\{v\}\} \\ \{\{\rho\}\}\{\{u\}\}\{\{v\}\} \\ \{\{\rho\}\}\{\{v\}\}^2 + \{\{p\}\} \\ \{\{\rho\}\}\{\{v\}\}\{\{w\}\} \\ \{\{\rho\}\}\{\{v\}\}\{\{h\}\} \end{bmatrix}, \quad .\mathbf{H}^{a,\#} = \begin{bmatrix} \{\{\rho\}\}\{\{w\}\} \\ \{\{\rho\}\}\{\{u\}\}\{\{w\}\} \\ \{\{\rho\}\}\{\{v\}\}\{\{w\}\} \\ \{\{\rho\}\}\{\{w\}\}^2 + \{\{p\}\} \\ \{\{\rho\}\}\{\{w\}\}\{\{h\}\} \end{bmatrix}, \tag{21}$$

with the notation $\{\{a\}\}_{im} := \frac{1}{2}(a_i + a_m)$.

The viscous stresses are computed in the standard formulation $\mathbf{F}^{v,\#} = \{\{\mathbf{F}^v\}\}$, $\mathbf{G}^{v,\#} = \{\{\mathbf{G}^v\}\}$, and $\mathbf{H}^{v,\#} = \{\{\mathbf{H}^v\}\}$ and the total fluxes are $\mathbf{F}^{\#} = \mathbf{F}^{a,\#} - \mathbf{F}^{v,\#}$, with the contravariant forms follow from $\tilde{\mathbf{F}}^{\#} = \left[\mathbf{F}^{\#}, \mathbf{G}^{\#}, \mathbf{H}^{\#}\right] \cdot \nabla\xi$, see [67, 68]. Formulations for $\tilde{\mathbf{G}}^{\#}$ and $\tilde{\mathbf{H}}^{\#}$ are obtained similarly.

To advance the solution in time, the system of equations (1) is integrated with an explicit low-dispersion 5-stage 4th-order Runge-Kutta scheme.

4 Experimental methods

4.1 Wind tunnel experiments

4.1.1 Models and wind tunnel

A series of models was constructed for force balance and/or PIV data in the wind tunnel. The models were sized for the resolution of the force balance, and PIV models were sometimes over-sized for improved spatial resolution. The wings were milled from solid aluminum on a CNC mill with a precision of 0.0127 mm. They were all then polished and painted. The NACA 0012 had a chord, $c = 7.5$ cm and span, $b = 48$ cm, for an aspect ratio $AR = b/c = 6.4$. The NACA 65-412 model used in the PIV tests had $c = 0.075$ m and $b = 0.225$ m, for $AR = 3$. Force balance tests were carried out using the $AR = 3$ model and an $AR = 12.9$ model ($c = 0.055$ m, $b = 0.71$ m). Note that AR varies between 12.9 and 3. In the two-dimensional tests, AR is not an explicit parameter, but end effects of some kind are always present, and will need to accounted for in subsequent results.

Tests were carried out in the closed loop Dryden Wind Tunnel at the University of Southern California. The tunnel has a contraction ratio of 8:1 and an octagonal test section measuring 1.37 m wall to wall. Given the small model size in comparison with the tunnel cross section, blockage effects were ignored. Twelve screens reduced the turbulence levels ($T = q/U$, where $q = \sqrt{u^2 + v^2 + w^2}$ in the test section to less than 0.03% for frequencies between 2 and 200 Hz over the speed range of 5 – 26 m/s [74, 75].

For two-dimensional tests, an infinite aspect ratio was approximated by placing endplates at either tip of the wing. The endplates were aligned carefully, parallel with the flow, and were kept within about 1 mm of the tip. This is within the separation distance of $0.005b$ (2.4 mm) recommended by [76], and less than the laminar boundary layer thickness on the plates themselves, $\delta = 5.2x/Re^{\frac{1}{2}} = 2.7$ mm.

4.1.2 Force balance

Force balance measurements were performed with a custom, three-component, cruciform-shaped force balance with a parallel plate sandwich design [54]. A new static calibration was performed before each test, generating a 3x4 calibration matrix. The three most recent matrices were averaged to generate the final calibration matrix used during the test. Considerable care was taken to assure that sensitivities of estimated drag to off-diagonal terms in the calibration matrix were correctly controlled. The uncertainty of lift and drag measurements is estimated to be less than 8 mN, which is 0.13 of the minimum expected drag force on this sized model.

Lift and drag measurements were zeroed with forces corresponding to the empty sting, the weight of the model, and free stream flow interaction with the sting. Because the sting was shielded by a shroud, the free stream flow interaction component was generally less than 5 mN. For three dimensional tests, the model support rod was also exposed to the air flow. To account for this, the drag force on a matching rod was also measured and subtracted from the test results.

Each force balance test consisted of five sweeps, forward and backward, through an angle of attack range of $-5^\circ \leq \alpha \leq 9^\circ$ in increments of 0.5°. After each step, the flow was allowed to settle for ten seconds before ten seconds of data were collected at 1 kHz and averaged. The five sweeps produced ten measurements for each α which were averaged to yield a single value. The uncertainty of each resulting force value was taken as the standard deviation of the ten averages. The entire test procedure was repeated for the two dimensional and three dimensional configurations at each Re until three consecutive datasets gave the same drag coefficient values within the uncertainty limits. In this case of a symmetric model, curves were shifted by small offsets (less than 0.3°) to ensure zero net lift force at zero α. Close to stall, the model begins to oscillate considerably, so measurements were not taken post stall.

4.1.3 PIV measurements

Particle Image Velocimetry (PIV) tests were carried out for $0^\circ \leq \alpha \leq 8^\circ$. The tunnel was filled with glycerin-based smoke with a typical particle diameter of 0.2-0.3 μm and a laser sheet parallel to the flow direction (in x, z) was generated by a Quantel EverGreen double-pulsed Nd:YAG laser. An Image Pro X 2M CCD camera (1600 x 1200 pixel, 14 bit) imaged particle fields on a cross-section 2.5 cm ($0.05b$) above mid span in x, z with a Nikon 70 – 210 mm f/4-5.6 NIKKOR AF lens. For the symmetric NACA 0012, the suction and pressure sides were illuminated by rotating the model in positive and negative α. To increase spatial resolution, the flow field on each side of the airfoil was split into two, slightly overlapping sub-regions that were imaged in separate experiments. For the 65-412, the flow field was split into either five (for $\alpha = [0^\circ, 2^\circ, 4^\circ, 6^\circ, 8^\circ, 10^\circ]$) or two (for $\alpha = [10^\circ, 10.1^\circ, 10.2^\circ, 10.3^\circ, 10.4^\circ, 10.5^\circ]$) overlapping sub-regions. When two sub-regions are used, they correspond to the forward and the aft sections of the suction side of the airfoil. When five sub-regions are used, they correspond to the forward and aft sections of both the suction and the pressure sides of the airfoil, and the wake.

200 image pairs were captured for each sub-region at a sample rate of 9.6 Hz, and the time delay between images in an image pair ($\delta t = 8\mu s - 30\mu s$) was tuned to maximize the dynamic range of observable displacements while minimizing peak locking errors and at the same time reducing otherwise untrackable shear deformations of correlation boxes inside the separation bubble. The images were processed with the LaVision DaVis software to produce velocity field estimates u, w in the streamwise and vertical directions x, z, on a uniform grid using a multi-pass algorithm, with initial 64 x 64 pixel interrogation windows reducing to 16 x 16 pixels by the final pass. A 50% overlap gave a final spatial resolution of 8 pixels, which is 0.27 mm, or $0.0036c$.

All 200 instantaneous velocity fields were averaged to produce one time-averaged velocity field for each sub-region. A built in Matlab thin-plate smoothing spline with a single smoothing parameter, similar to the spline used in [**?**], was applied to the averaged results in order to reduce the random noise component. The average change in either velocity component in a sub-region due to smoothing was always less than 0.4% of the maximum value of that component in the sub-region. The spanwise component of vorticity, $\omega_y = \partial w/\partial x - \partial u/\partial z$ was calculated at each grid location from the derivatives of the smoothing spline coefficients. All four averaged and smoothed sub-region velocity and vorticity fields were finally stitched together to form one composite velocity/vorticity field, on both sides of the airfoil, for each α.

4.2 Water channel flow visualization

Dye-injection flow visualization tests were carried out on a scaled model in the USC water channel (BWC) which has a rectangular test section (L,W,H = 762, 89, 61 cm). Free stream velocity data were collected during tests with a MSE 2D miniLDV laser Doppler velocimeter, and $T < 1.7\%$ for all tests. The airfoil model was made of clear acrylic with $c = 14.4$ cm, $b = 45$ cm ($AR = 3.1$). This AR is sufficient to generate a largely two dimensional flow at the mid-span location when tip vortices are blocked by the bottom of the channel at one end and an endplate positioned just beneath the free surface. Dye was injected from a leading edge exit port at $y/b = 0$ and/or at various offset (in x, z) locations

upstream. Dye materials were milk and alcohol (mixed for neutral buoyancy) or fluorescein/rhodamine complexes. A 5.14 W, 532 nm wavelength CNI continuous wave laser was spread into a sheet in an (x, z)-plane and aligned in the y-direction with the injection location to illuminate the dye. A Mako U-130 camera (1280 X 1024 pixel, 10 bit) with an Edmund Optics 25 mm C series fixed focal length lens collected images at a frame rate of 20 fps from below the model through a window in the bottom of the channel. For $Re = 2 \times 10^4, U = 14$ cm/s, and a convection time c/U is on the order of 1 s, so sampling 2 orders of magnitude faster can be considered time-resolved. The second advantage of dye visualization is that fine scale features can be observed and traced that are lost in an average PIV correlation box.

4.3 Vortex shedding frequency

Flow visualization image sequences of the airfoil wake ($1 \leq x/c \leq 2$) were analyzed to estimate the shedding frequency as a function of α. Dye injected into the boundary layer marks the vortex structures originating at the surface, so image sequences were analyzed to determine how often patches of dye passed through the wake observation window. This was done by selecting a grid of pixels (20 X 20 pixel) from an interrogation box in the wake images and determining their intensity as a function of time. A Fourier transform was then used to generate an amplitude spectrum for each pixel, and the spectra from all pixels on the grid were averaged to determine the dominant frequencies in the wake. This method produced sharp, distinct peaks at low α, where vortices could be clearly identified, but less distinct peaks at the higher α, where the wake became more turbulent, leading to the diffusion of the dye streaks. When there was no obvious dominant frequency for a particular image set, or when the dominant frequency would change with the location of the interrogation box, that image set was discarded.

5 Assessing Standard and Kinetic Energy Conserving for Marginally Resolved DNS

In the this section, we summarize the assessment of of numerical stability and accuracy of the standard DGSEM and a kinetic energy conserving split form for simulation of the chambered airfoil. Results of the inviscid Taylor-Green vortex and the viscous flow over a NACA 65(1)-412 airfoil are simulated using the standard DGSEM, which supports both Legendre-Gauss (LG) and Legendre-Gauss-Lobatto (LGL) nodes, and the kinetic energy conserving formulation of the split form (SF) with LGL points. The split form allows for simulation with a marginal resolution, thereby saving computational effort to obtain DNS results. A paper has been submitted to *Computers & Fluids* [77].

5.1 Taylor-Green Vortex

The implementation of the kinetic-energy preserving inviscid fluxes into the DGSEM code is verified with the inviscid Taylor-Green vortex in three dimensions, as it has been done by Gassner *et al.* [72]. 16^3 elements are used in combination with a uniform polynomial order of $N = 3$. The kinetic energy $k = (u^2 + v^2 + w^2)/2$ is integrated over the domain at each time step and plotted in Figure 5. Two cases are considered: the standard form using LG nodes and the split form with LGL nodes, where the interface fluxes are computed with an upwinding Roe solver (Roe), a central Lax-Friedrichs solver with a stabilization term (LxF), and a central Riemann solver without dissipation (Central).

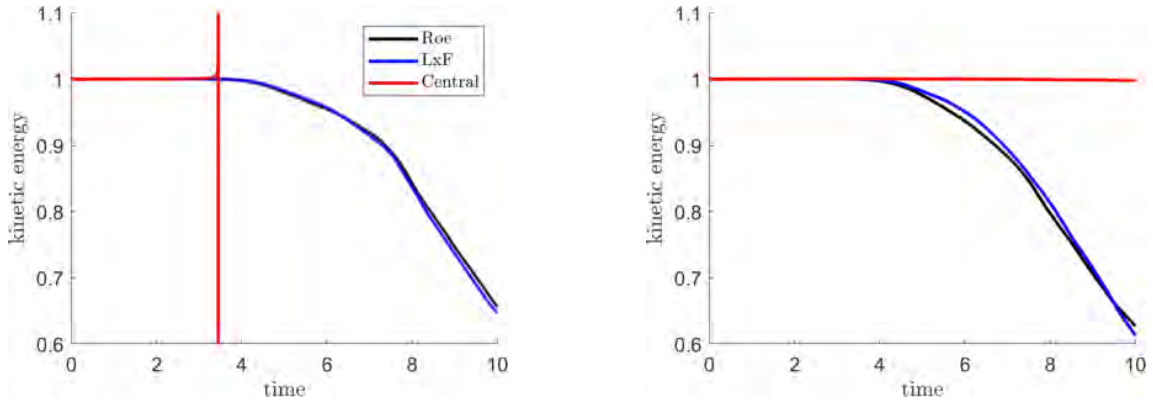

Figure 5: Integrated kinetic energy over time of the Taylor-Green vortex in 3D with different Riemann solvers (Roe, Lax-Friedrichs (LxF), Central without dissipation). (a) Standard form with LG nodes. (b) Split form with LGL nodes.

Table 1: Aerodynamic data of airfoil flows at different polynomial orders.

Node type	Flux method	N	C_l	C_d	St
LG	Standard	3	0.457	0.0530	3.37
LGL	Standard	3	-	-	-
LGL	Split form	3	0.405	0.0732	2.30
LG	Standard	6	0.445	0.0561	2.69
LGL	Standard	6	0.415	0.0560	2.59
LGL	Split form	6	0.440	0.0565	2.75
LG	Standard	12	0.442	0.0552	2.78
LGL	Standard	12	0.442	0.0554	2.78
LGL	Split form	12	0.442	0.0554	2.78

The kinetic energy as a function of time is shown in Figure 5. As expected, the standard form without dissipation at the interfaces is unstable. Upwinding or dissipative schemes are stable for this problem, but decrease the total kinetic energy with time (Fig. 5a). The split form approximation conserves the kinetic energy if a central Riemann solver without stabilization terms is used, while the Roe and Lax-Fiedrichs solvers add numerical viscosity and decrease the total kinetic energy (Fig. 5b), just as in the standard form. It should be noted that the split form approximation is not unconditionally stable, as the same test case crashes at higher polynomial orders [72]. In the following test problems, the upwinding Riemann solver of Roe is used.

5.2 Two-dimensional airfoil flow

The flow over a NACA 65(1)-412 airfoil is simulated at a Reynolds number based on the chord length of Re_c = 20,000 and a Mach number of M = 0.3. The airfoil is at 4° incidence.

The computational domain consists of 2,256 quadrilateral elements, where the boundaries are curved and fitted to a spline representing the airfoil's surface as described by Nelson *et al.* [78]. The outer boundaries of the domain are defined as free-stream boundaries while the airfoil surface is treated as a non-slip, adiabatic wall. Polynomial orders of N = [3, 6, 12] are used in all elements, where N = 12 has been found to give a grid converged solution. A more detailed description of the base flow is given by Nelson [78] and Klose *et al.* [79]. All computations are run until quasi-steady state is reached, and statistics are computed over 10 convective time units.

The vorticity plot in Figure 6 shows that the boundary layer separates mid-cord, enclosing a recirculation region on the airfoil's upper side. Periodic shedding of vortices lead to the formation of a Von-Karmann type vortex street in the wake.

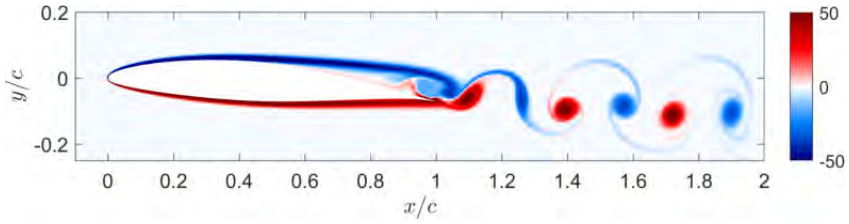

Figure 6: Instantaneous vorticity contours of flow over NACA 65(1)-412.

The averaged lift and drag coefficients, as well as the Strouhal numbers are summarized in Table 1. For a polynomial order of N = 12, the averaged lift and drag coefficients are $\bar{C}_l$ = 0.442 for both LG and LGL-SF schemes and $\bar{C}_d$ = 0.0552 for the standard form with Gauss points and $\bar{C}_d$ = 0.0554 for the split form, resulting in a relative difference of <0.4%. The Strouhal number based on the frequency of the lift coefficient is consistently at St = 2.78 for all cases. The fact that no significant difference between the LG and LGL results are found is in accordance with the findings by Nelson *et al.*, who reported convergence for a polynomial order of N = 12 using LG points [78].

To evaluate the performance on under-resolved computations, we decrease the polynomial order to N = 6 and N = 3 and compare the results to the reference solution at N = 12. At a polynomial order of N = 3, the methods using Gauss-Lobatto quadrature nodes perform rather poorly, as the standard form is numerically unstable and the split form largely overestimates the drag (33%, Tab. 1). Results obtained from the standard LG form are closer to the converged solution (<4%), with the exception of the Strouhal number (21% over-estimated).

As expected, increasing the polynomial order to $N = 6$ considerably improves the quality of the results. The differences in the lift coefficient and Strouhal number of the split form are now below 1% and only the drag is slightly over-estimated by about 2%. The standard LG form matches lift and drag closely, but has a frequency error of 3% with a spurious low-frequency component in the lift and drag force (Fig. 7). The standard form using LGL nodes gives the poorest results with larger errors in the lift and Strouhal number.

Overall, the results show that for the marginally resolved airfoil flow at $N = 6$, the split form yields the best results with the lift coefficient and Strouhal number matching the converged solution closely and only slightly larger deviations in the drag as compared to the standard DG scheme. For strongly under-resolved flows, the standard formulation with LG nodes is advantageous, as the errors in lift and drag coefficients are much smaller than for simulations using LGL nodes. Again, this result is expected, as the Gauss-Lobatto quadrature underintegrates and thus is less accurate. The favorable dispersion relation of the Gauss-Lobatto nodes, as shown by Gassner and Kopriva [70], also gives a reasonable explanation for the better representation of the Strouhal number for under-resolved cases when using the LGL split form.

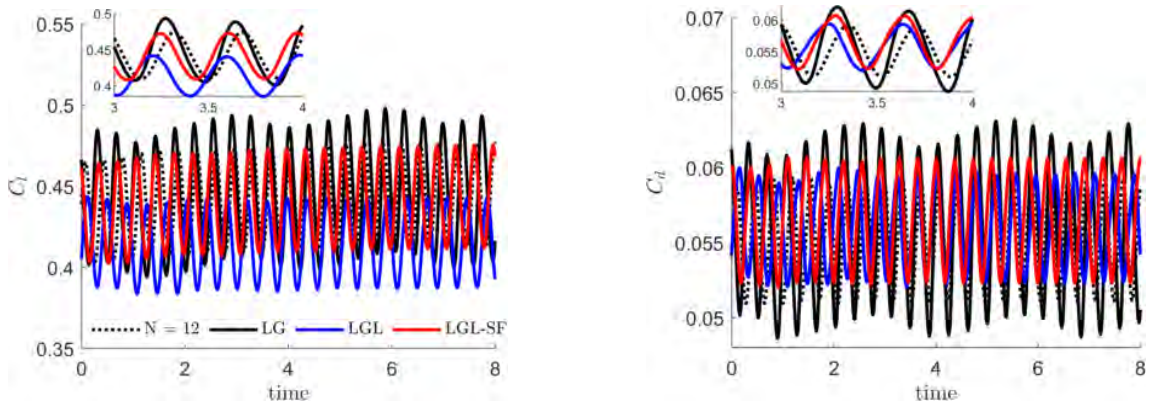

(a) (b)

Figure 7: Lift (a) and drag (b) coefficients of underresolved flows for a polynomial orders of $N = 6$. LG = Legendre-Gauss nodes (standard DG formulation), LGL = Legendre-Gauss-Lobatto nodes (standard DG formulation), LGL-SF = Legendre-Gauss-Lobatto nodes & split form DG).

5.3 Three-dimensional airfoil flow

Ee solve the three-dimensional flow over the NACA 65(1)-412 airfoil under an angle of attack of $\alpha = 10°$ at Reynolds number Re_c = 20,000. The flow is characterized by a laminar separation bubble at the leading edge and subsequent transition to turbulence [79]. The airfoil is extruded by half a cord length ($0.5c$) in the spanwise direction and periodic boundary conditions are applied to approximate an infinite wing, resulting in a total of 33,660 hexahedral elements. The computations are initialized by mapping a two-dimensional flow field uniformly in the spanwise direction.

Two cases are considered: the standard DG scheme with Gauss nodes and the kinetic energy stable split form with Gauss-Lobatto nodes. Polynomial orders of $N = 10$ and $N = 12$ in the region close to the airfoil are chosen, but the order is gradually lowered in the far field to decrease the computational costs. A CFL number of 0.5 ensures that numerical instabilities do not arise from the time stepping scheme.

Only the split form DG scheme has the numerical robustness to compute this flow and produce results past the initial start-up phase, as summarized in Table 2. Figure 8 (a) shows the lift coefficient over time for the different schemes and polynomial orders, where the dashed lines indicate the points of termination (crash). Figures 8 (b) – (d) show iso-surfaces of the vorticity at $t = 0.2$, $t = 1.6$, and $t = 18.1$ respectively and illustrate the flow transition to three

Table 2: Numerical Stability of the 3D airfoil simulations at 10° incidence. ✓= stable, x = unstable.

Node type	Flux method	$N = 10$	$N = 12$
LG	Standard	x	x
LGL	Split form	✓	✓

dimensional turbulent structures. The numerically unstable elements in the standard DG scheme are highlighted in red in Figure 8 (b).

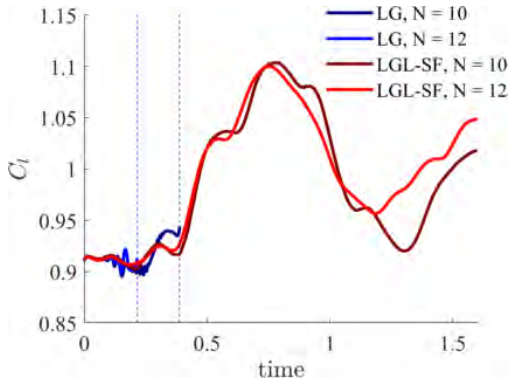

(a)

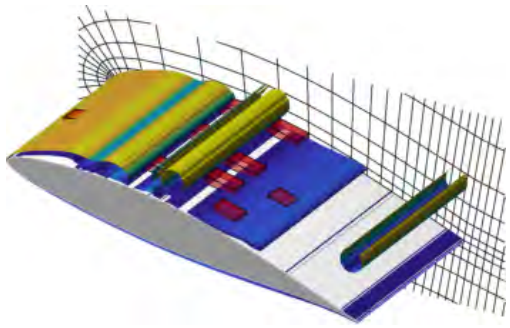

(b)

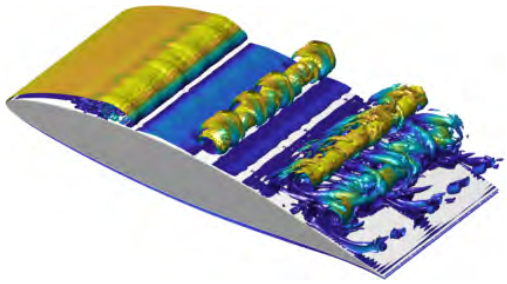

(c)

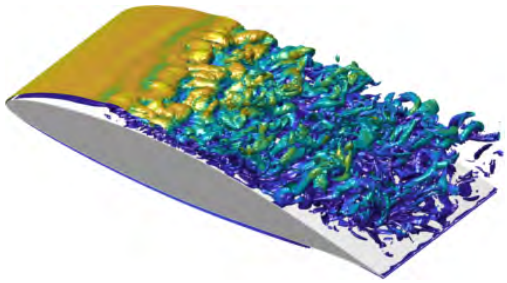

(d)

Figure 8: (a) Lift coefficient for $N = 10$ & 12 and standard & split form DG. Points of termination indicated by dashed lines. (b) – (d): Iso-surfaces of the vorticity. Numerically unstable elements for the standard DG are highlighted in red.

Although the Reynolds number is moderate, the turbulent flow over the airfoil in Figure 8 (d) illustrates the small-scale vortical structures and the need for a numerically robust scheme to capture them without filtering. Because the standard DG formulation crashes – even with high-order approximations – we see that transitional flows with high velocity gradients greatly benefit from the enhanced robustness of the split form DG scheme.

6 The unexpected properties of the NACA 0012 at moderate Re

6.1 Wind tunnel measurements on the NACA 0012

Fig. 9 shows $c_l(\alpha)$ and $c_d(\alpha)$ for the wind tunnel experiments. There are a number of features of $c_l(\alpha)$ alone that are notable. First, about $\alpha = 0°$ the lift slope, $dc_l/d\alpha = c_{l\alpha}$ is negative. c_l reaches a local minimum value at $\alpha = 0.5°$ and then increases with a slope significantly above the theoretical thin airfoil result ($c_{l\alpha} = 2\pi$) up to$\alpha = 3°$. At this point c_l exceeds the 2D theoretical value. With further increase inα up to $9°$, $c_{l\alpha} < 2\pi$ and at higher α the airfoil begins to stall, but not abruptly. The resolution in α is only just sufficient to show the negative $c_{l\alpha}$ about $\alpha = 0°$, but the result is very robust and repeatable. The inset of Fig. 9 shows a separate set of experiments from $-1.6°$ to $+1.6°$ in steps of $0.2°$. In general, the data agree with the $c_{l\alpha} = 2\pi$ line only coincidentally, at the three points where the curves intersect. By contrast, $C_d(\alpha)$ (Fig. 9b) does not have discontinuous regions. It is also symmetric about $\alpha = 0°$ and could be easily fit within uncertainties with a smooth function.

Since c_l is negative at small positive α so is L/D (Fig. **??**a). There is a broad maximum in L/D from about $\alpha = 3$ to $7°$ Its value, from 13 – 15, is respectable for a moderate Re wing, mainly because the lift is higher than expected. The lift-drag polar (Fig. **??**b) has a characteristic loop with $c_l = 0$ at three different c_d points. dc_l/dc_d is also quite steep, up to $c_l = 0.4$. Certain of these features are not normally associated with lower Reynolds number airfoil properties, and certain of them, such as the multiple $c_l = 0$ crossings are not usual in any circumstance. All observations exceed experimental uncertainty, and the curves are symmetric within those bands about $\alpha = 0°$

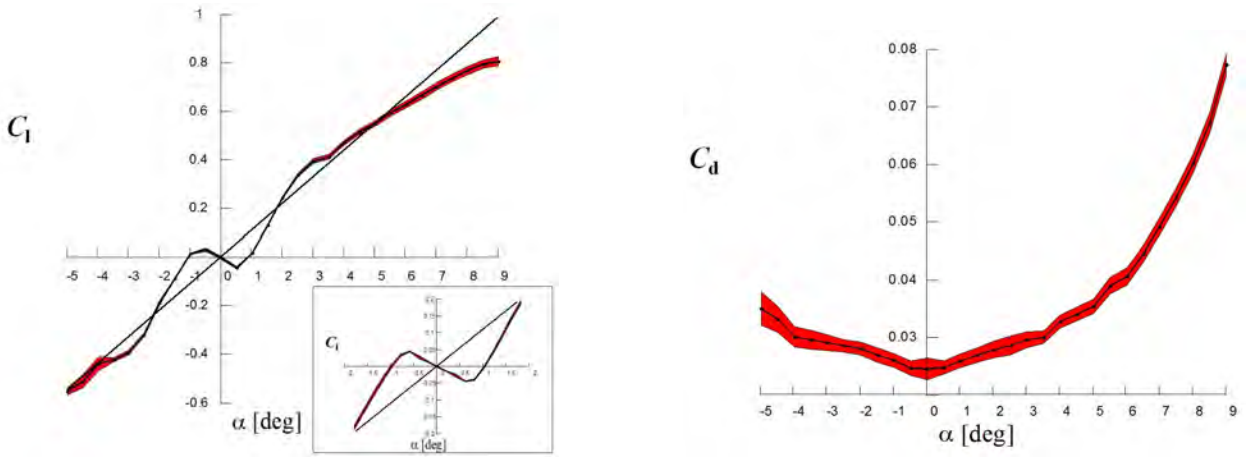

(a) (b)

Figure 9: Experimental values for (a) $C_l(\alpha)$ and (b) $C_d(\alpha)$ for the NACA 0012 at $Re = 5 \times 10^4$. The mean values in black show the average of ten measurements made during a single test and the envelope shaded in red is bounded by the standard deviation of those measurements.

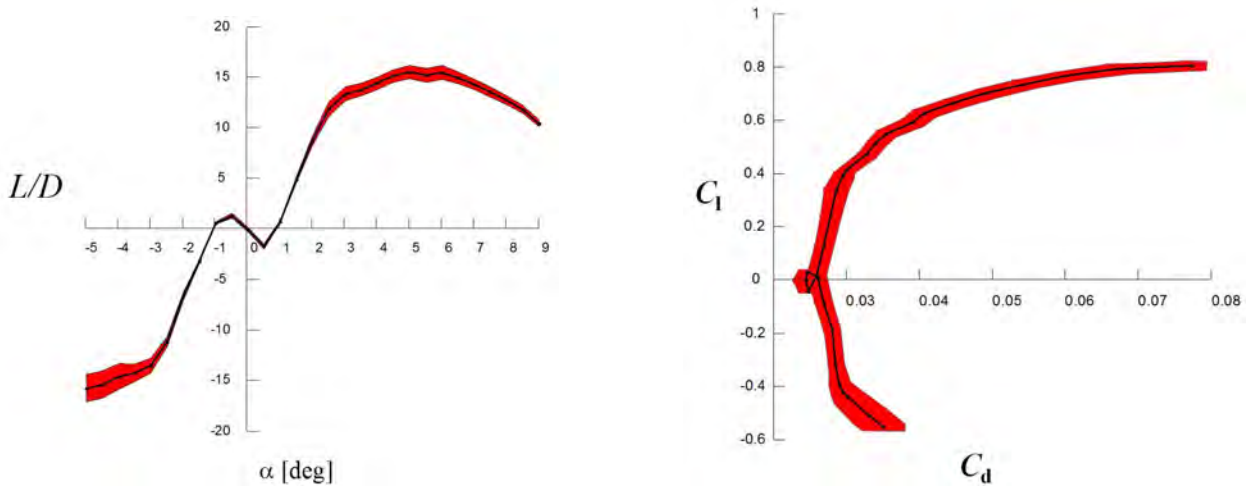

(a) (b)

Figure 10: Two-dimensional performance curves as (a) $L/D(\alpha)$ and (b) $C_l(C_d)$ for the NACA 0012 at $Re = 5 \times 10^4$.

The observations from Figs 9 and 10 are not peculiar to the 2D case (as simulated with endplates), but are just as evident for the finite wing, AR = 6.4 geometry shown in the equivalent Figs 11 and 12.

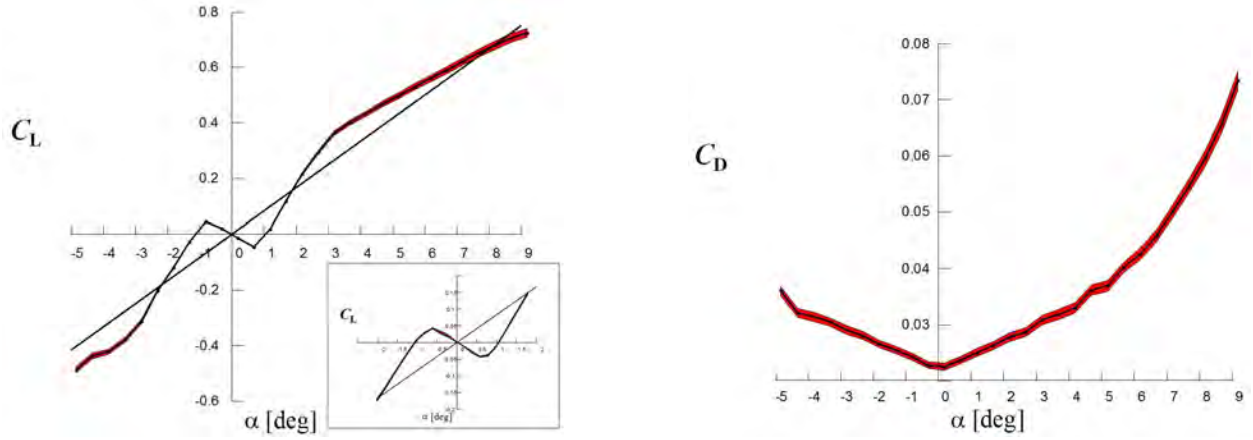

(a) (b)

Figure 11: Finite wing force coefficients from experiment: (a) $C_L(\alpha)$ and (b) $C_D(\alpha)$ for $AR = 6.4$ wing at $Re = 5 \times 10^4$.

C_L is measurably and repeatably negative for small positive α the three, almost-linear slopes all differ from an expected value, $C_{L,\alpha} = c_{l,\alpha}(AR/AR+2)$ where the 2D value, $c_{l,\alpha} = 2\pi$s decreases as AR decreases (we ignore the correction for span efficiency, which is close to 1), though it remains a good average value over all α. From $\alpha = 3°$ to $\alpha = 6°$, C_L significantly exceeds the theoretical value. C_D is not, in general, appreciably higher than c_d so L/D (Fig 12a) again has a broad peak in $\alpha = 3 - -6°$. The loop in the lift-drag polar (Fig. 12b) remains as distinct as for the 2D case.

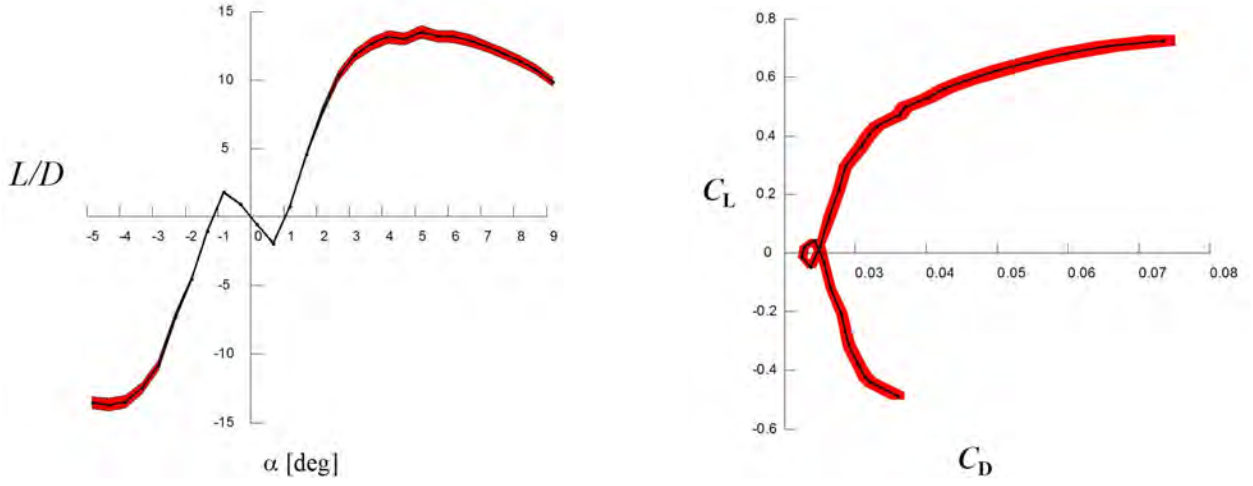

(a) (b)

Figure 12: Finite wing performance measures; (a) $L/D(\alpha)$ and (b) $C_L(C_D)$ for $AR = 6.4$ wing at $Re = 5 \times 10^4$.

PIV-derived, time-averaged fields of $|u|(x, z)$, $\omega_y(x, z)$ (Fig. 13) and $u(x, z)$, $w(x, z)$ (Fig. 14) explain the force balance observations.

At $\alpha = 0°$ the flow about the NACA 0012 is symmetric and separates (on both sides) before the trailing edge. At $\alpha = 0.5°$ the separation point has moved forward on the upper (suction) surface, but has moved aft in the lower (pressure) surface (Fig. 13a, row2). The contour of zero spanwise vorticity no longer leaves the trailing edge straight, but is deflected upwards (Fig. 13b, row2). Regions of $u < 0$ are more prominent on the upper surface (Fig. 14a, row2), and the distribution of $w(x, z)$ aft of the trailing edge is asymmetric, with stronger, positive w on the lower side (in Fig. 14b, row2, $w = 0.25$ m/s beneath the airfoil, and -0.2 m/s above it). At this α, the lowest part of the airfoil

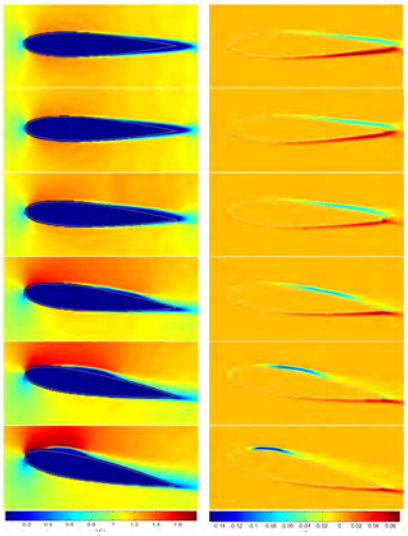

Figure 13: PIV-derived fields of (a) velocity magnitude, and (b) spanwise vorticity for $\alpha = [0, 0.5, 2, 4, 6, 8]^\circ$.

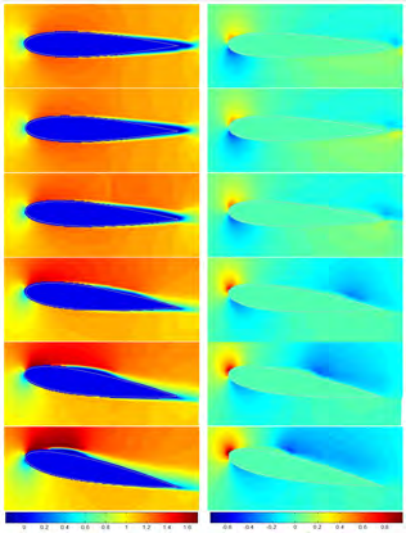

Figure 14: Time-averaged fields of: (a) u, and (b) w velocity components for $\alpha = [0, 0.5, 2, 4, 6, 8]^\circ$.

is below the trailing edge and a slightly favorable pressure gradient allows the streamlines to follow the curvature into an upward direction. The net acceleration is upwards, as the lower streamlines have higher curvature, and the net lift is negative. At the same time, the laminar separation before the upper surface trailing edge assures that streamlines here are also deflected slightly upwards. At $\alpha = 2^\circ$ row3 in Figs 13 14), the streamlines are not deflected strongly upwards on the lower surface, and though the separation line has moved further forward on the upper surface, the net flow has returned downwards. The trailing wake has its smallest streamwise extent, like an attached recirculation bubble. (The flow is highly unsteady here, and so explanations on time-averaged fields need careful interpretation.) At $\alpha = 4^\circ$ (row4 in Figs 13, 14, all fields show signatures of a separation bubble that reattaches on the upper surface, close to where $w(x, z)$ has its highest negative value. The flow acts as if the airfoil had a higher convex curvature on the upper surface, formed by the combination of airfoil surface and separation bubble. The changed effective geometry accounts for the better than expected C_L around this α (Fig. 11a). The drag cost is comparatively small and this α-range corresponds to the beginning of the broad maximum in L/D (Fig. 12a). If the separation bubble can be termed a Laminar Separation Bubble (LSB) in the classical sense, then the LSB is associated with significantly improved aerodynamic performance at this α, which is contrary to most literature interpretations based on observations at higher Re. As the LSB moves forward on the upper surface with further increases in α (6° and 8°, rows 5, 6, in Figs 13,14) the LSB shrinks in streamwise extent and the spanwise vorticity becomes more strongly negative at the outer shear

layer. This phase is associated with reduced C_L, but continued high L/D. There is a broad downwash region in $w(x, z)$ from the mid-point of the LSB to the airfoil trailing edge. Figs 13 and 14 are for a mid-span section through the $AR = 6.4$ wing. Based on the very similar shapes of the force balance data, for example, $C_l(C_d)$ (Fig. 10b) and $C_L(C_D)$ (Fig. 12b), the 2D and finite wing results are not expected to be significantly different there, and the bubble dynamics are not appreciably different, consistent with observations in [75] for an E387 at similar Re.

7 Experimental and Numerical Investigations of the Flow over a NACA 65(1)-412 Airfoil

7.1 Laboratory and numerical experiment

One purpose of this study is to closely compare equivalent investigative procedures. Numerical simulations solve the known Navier-Stokes equations, albeit on a discrete grid. No modelling is used, but certain procedures may be required to regularize the solutions, particularly for low Mach number. The flow is fully resolved in space and time, with all velocity and pressure fields. The sensitivities of these transitional Re flows mean that high spatial resolution is required over large parts of the near-foil field, and calculations are expensive. Furthermore, each different U, or α entails a completely new calculation because either Re or the problem geometry are now new. By contrast, wind tunnel or water channels have analog Navier-Stokes solutions, but to problems whose specifications are not precisely known. If these can be made sufficiently close to the nominal (ideal) problem geometry, then systematic variations in U and α can reveal dependencies in an efficient way.

Finally, experiments must be interrogated with specific measurement techniques, each of which yield estimates of selected quantities in some reduced dimension of the full physical field. Here Re $= 2 \times 10^4$ is reachable by DNS with no model. The flow quality in the wind tunnel is good down to a certain minimum U, which sets a maximum on chord length. The strain gauge load cells have a lower noise floor which is fixed in mN, so the wing area must be sized carefully for force measurement resolution. All force measurements require a certain strain and model support deflection, but this cannot be large compared with effective disturbance scales in the flow. As will be shown later, the optimal wing area and aspect ratio differ for force and flow field measurements, respectively, driving the design alternately to high and low aspect ratio wings. In a true infinite wing problem, or in a computational box with wrap-around end conditions, AR, is not an important parameter. However, in a physical model, wall or end-plate boundary layers interact with the wing tips. The ways in which they do so will differ according to the wall/plate boundary conditions in wind tunnel or water channel experiments.

The experiments described here thus cover a range of AR and Re to specifically illustrate their influence, and we make a deliberate mix of DNS (DG), wind tunnel (WT) and water channel (WC) experiments, deducing most likely physical truths from overlap. The final section will show simulations that show how end-wall boundary conditions can significantly impact the measured airfoil performance.

Several AIAA papers [79, 80] were written and conference contributions were made that we have either submitted to the AIAA Journal or are in the process of maturing to journal manuscripts.

7.2 DNS problem setup

The flow over a NACA 65(1)-412 airfoil is simulated in three dimensions at a Reynolds number based on the chord length of Re_c = 20,000 and a Mach number of M = 0.3. A Prandtl number of Pr = 0.72, Sutherland constant R_T = S/T_f = 110/200, and ratio of specific heats γ = 1.4 are chosen in accordance with Nelson [81]. A fouth-order explicit Runge-Kutta adaptive time-stepping scheme is used with time step sizes Δt of the order $\mathcal{O}(10^{-5})$.

For lower angles of attack ($0^\circ \leq$ AOA $\leq 8^\circ$), we take advantage of the more accurate Legendre-Gauss quadrature nodes in the standard DG formulation, while the case AOA = 10° is computed with the more robust kinetic energy conserving split form, given that it is strongly turbulent. The interface fluxes in the DG scheme are obtained from an upwinding Roe solver for the inviscid part and a Bassy-Rebay formulation for the viscous flux.

The airfoil surface is treated as no-slip adiabatic wall and free-stream conditions are set at the outer boundaries. To account for the curvature of the airfoil, the boundary elements are curved and fitted to a spline representing the airfoil's surface according to Nelson *et al.* [78]. The 2D simulations are initialized with an uniform velocity field under the respective angle of attack and run for 50 convective time units (1 $CTU = t \cdot c/U_\infty$). The three-dimensional simulations are initialized with 2D data and run at least until quasi-steady state has been reached and the lift and drag coefficients fluctuate around a mean, typical after 10 to 20 convective time units.

Table 3: Domain sizes of selected airfoil studies.

Source	R	W	L_z
Shan *et al.* [84]	4	3	0.1
Jones *et al.* [82]	7.3	5	0.2
Visbal [85]	100	100	0.4
Zhang *et al.* [86]	6	10	0.8
Gageik *et al.* [87]	30	8	0.1
Hosseini *et al.* [88]	2	6.2	0.1
Balakumar [83]	15	15	0.2
present (periodic)	30	30	0.5
present (endwall)	5	15	3

Domain size and resolution

The domain size is a critical parameter for any simulation of external aerodynamics. Usually, a compromise has to be found between a large-enough domain to minimize the effects of the outer boundaries and the available computational resources limiting the number of grid points to be used. Typical parameters of the domain are the radius *R* and the wake length *W* (see Figure 15).

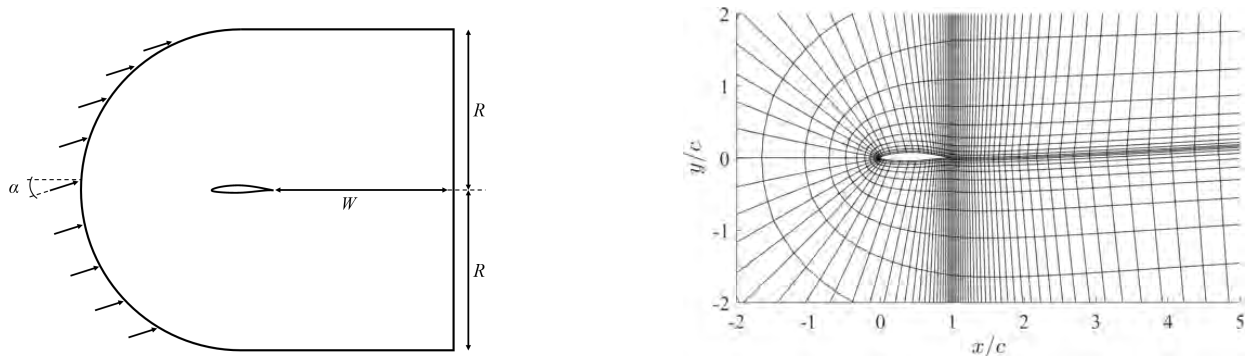

(a) (b)

Figure 15: C-Grid computational domain with general parameters (a) and elements used for the simulations (b). Only elements withouth interior Gauss nodes are shown.

Infinite airfoil with periodic spanwise boundaries For simulations with periodic boundary conditions in transverse direction, we use a C-grid mesh with a sharp trailing edge and a domain radius and wake of 30 coord lengths. The wing is extruded by $L_z = 0.5c$ along the span. We assume this to be sufficient as others have shown only negligible effects on larger domains [82, 83]. Table 3 summarizes the dimensions of the computational domain for selected high-fidelity airfoil simulations and shows that the presented setup compares well to other studies.

The three-dimensional computational domain is split into 33,660 hexahedral elements, which are clustered around the airfoil. A close-up view of the mesh is given in Figure 15 (b). Within each element, the solution is approximated on a N^{th} order polynomial basis, where we choose $N = 12$ in the region around the airfoil and gradually decrease the order to $N = 1$ in the far field. To prevent spurious reflections from the coarser elements and the outer boundaries, an exponential filter is employed (see Chaudhuri *et al.* [89]). No filter is used in the elements directly surrounding the airfoil and the filter order is progressively lowered from $\phi = 64$ to $\phi = 16$ as the distance to the airfoil increases.

For the NACA 65(1)-412 airfoil, Nelson *et al.* [78] show numerical convergence at a polynomial order of $N = 12$ an angle of attack of 4° and Reynolds number of 20,000. With nodes of the Legendre-Gauss quadrature, this accounts to a wall-normal distance of the first collocation point at the leading edge of $\Delta\eta^+_{max} \approx 0.85$, $\Delta\xi^+_{max} \approx 1.5$, and $\Delta\zeta^+_{max} \approx 2.1$. These values are well within the limits accepted for DNS [90]. Note that the grid spacing is estimated by the distance to the first collocation point of the Gauss nodes.

Finite airfoil with endwalls To model the effect of endwalls, the computations are carried out on a smaller domain (see Tab. 3). The no-slip wall extends four cord lengths in front of the airfoil and results in an approximate boundary

layer thickness of $\delta \approx 4.91x/\sqrt{Re_x}$ = 0.07c, estimated by the Blasius solution for laminar flow. The element spacing along the span is consistent with the infinite wing simulations and only refined close to the transverse walls.

The computational domain of the finite airfoil with aspect ratio AR = 3 consists of 208,692 hexahedral elements. A polynomial order of N = 10 is used in the region around the airfoil and gradually decreased to N = 1 in the far field, similar to the setup with periodic boundaries. Gauss-Lobatto quadrature nodes are chosen as they allow for larger time steps than the Gauss points, and the simulations are stabilized by using an exponential filter, where the filter order is progressively lowered from ϕ = 64 around the airfoil to ϕ = 16 in the far field. The simulation of the airfoil with endwalls therefore classifies as implicit LES.

7.3 Results and Discussion

7.3.1 Time-averaged lift and drag

The time-averaged c_l and c_d as well as the inviscid thin airfoil theory prediction (assuming the experimental α_{0L}) are given over a range of α in Fig. 16. The lift-slope $c_{l,\alpha}$ is close to 2π, for small α. Note how $\alpha_{0L} > 0$ ($c_l < 0$ at $\alpha = 0°$), even when the camber is positive, suggesting an effective negative camber at low α due to flow separation. This behavior is significantly different than at a design Re $= 10^6$, where $\alpha_{0L} < 0$ and design $\alpha = 0$ [8].

At $\alpha = 4°$, DNS and WT c_l agree and lie below the inviscid prediction. At $\alpha = 8°$, DNS and WT c_l do not agree: DNS is above the 2π line, a state not reached in experiment until $\alpha = 9.5°$. At $\alpha = 10°$, DNS and WT c_l agree once more, and both exceed the inviscid value.

WT $c_l < 0$ when $c_{d,min}$ is reached at approximately $\alpha = -1.5°$. As α decreases below $-1.5°$, c_l no longer falls with slope 2π, departing, once again, abruptly, from the inviscid line. Disagreements in c_d occur at the same α as those in c_l. Both show an abrupt improvement in performance (decrease in c_d, increase in c_l) at some critical angle of attack (α_{crit}).

The lift-drag polar (Fig. 17 shows the abrupt jump in experimentally measured forces at a critical angle of attack,α_{crit}. It will be shown later that the jump to the high-lift low-drag state is due to the formation of a laminar separation bubble (LSB). As noted before, in this Re range, the increase in L/D due to bubble formation is opposite to what is often reported at Re $> 10^5$.

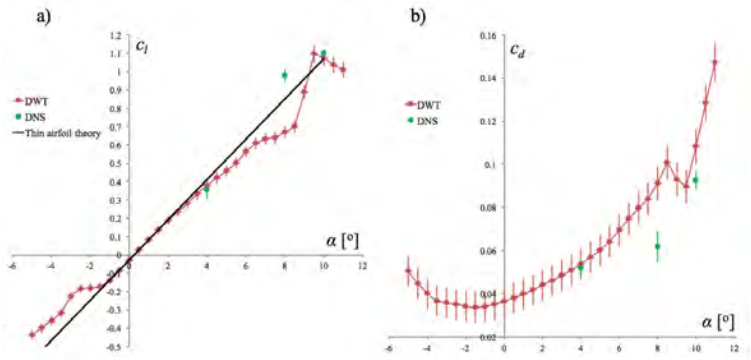

Figure 16: Time-averaged $c_l(\alpha)$ (a) and $c_d(\alpha)$ (b), for the NACA 65(1)-412 at $Re = 2 \times 10^4$.

The disagreement between WT and DNS comes from different α_{crit}. α_{crit} is hard to estimate with great accuracy in experiments, as any real experiment is influenced by the free stream disturbance environment, model and tunnel vibrations, surface roughness, and model AR, to name a few. The sensitivity to AR has been investigated, and Fig. 18 gives c_l and c_d for two wings, $AR = 3$ and 13, sized for Re $= 4 \times 10^4$ and tested under identical conditions. Recall that $\alpha_{crit} = 9.5°$ for WT at Re $= 4 \times 10^4$. In Fig. 18, $\alpha_{crit} = 8°$ for $AR = 3$ and $\alpha_{crit} = 7°$ or $7.5°$ (depending on sweep direction) for $AR = 13$, and therefore α_{crit} is clearly a function of both Re and AR.

The relative importance of end effects, which appear to increase α_{crit} diminish with increasing AR, so α_{crit} in any experiment will likely be lower than the corresponding DNS value, as is seen in Fig. 16. This also means that PIV data derived from the $AR = 3$ wing will show a different α_{crit} than the force balance data derived from an $AR = 13$ wing in the same facility, as evidenced by the curves in Fig. 18. However, if we disregard the particular value of α_{crit} then the flow physics near mid span and the transition from a fully separated state (SI) to a reattached state (SII) will be the same, so dynamically equivalent flow fields can now be compared around that transition.

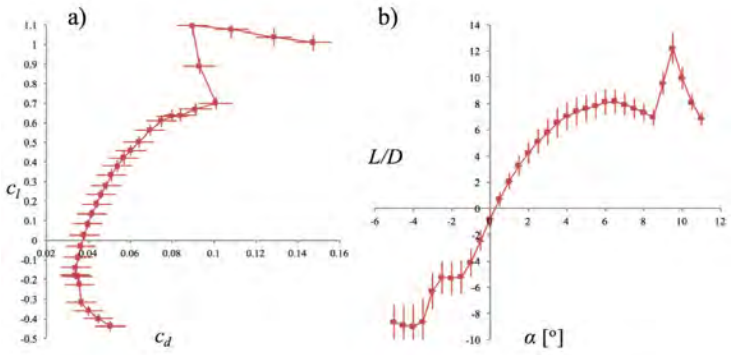

Figure 17: The lift:drag polar $c_d(c_l)$ (a) and $L/D(\alpha)$ (b) for the NACA 65(1)-412 at $Re = 2 \times 10^4$.

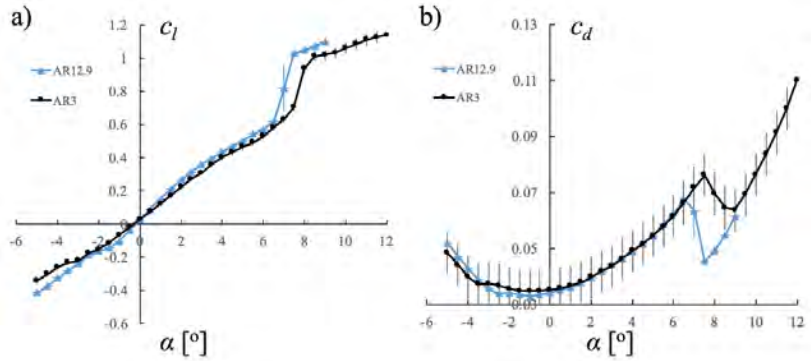

Figure 18: $c_l(\alpha)$, $c_d(\alpha)$ in (a) and (b), at $Re = 4 \times 10^4$ for $AR = 3$ and $AR = 13$.

7.3.2 Flow topology – time-averaged fields

The jump from SI to SII seen in the c_l and c_d plots of Fig. 16 is caused by the separated boundary layer reattaching to the airfoil surface at α_{crit} [9]. The development of the time-averaged flow before α_{crit} is shown in Fig. 19 using PIV-generated streamlines. At $\alpha = 0°$, the flow separates before the trailing edge over the suction (upper) surface. A recirculating region (v1) extends over the airfoil and aft of the trailing edge. A counter-rotating vortex (v2) appears first to originate at the trailing edge from flow around the pressure (lower) side. As v1 grows with increasing α, v2 is increasingly distorted and displaced downstream, appearing more as a secondary structure that is induced by v1. A comparison of streamlines from DNS and experiment for $\alpha = 0°$ is shown in Fig. 20. At $\alpha = 10°$, a blue line has been added that encloses the airfoil as well as the viscous recirculating regions. The recirculating fluid has about the same cross-section as the airfoil itself, and a similar vertical displacement. It could be described as a large LSB with virtual reattachment in the wake, aft of the physical trailing edge. The global flow field and streamline deflection (and hence the lift) is determined by the effective airfoil shape, made up of the combined airfoil and LSB geometry.

The laminar boundary layer appears to separate from the surface at a well-defined angle in Fig. 19, and Fig. 21 shows a systematic estimation of the shear layer position in chordwise and chord-normal coordinates.

More detailed comparisons of $u-$ and ω_y- profiles at $\alpha = 4°$ (Fig. 22) show reasonable qualitative agreement, though in DNS, the boundary layer diffuses away from the surface more rapidly with streamwise distance.

At $\alpha = 10.0°$ the slow recirculating region reaches its largest size (Fig. 19). The effective airfoil shape is not aerodynamically efficient, leading to a decrease in L/D after a local maximum but before α_{crit} (Fig. 19). At $\alpha = 10.1°$, the flow state abruptly changes (Fig. 23). A laminar separation bubble forms and closes from about $1/3c$ – $2/3c$. With small further increases in α, the bubble moves forward and shortens. T he formation of the LSB (transition from SI to SII) greatly increases L/D.

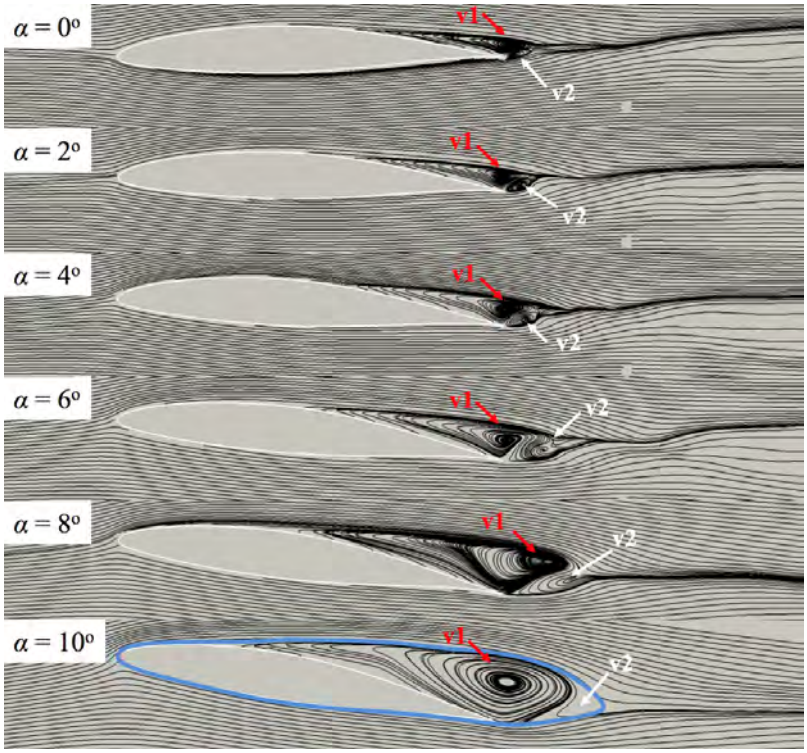

Figure 19: Time averaged streamlines for $\alpha < \alpha_{\text{crit}}$

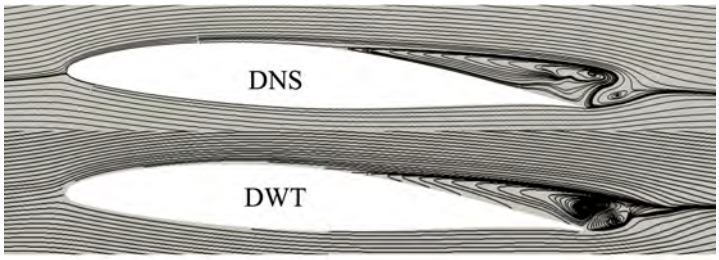

Figure 20: Comparison of time-averaged streamlines from DNS and wind tunnel experiment (DWT) for $\alpha = 4°$.

7.3.3 Instantaneous flow fields

Three qualitatively distinct types of flow field can be identified from instantaneous PIV and dye injection images: type 1) laminar separation with vortex rollup beginning after the trailing edge; type 2) laminar separation with vortex rollup beginning over the airfoil and no reattachment; type 3) laminar separation with reattachment. Flow fields of type 1 and 2 occur before α_{crit} and type 3 occurs after α_{crit}. Examples of time-averaged and instantaneous flow fields of type 1, 2, and 3 can be found in the top, middle, and bottom row respectively of Fig. 24. PIV and dye injection images of the same flow type look very similar, and the separation locations and angles at a given α are nearly identical. The main difference is that the dye injection images show a transition from flow field type 1 to type 2 and from flow field type 2 to type 3 at earlier α. This may be due in part to the much larger turbulence intensity in the water channel. When vortex roll-up occurs after the trailing edge (type 1), the primary instability mode is a wake mode where two opposite-signed shear layers interact. With increasing α, the roll-up moves forward until it now occurs over the solid surface (type 2) and the primary instability mode is in the separated shear layer. Following transition to type 3, at and after α_{crit}, the first wavy motions can be seen in the shear layer of the short laminar separation bubble. It is the rapid growth of this mode that leads to pairing and transition and a flow that is reattached, in the mean, though no instantaneous flow field resembles this mean.

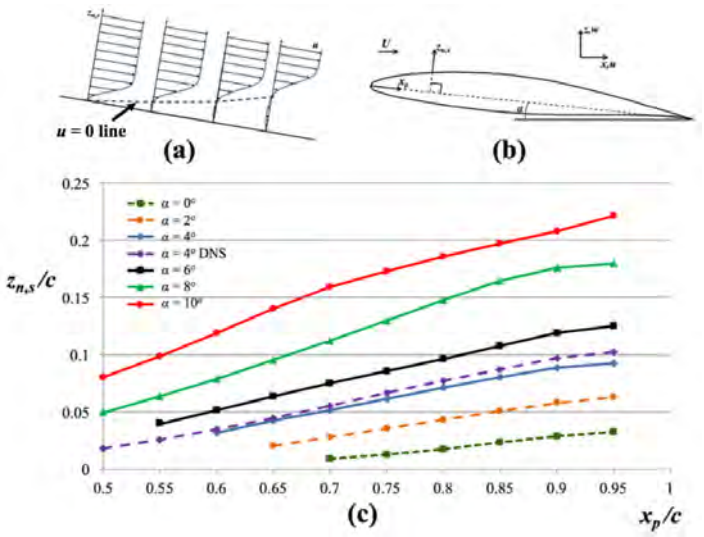

Figure 21: (a) $u = 0$ line definition, (b) coordinate system definition, (c) $u = 0$ line locations from PIV for $\alpha = [0°^{-}10°]$ and DNS $u = 0$ line location for $\alpha = 4°$.

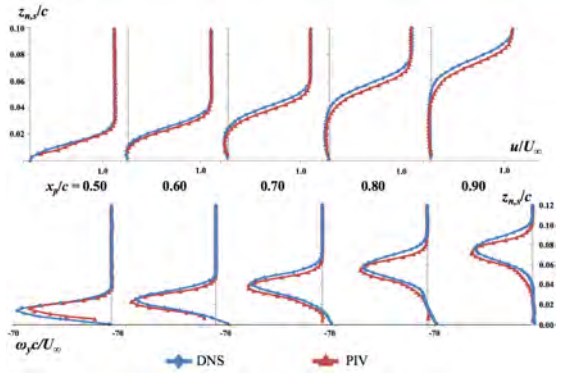

Figure 22: $u-$profile (top) and ω_y-profile (bottom) comparison between DNS and PIV over the suction surface of the airfoil for $\alpha = 4°$.

7.3.4 Wake vortex shedding frequency

Wake vortex shedding frequency data from seven tests, expressed as the non-dimensional Strouhal number ($St = fc/U$), has been plotted for $\alpha < \alpha_{crit}$ (flow field types 1 and 2) in Fig. 25. Reliable measurements could not be made after α_{crit} because of the increased diffusion of dye before the trailing edge due to increased mixing in the reattached boundary layer when an LSB forms. St remains between 3 and 3.3 for $0° < \alpha < 3.5°$, but drops between $\alpha = 3.5°$ – $4.5°$ to approximately 2.6, before increasing to approximately 3.25 at $\alpha = 5°$ and remaining nearly constant until $\alpha = 8°$. Three data points for $6° < \alpha < 7°$ fall between 1.5 and 1.62, corresponding to approximately half the mean values for all other tests. The existence of prominent first subharmonics suggest a vortex pairing or merging process.

St can be determined using DNS force time traces, as wake vortex shedding will cause oscillations in lift and drag. DNS St values at $\alpha = 0°$ and $4°$ fall within the same range as experimental data. However, DNS gives $St = 1.9$ at $\alpha = 6°$, which is below most experimental values. It is interesting to note that it appears this value would agree with experimental data had the experimental data continued to fall at the rate seen between $\alpha = 3.5° - 4.5°$. Fair comparisons cannot be made at higher α, as the experiment and DNS show the airfoil in different flow states.

The jump in St seen between $\alpha = 4.5°$ and $5°$ may be associated with the switching of the dominant instability that leads to wake vortex shedding from a shear layer instability to a wake instability as the flow field switches from type 1 to type 2. The switching between type 1 and type 2 flow fields was found to occur at $\alpha = 5.5° \pm 0.5°$. However, it should be noted that an upstream disturbance can create a dye filament pattern that may persist into the wake. This means that some wake patterns, and therefore frequency measurements, may be impacted by disturbances that have

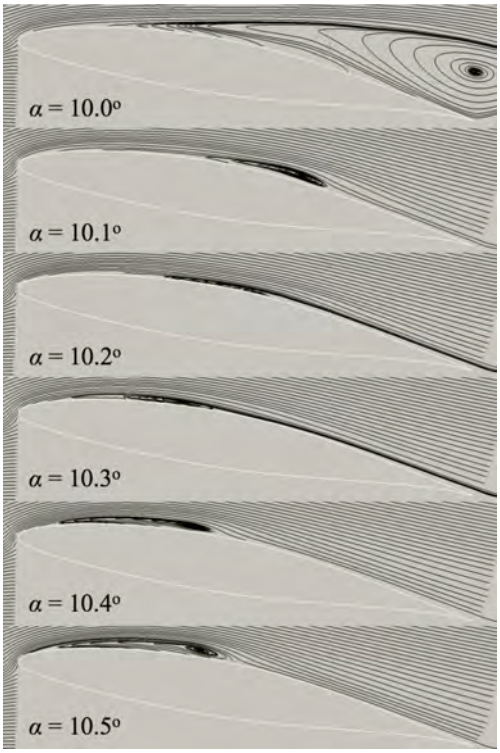

Figure 23: Time-averaged streamlines close to α_{crit}.

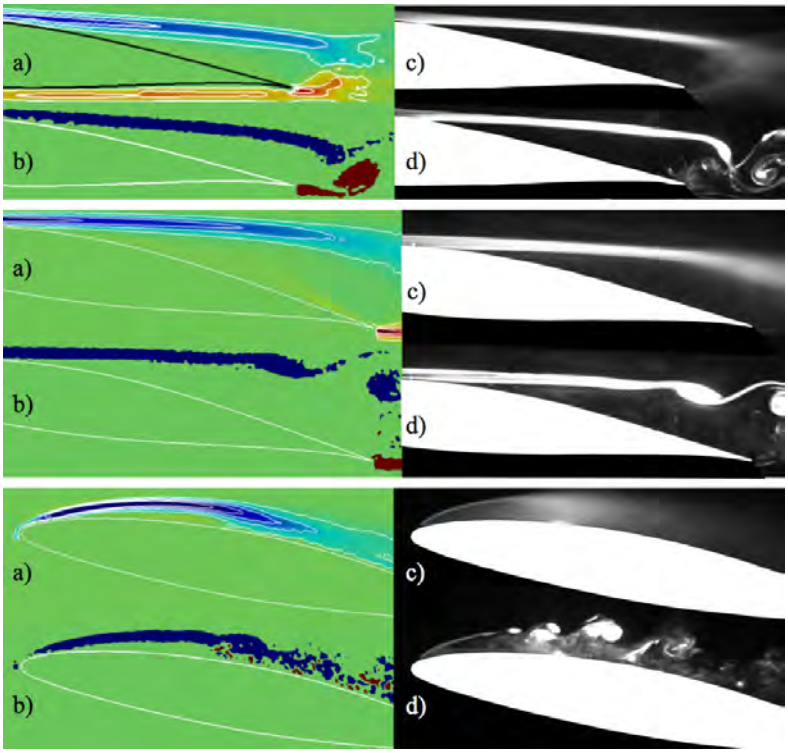

Figure 24: (a) time-averaged ω_y from PIV, (b) instantaneous ω_y from PIV, (c) time-averaged and d) instantaneous dye flow visualization images for $\alpha_{\text{PIV}} = \alpha_{\text{DFV}} = 4^\circ$ (top), $\alpha_{\text{PIV}} = 9^\circ, \alpha_{\text{DFV}} = 6^\circ$ (middle), and $\alpha_{\text{PIV}} = \alpha_{\text{DFV}} = 11^\circ$ (bottom)

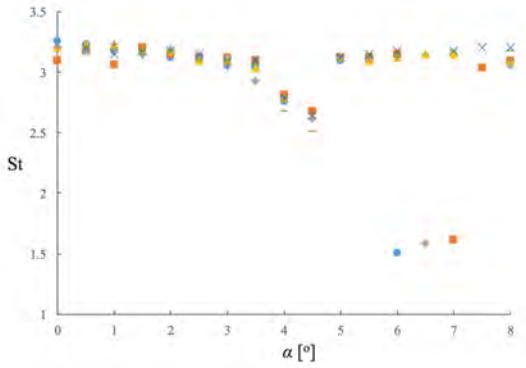

Figure 25: $St(\alpha)$ – seven different tests are overlaid for nominally identical conditions for any given α.

since evolved or died out. It is also not known how large the wake vortex formation region is, and how measurements are impacted by their proximity to this region. Finally, dominant frequencies become harder to measure using the current method as the wake becomes more turbulent at the higher α. Further hot-wire tests are suggested to investigate the wake vortex shedding frequency in more detail.

7.3.5 3D FTLE fields from 3D DNS

Figure 26 shows slices of the three-dimensional FTLE field in the transitional wake flow obtained from on-the-run particles traces of the DNS at AOA = 4°. Ridges in the backward-time FTLE indicate attracting LCS, which are surfaces of coherent fluid material. Vortex cores are clearly visible as bright spots enclosed by high FTLE values in Figure 26 and highlight the flow structure, which is dominated by large spanwise rollers enveloped by streamwise vortex tubes.

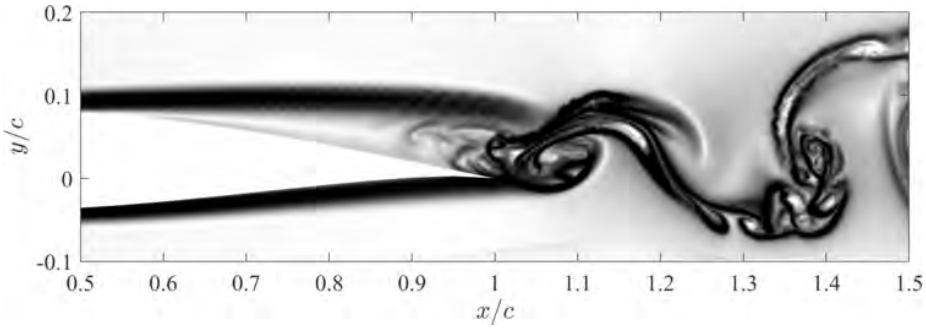

(a)

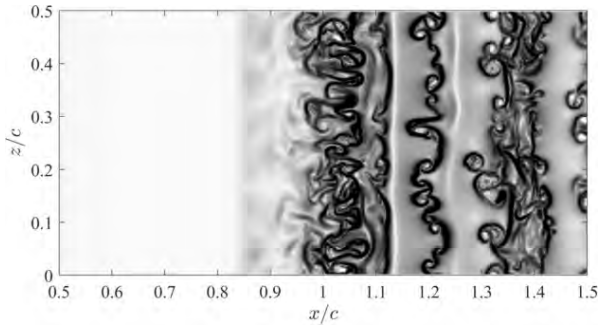

(b)

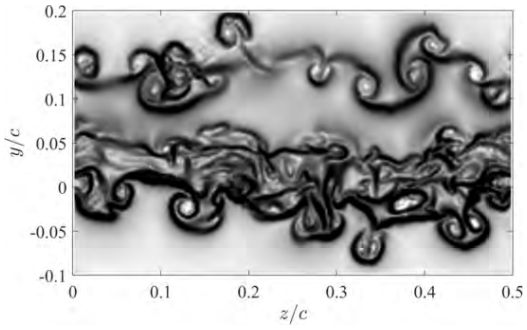

(c)

Figure 26: Backward-time FTLE slices of separating flow over a NACA 65(1)-412 airfoil under 4°. Particle trace integrated over T = 0.2. (a) side view; (b) top view (c) spanwise wake view

The transition of the flow field is shown in Figure 27. The surface streamlines are obtained from the local wall shear stress and show the transverse separation line at mid-cord for AOA = 4° (Fig 27 a). The Q-criterion omits regions of shear and therefore only shows the vortical flow in the transitioning wake. For AOA = 8° (Fig. 27 b), spanwise vortices shed from a slender laminar separation bubble at the leading edge and transition the flow early on.

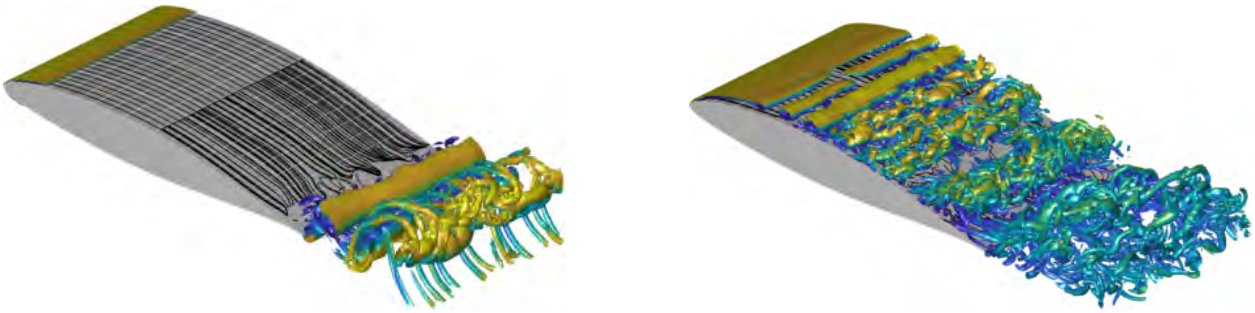

(a) (b)

Figure 27: Iso-surfaces of the Q-criterion for AOA = 4° (a) and 8° (b), colored by velocity. Surface streamlines are plotted in black.

7.3.6 Finite airfoil with endwalls

We visualize the flow pattern of the separating airfoil flow with endwalls through the continuous injection of Lagragian fluid tracers at several locations over the airfoil surface, as well as by extracting surface streamlines (Fig 28). Just as for the case with periodic boundaries (Fig. 27 a), the surface streamlines show the separation line at approximately mid-cord. The endwalls, however, induce a significant transverse bending of the line, which only remains straight in the center portion of the wing. As the thickness of the boundary layer at the airfoil's leading edge is only $\delta \approx 0.07c$, this effect is by more than a magnitude larger and likely caused by blockage in the spanwise direction.

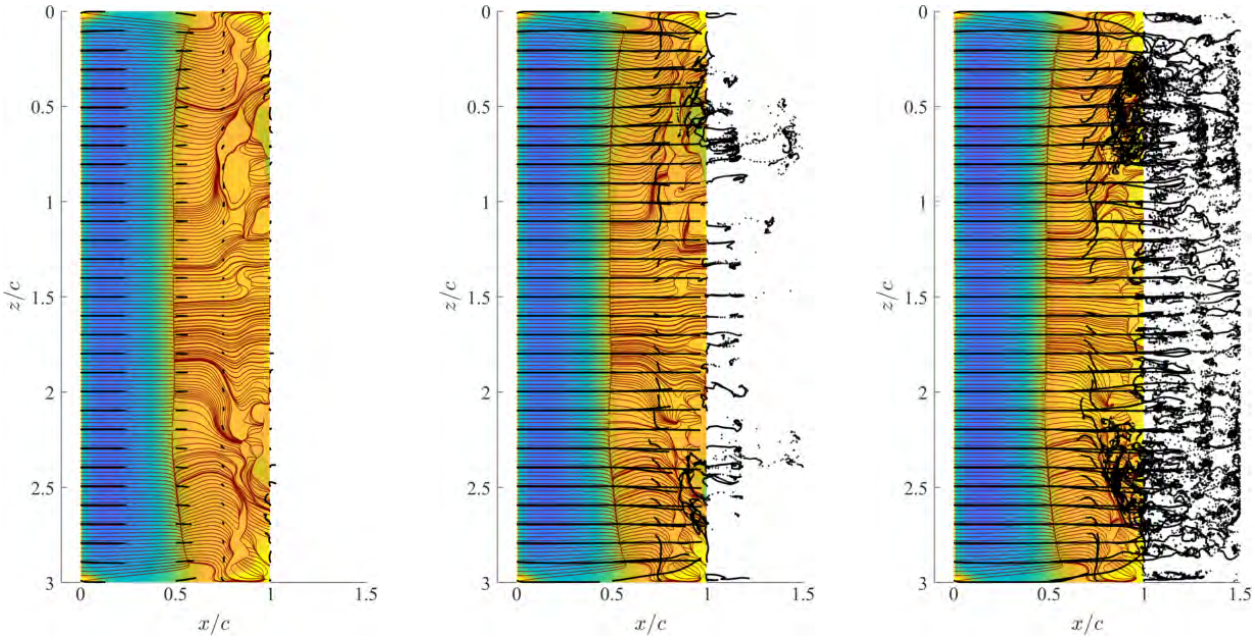

(a) (b) (c)

Figure 28: Top view of separating airfoil flow. Surface is colored by pressure coefficient with surface stream lines in red. Lagrangian particles (black) are continuously injected at different locations over the airfoil.

The advancing streaklines in Figure 28 at $t = 0.2$ (a), $t = 1.0$ (b), and $t = 1.99$ (c) show that large-scale three-dimensional structures govern the flow within the separation bubble and move fluid material towards the center of the wing. Material

transport and the curved separation line indicate that undisturbed flow conditions only exist within over one third of the airfoil at the center.

8 The Kinematics of Lagrangian Flow Separation in External Aerodynamics

Using theoretical development on early upwelling near asymptotic separatoin locations, we present a comprehensive picture of the kinematics of Lagrangian flow separation in external aerodynamics. It is shown how the fluid particles are ejected from the wall by the initial formation of a material spike that is consequently governed by FTLE dynamics and the asymptotic separation line. This research has been submitted and has been resubmitted after minor revisions to the *AIAA Journal* [42].

8.1 The Lagrangian backbone of separation and the spiking point

Using a coordinate system $[s,\eta]$ in direction tangential and normal to the wall respectively, we determine major fluid upwelling event by determing Lagrangian curvature changes relatively to the initial curvature $\bar{\kappa}_{t_0}^{t_0+T} := \kappa_{t_0}^{t_0+T} - \kappa_0$ in a neighborhood of the no-slip boundary foliated by a set of material lines initially parallel to the wall, parametrized by $\mathbf{r}_\eta(s),\ s\in[s_1,s_2]\subset\mathbb{R},\ \eta\in[0,\eta_1]\subset\mathbb{R}$. Such a foliation enslaves the initial local tangent $\mathbf{r}'_\eta$ and curvature κ_{0_η} to the position $\mathbf{r}_\eta$, making therefore $\bar{\kappa}_{t_0}^{t_0+T}$ a function of t_0, T and of the initial configuration $\mathbf{r}_\eta$ only. Here $(\cdot)' := \frac{d}{ds}(\cdot)$. The $\bar{\kappa}_{t_0}^{t_0+T}$ field can be directly computed from the flow map $\mathbf{F}_{t_0}^{t_0+T}$ using the relation

$$\bar{\kappa}_{t_0}^{t_0+T} = \frac{\left\langle \left(\nabla^2\mathbf{F}_{t_0}^{t_0+T}(\mathbf{r}_\eta)\mathbf{r}'_\eta\right)\mathbf{r}'_\eta, \mathbf{R}\nabla\mathbf{F}_{t_0}^{t_0+T}(\mathbf{r}_\eta)\mathbf{r}'_\eta\right\rangle}{\left\langle \mathbf{r}'_\eta, \mathbf{C}_{t_0}^{t_0+T}(\mathbf{r}_\eta)\mathbf{r}'_\eta\right\rangle^{3/2}} - \kappa_{0_\eta}\left[\frac{det\left(\nabla\mathbf{F}_{t_0}^{t_0+T}(\mathbf{r}_\eta)\right)\left\langle \mathbf{r}'_\eta,\mathbf{r}'_\eta\right\rangle^{3/2}}{\left\langle \mathbf{r}'_\eta, \mathbf{C}_{t_0}^{t_0+T}(\mathbf{r}_\eta)\mathbf{r}'_\eta\right\rangle^{3/2}} - 1\right], \quad (22)$$

where $\langle\cdot,\cdot\rangle$ denotes the inner product; $(\nabla^2\mathbf{F}_{t_0}^t(\mathbf{r}_\eta)\mathbf{r}'_\eta)_{ij} = \sum_{k=1}^{2}\partial_{jk}F_{t_0\,i}^t(\mathbf{r}_\eta)r'_{\eta_k},\ i,j\in\{1,2\}$, and $\mathbf{R}$ is the rotation matrix defined as

$$\mathbf{R} := \begin{bmatrix} 0 & 1 \\ -1 & 0 \end{bmatrix}. \quad (23)$$

We note that with a clockwise parametrization of the no-slip boundary, $\mathbf{R}\mathbf{r}'_\eta$ is the vector normal to the initial material line, pointing towards the boundary. The initial position $\mathcal{B}(t_0)$ of the Lagrangian backbone of separation – i.e., the theoretical centerpiece of the material spike over $[t_0,t_0+T]$ – is then defined as a positive-valued wall-transverse ridge of the $\bar{\kappa}_{t_0}^{t_0+T}$ field (Serra *et al.* [91] for details). Later position of the backbone $\mathcal{B}(t)$ can be computed by materially advecting $\mathcal{B}(t_0)$, i.e., letting $\mathcal{B}(t) := \mathbf{F}_{t_0}^t(\mathcal{B}(t_0)),\ t\in[t_0,t_0+T]$. If $\mathcal{B}(t_0)$ connects to the wall transversally, the intersection point is called the Lagrangian spiking point and is defined by

$$(s_p,0) := \mathcal{B}(t_0)\cap\text{no-slip wall}. \quad (24)$$

Serra *et al.* [91] derived also alternative exact formulas for the Lagrangian spiking point using only on-wall Eulerian quantities in the case of steady, time periodic and generally aperiodic flows (cf. Table 4). Finally, in the instantaneous limit ($T=0$), the Lagrangian backbone of separation and spiking point turns into their correspondent Eulerian versions (Serra *et al.* [91]).

In Table 4, $\hat{v}$ indicates the velocity in normal direction to the wall, and can be computed from the inner product:

$$\hat{v} = \langle\mathbf{v},\mathbf{n}\rangle = un_x + vn_y, \quad \mathbf{n} := \mathbf{R}\frac{\mathbf{r}'_\eta}{|\mathbf{r}'_\eta|}, \quad |\mathbf{r}'_\eta| = \sqrt{\langle\mathbf{r}'_\eta,\mathbf{r}'_\eta\rangle}. \quad (25)$$

Lagrangian spiking point : $(s_p,0)$	
$\nabla\cdot\mathbf{v}\neq 0$	$\nabla\cdot\mathbf{v}=0$
$\begin{cases}\int_{t_0}^{t_0+T}\partial_{sssn}\hat{v}\,(s_p,0,t)=0,\\ \int_{t_0}^{t_0+T}\partial_{ssssn}\hat{v}\,(s_p,0,t)>0,\\ \int_{t_0}^{t_0+T}\partial_{ssn}\hat{v}\,(s_p,0,t)<0.\end{cases}$	$\begin{cases}\int_{t_0}^{t_0+T}\partial_{sssnn}\hat{v}\,(s_p,0,t)=0,\\ \int_{t_0}^{t_0+T}\partial_{ssssnn}\hat{v}\,(s_p,0,t)>0,\\ \int_{t_0}^{t_0+T}\partial_{ssnn}\hat{v}\,(s_p,0,t)<0,\end{cases}$

Table 4: Equations determining the Lagrangian spiking point for generally aperiodic compressible (left) and incompressible (right) flows on a no-slip boundary in terms of on-wall Eulerian quantities. $\hat{v}$ indicates the velocity direction normal to the wall.

Assuming a curved, parametrized boundary $\mathcal{W}(s)$, the normal vector $\mathbf{n}$ at each collocation point $\mathbf{x}_i$ is the vector pointing to the closest intersection point with the boundary $\mathcal{W}$ and found by minimizing the distance function $d_i(s) = |\mathbf{x}_i - \mathcal{W}(s)|$. If we assume a continuous and sufficiently smooth function $\hat{v}$, we can switch the order of differentiation in Table 4 and compute the normal gradients first. Once the normal velocity is obtained at each collocation point, the gradient can be computed by multiplication with the derivative matrix $\mathcal{D}$. Using the spectral operator $\mathcal{D}$ gives the derivatives in x- and y-direction in the polynomial order of the scheme.

$$\nabla \hat{v} = \mathcal{D}\hat{v}. \tag{26}$$

The directional derivative of the normal velocity $\hat{v}$ in direction of the wall-normal vector $\mathbf{n}$ is computed as

$$\partial_\eta \hat{v} = \nabla_{\mathbf{n}} \hat{v} = \nabla \hat{v} \cdot \mathbf{n} = (\partial_x \hat{v})\, n_x + (\partial_y \hat{v})\, n_y. \tag{27}$$

This relation allows us to calculate the normal derivatives everywhere in the flow field from the velocity gradient and the normal vector at each point. Once $\partial_\eta \hat{v}$ or $\partial_{\eta\eta} \hat{v}$ are determined, the derivatives tangential to the wall can be computed subsequently.

8.1.1 Lagrangian Particle Tracking

Lagrangian particles are traced by spectrally interpolating the velocity field for each particle and numerically integrating $\dot{\mathbf{x}}(\mathbf{x}, t) = \mathbf{v}(\mathbf{x}(t), t)$ using a 3rd order Adam-Bashfort scheme. We take advantage of the *gslib* library for efficient particle tracking and velocity interpolation, as described by Mittal *et al.* [92].

8.2 Problem setup

The canonical circular cylinder flow is computed at a Reynolds number of $Re_d = 100$ based on a cylinder diameter of unity and Mach number of 0.1, rendering compressibility effects negligible. The computational domain is divided into 347 quadrilateral elements and the solution is approximated with a 16th order polynomial. This accounts to a total of 100,283 collocation points. At the outer boundaries, a free stream condition is applied while the cylinder is approximated with curved element faces and an adiabatic no-slip wall. 402,201 Lagrangian particles are initialized in 201 wall-parallel lines around the cylinder with a spacing of Δ/d = 0.001 between each line.

The flow over a NACA 65(1)-412 airfoil is simulated at a Reynolds number based on the chord length of $Re_c = 20,000$ and a Mach number of $M = 0.3$. The Mach number is relatively low ensuring a nominally incompressible flow, but it is high enough to prevent stability issues pertaining to the explicit time integration we use. The computational domain consists of 2,256 quadrilateral elements, with the dimensions of the domain being adopted from Jones *et al.* [82]. The boundary elements are curved and fitted to a spline representing the airfoil's surface according to Nelson *et al.* [78]. Boundary conditions at outer edges of the computational domain are specified as free-stream boundaries while the airfoil surface is treated as a non-slip, adiabatic wall. The solution vector is approximated with a 16th order polynomial, giving a total of 651,984 collocation points in the domain. 1,005,201 Lagrangian particles are initialized in 201 wall-parallel lines around the airfoil with a spacing of Δ/c = 0.0002 between each line.

The wall-normal derivatives in Table 4 are computed within the DGSEM solver. With Equations 25 and 27, the quantities $\hat{v}_\eta$ and $\hat{v}_{\eta\eta}$ can be spectrally computed in each element using the operators available in the DGSEM framework and subsequently interpolated to the wall. The derivatives in wall-tangential direction can either be computed within the DGSEM solver or as part of the post-processing work. Given the sensitive nature to numerical noise of second and higher derivatives, a smoothing filter is applied to the DNS output data as a post-processing step.

8.3 Results and discussion

8.3.1 Cylinder flow

To study the kinematics of flow separation, we consider a cylinder flow at $Re_d = 100$. Ridges in the FTLE field show a flow pattern that is well-known to be dominated by a pair of counter-rotating vortices alternately shedding in a regular manner from the top and bottom of the cylinder with a period of approximately six convective time units [93, 94]. A snapshot of the backward-time FTLE (Figure 29) reveals the long-term attracting LCSs in the wake, which highlight the edges of the advected vortices. Although this LCS is associated with separation (see Lipinski *et al.* [95]) and with early vortex formation and shedding [94], the FTLE ridge cannot intersect with the cylinder wall but rather envelopes the body. This is a direct consequence of the no-slip condition at the wall and non-hyperbolicity, as was explained in the introduction. The exact on-wall origin of separation can hence not be identified solely based on a strain-based FTLE field. A more rigorous analysis of the near-wall flow field is required. To this end, we first determine the

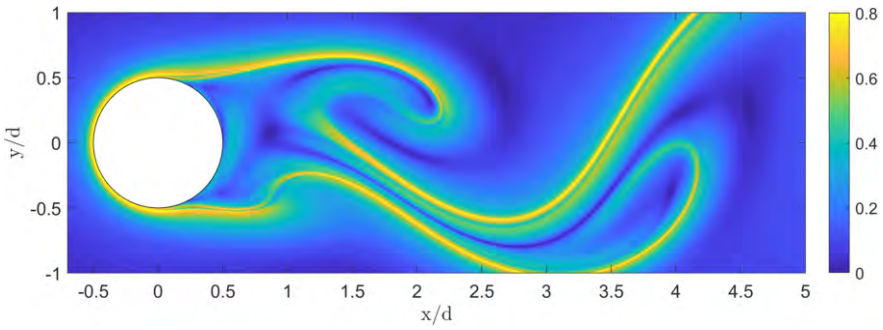

Figure 29: Backward-time FTLE from integration over one vortex shedding period.

asymptotic separation point and line [35] and then compute the Lagrangian curvature change $\bar{\kappa}_{t_0}^{t_0+T}$ and associated spiking dynamics. Later, we will relate the material spiking and the FTLE.

The averaged zero-skin-friction point is determined according to Eq. 10 with the temporal mean of the skin friction coefficient over one vortex shedding period. It is located at $x/d = 0.23$, approximately half way between center and the rear end of the cylinder. The angle of the separation line with respect to the tangent of the cylinder surface at the separation point is determined with Eq. 11. It oscillates periodically between 34° and 57°. We use the angle and separation point to create a linear approximation of the unstable manifold to which fluid particles that eject from the wall are asymptotically attracted.

The near-wall dynamics are visualized in Figure 30, where color-coded fluid tracers, the linear separation profile and instantaneous streamlines are plotted for different integration times, T. Particles up- and downstream of the line undergo an initial upwelling (spiking) and are drawn towards the unstable manifold.

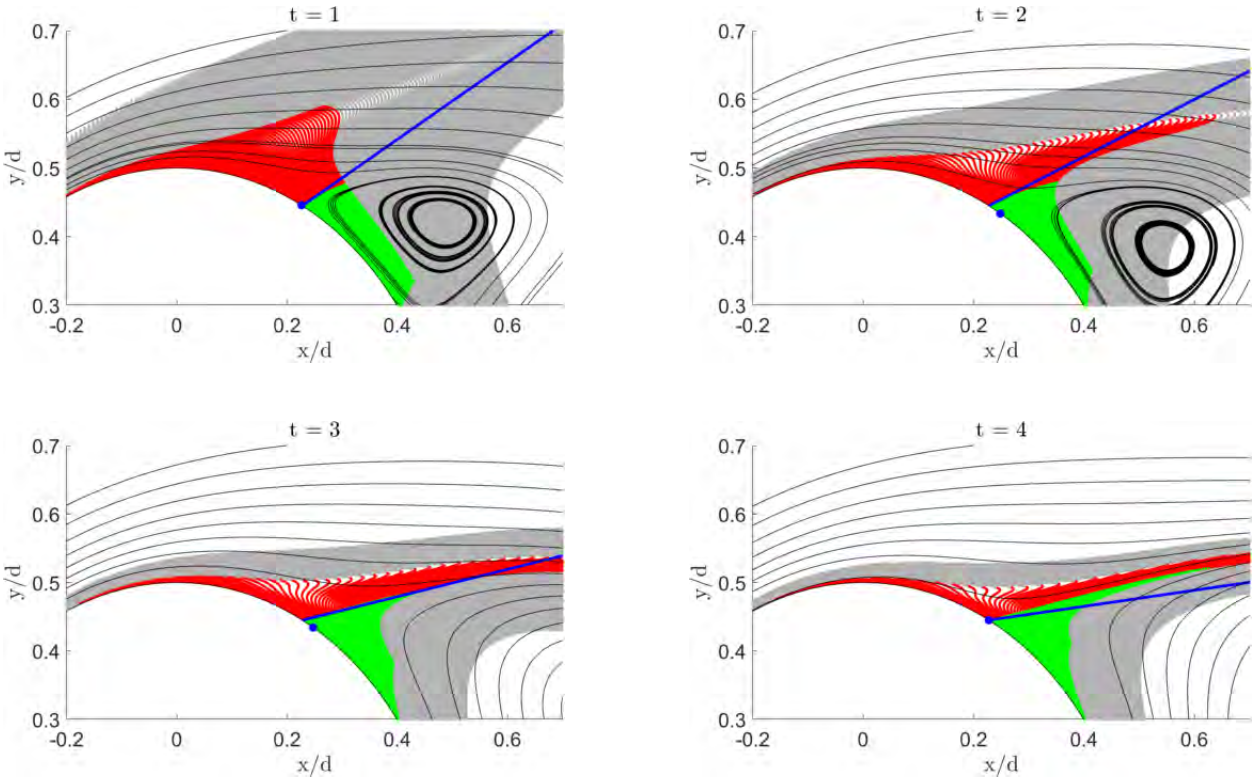

Figure 30: Advection of particles over the cylinder near the separation point. Particles divided by linear separation line (blue) in upstream (red) and downstream (green). Zero-skin-friction point in blue, streamlines in black.

To identify the onset of flow separation, i.e. the origin of material spiking, we extract a backbone from the evolution of the material lines through ridges in the corresponding advected curvature field $\bar{\kappa}_{t_0}^{t_0+T}$. We plot the curvature field for integration times of T = [0.1, 0.4, 0.7, 1.0], and $t_0 = 0$ in Figure 31. Note that we first compute $\bar{\kappa}_{t_0}^{t_0+T}$, which is a scalar field based at t_0, and then advect it with $\mathbf{F}_{t_0}^{t_0+T}$. The latter operation reflects the material property of lines and the backbone, $\mathcal{B}(t_0+T) := \mathbf{F}_{t_0}^{t_0+T}(\mathcal{B}(t_0))$. The backbone, $\mathcal{B}(t)$, shown in magenta. For reference, we also plot the instantaneous zero-skin-friction point and the linear approximation of the separation profile in green.

The evolution of material lines in Figure 31 show that the backbone profile $\mathcal{B}(t)$ is correctly placed along the local spikes of material lines and intersects with the wall shortly upstream of the center of the cylinder. The separated fluid tracers then follow the direction of the linearly approximated separation profile. While the asymptotic separation profile provides information about the long-term behavior of separating fluid tracers, the initial material spike formation remains hidden and can only be extracted from analysis of the curvature scalar field.

The curvature change field $\bar{\kappa}_{t_0}^{t_0+T}$ for integration time intervals of T = 0.4 and 1.0 in Figure 32 reveal a total number of four Lagrangian backbones. Two originate from the top and the bottom of the cylinder and evolve along a dominant, growing ridge in the curvature field driven by the separation of the boundary layer. The two other backbones are located within the recirculation region in the separated cylinder wake. They are based on much weaker curvature ridges and we therefore deem them of secondary interest in the onset of separation.

Spiking phenomenon and FTLE The spike formation, which occurs over short time, is hidden to the FTLE field [91]. For longer integration times, however, the material spike, governed by off-wall dynamics, converge to the attracting backward-time FTLE ridge. For the cylinder case, we visualize the spatial relation between the backbone, material lines and the backward-time FTLE field at different time instances in Figure 33. In this figure, a time interval of one vortex shedding period, T = 6, is used to compute the FTLE field. Material lines and the backbone are advected from t = 0 to t = 1, 2, 3, and 4 (black).

Initially, the fluid tracers undergo an upward motion in transverse direction to the cylinder and the backbone along the material spike crosses the FTLE ridge (t = 1). As the integration time increases, however, the material lines bend downwards (t = 2) and gradually align with the unstable manifold for $t \geq 3$. The long-term manifold identified through the backward-time FTLE ridge attracts the separating fluid material and gradually aligns with the material backbone. The trace of the separated fluid in the wake follows the same pattern and shows long-term sharp spikes along dominant FTLE ridges, as illustrated in Figure 34.

The above results highlight that the Lagrangian backbones of separation and the FTLE provide critical complementary structures in the analysis of Lagrangian flow separation. While the initial motion through upwelling of fluid material can only be determined through the analysis of the curvature change field [91], the long-term off-wall dynamics are governed by the FTLE. A combination of both methodologies therefore, together with the asymptotic separation line, gives a complete picture of the kinematics of separation.

Extraction of spiking points The spiking points, s_p, are the wall signatures of material upwelling and can either be identified from the intersection of a wall-transverse curvature change ridge with the boundary (Eq. (24)) or from on-wall Eulerian derivatives of the wall-normal velocity (Table 4). Here, we extract s_p using the criterion for incompressible flows, since the flow with a free-stream Mach number of M = 0.1 is nearly incompressible

From the condition specified in Table 4, the spiking points are located at minima of the integrated derivatives of the normal velocity in normal and tangential direction, $\int_{t_0}^{t_0+T} \partial_{\eta\eta ss}\hat{v}dt$. We plot this function in Figure 35 (a) for the upper half of the cylinder and an interval of T = 1. The resulting spiking points are indicated with red circles. Figure 35 (b) shows the curvature change field $\bar{\kappa}_0^1$ and the Lagrangian backbones of separation $\mathcal{B}(t_0)$ in magenta. The spiking points identified from the normal velocity derivatives are plotted as red dots at the boundary and match exactly with the intersection of the backbones and the wall. Through the agreement of the spiking points determined from Eulerian on-wall quantities and the alternative Lagrangian definition (Eq. (24)), here, we verify the theory by Serra *et al.* [91] *for the first time*, i.e. we confirm the theory that material upwelling in the Lagrangian frame can be captured also by using wall-based Eulerian quantities only.

Figure 36 shows the curvature change field, based at the initial time, on the upper side of the cylinder for increasing integration times, together with the Lagrangian spiking points from on-wall quantities (red), backbones of separation (magenta), and boundary layer approximations based on the momentum and displacement thickness in grey and black respectively. These plots are based on the same particle trace that is used in the previous Figures 31, 32, and 35 (b). The Lagrangian spiking point s_p is located at x/d = -0.09, which places it far upstream of the asymptotic separation point (x/d = 0.23) and, remarkably, even upstream from the cylinder center.

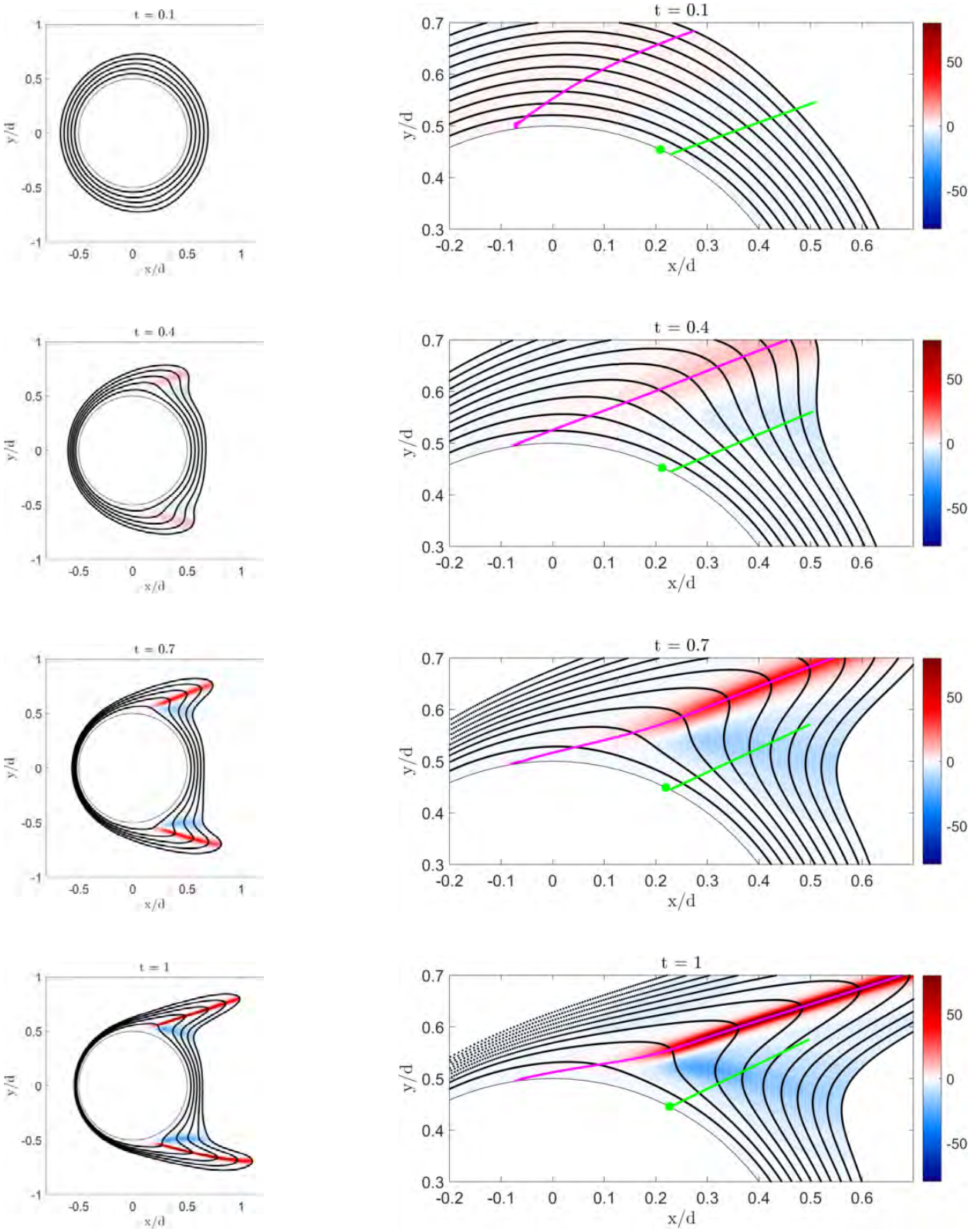

Figure 31: Advection of material lines and the curvature field $\bar{\kappa}^t_{t_0}$, $t = t_0+T$ around a cylinder for different integration times. The backbone $\mathcal{B}(t)$ is highlighted in magenta. Linear separation line and zero-skin-friction point in green.

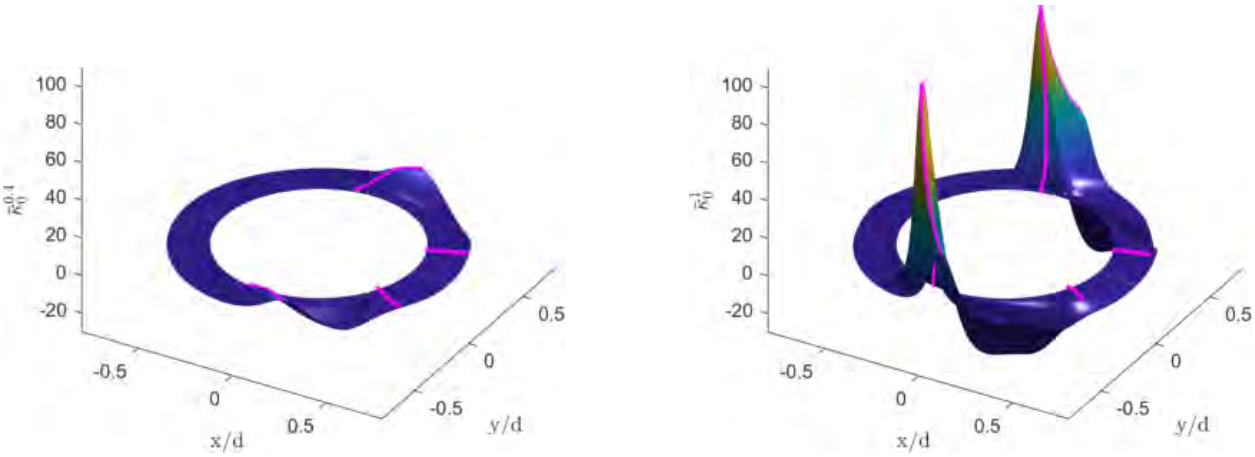

Figure 32: Surface plot of the curvature scalar fields $\bar{\kappa}_0^{0.4}$ and $\bar{\kappa}_0^{1}$. Backbone of separation in magenta.

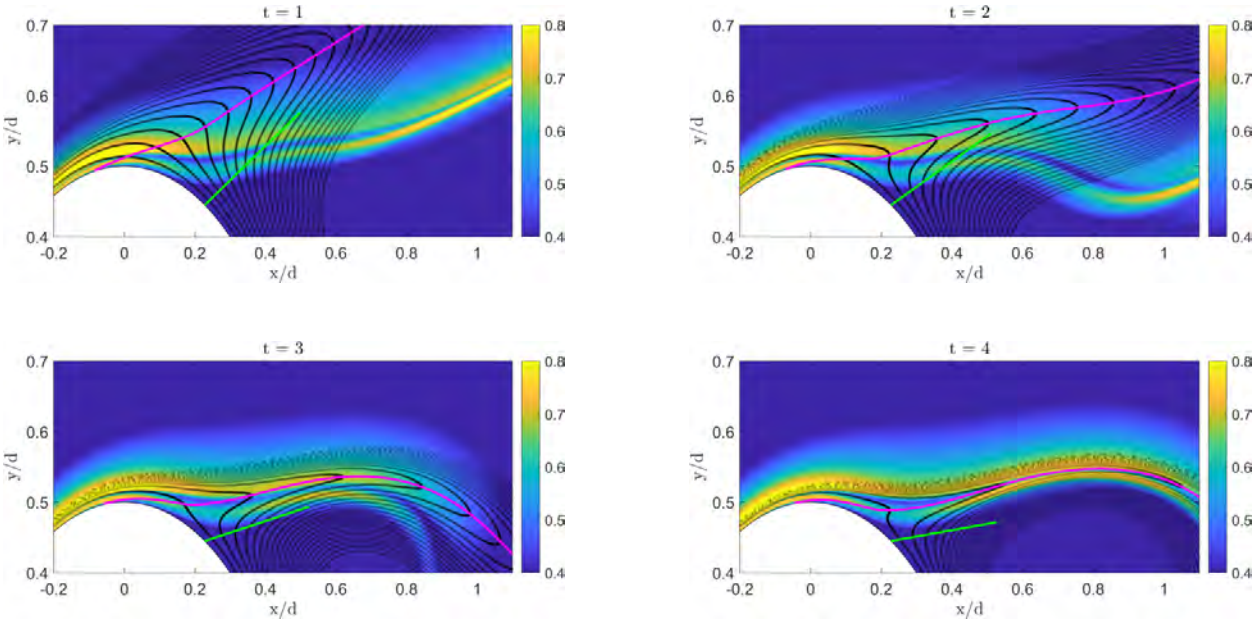

Figure 33: Backward-time FTLE field (contour plot) computed from t to $t - T$ over $T = 6$. Advected material lines from 0 to t in black and the Lagrangian backbone of separation in magenta. Asymptotic separation profile in green. Y-axis stretched.

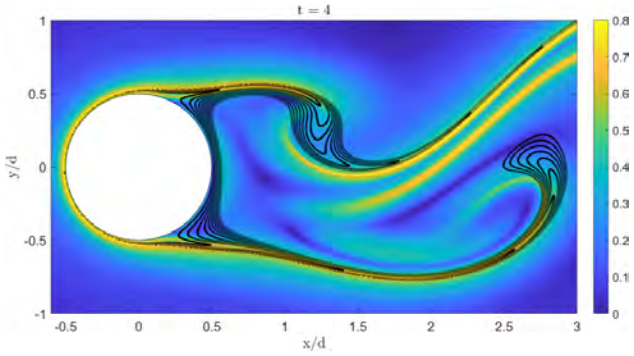

Figure 34: Backward-time FTLE and material lines in the wake.

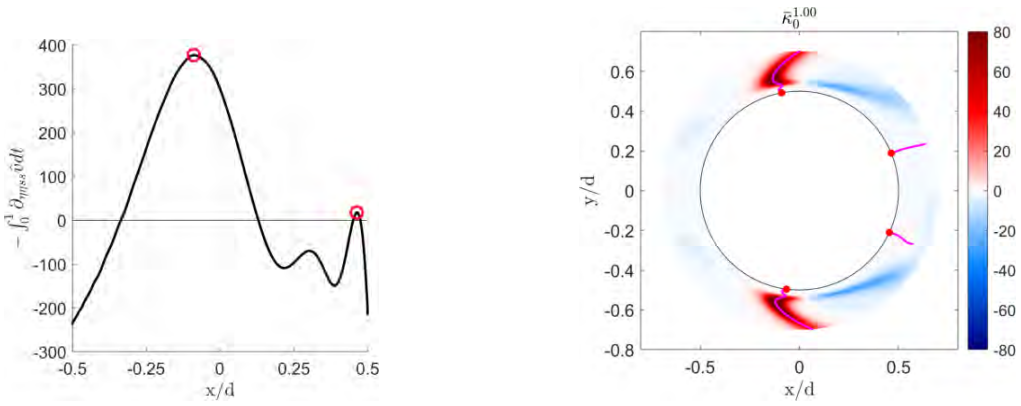

(a) (b)

Figure 35: (a) $-\int_0^1 \partial_{\eta ss}\hat{v}dt$ with spiking points in red. (b) Curvature change field $\bar{\kappa}_0^1$ with backbones (magenta) and Lagrangian spiking points (red) identified from Eulerian on-wall quantities.

We find that there is a strong correlation between the curvature change field and the boundary layer scaling thicknesses, such as the displacement thickness and momentum loss thickness [3]. Figure 36 shows that, as the integration time increases, ridges of $\bar{\kappa}_{t_0}^{t_0+T}$ form and develop a peak at the intersection with the displacement thickness (black line). Within the momentum thickness layer (grey line), the curvature of the ridge abruptly decreases. The dependence of the backbone of separation on the displacement and momentum thickness is a remarkable result, as boundary layer thicknesses follow kinetic arguments and typically involve thresholds parameters. Inflection of the backbone of separation, in contrast, despite being threshold free and purely kinematic, accurately separate on- and off-wall regions characterized by different dynamics. We are currently exploring this correlation in material and plan to report on this in the near future.

We note that even though the curvature change ridge develops a 'nose' and moves upstream with increasing integration time, the backbone $\mathcal{B}(t_0)$ maintains its original on-wall signature and intersects the wall at the spiking points identified by the criteria in Table 4.

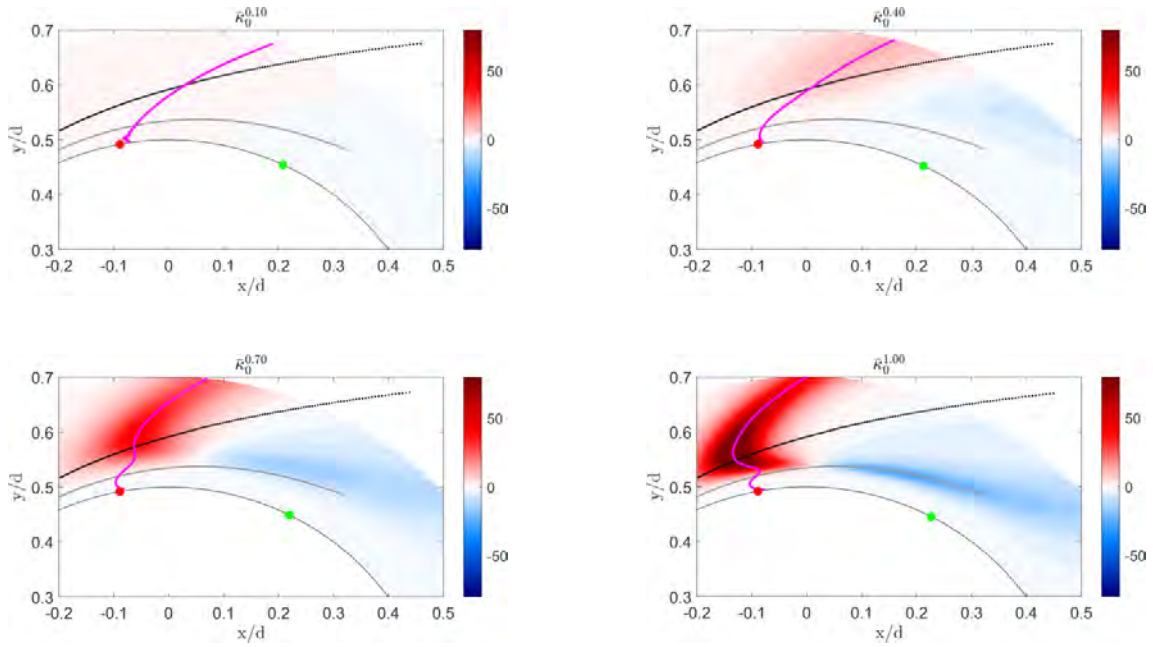

Figure 36: Lagrangian curvature change field with the corresponding backbone of separation (magenta) and Lagrangian spiking points (red) identified from Eulerian on-wall quantities for different integration times. Zero-skin-friction point in green, boundary layer displacement thickness in black and momentum thickness in grey.

8.3.2 Airfoil flow

For a more complex and encompassing external aerodynamics test case, we study the kinematics of flow separation on a cambered NACA 65(1)-412 airfoil at a chord-based Reynolds number of $Re_c = 20,000$ and 4° angle of attack. The low Reynolds airfoil flow is characterized by boundary layer separation at mid-cord, a recirculation region downstream of the separation location and a Von-Karmann-type vortex shedding in the wake, resulting in a time-periodic flow pattern with a period of $T = 0.36$.

A snapshot of the backward-time FTLE (Figure 37) visualizes the separated shear layer and the edges of the shedded and advected vortices.

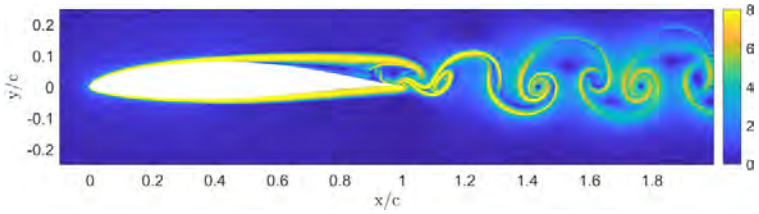

Figure 37: Backward-time FTLE from integration over one vortex shedding period.

The asymptotic separation point is computing using the mean over one vortex shedding period, and is located at the averaged zero-skin-friction point at $x/c = 0.50$, i.e. exactly at mid-cord, slighly behind the maximum thickness location of the airfoil ($x/c = 0.4$). This is in accordance with thre result reported in Nelson *et al.* [78] and Kamphuis *et al.* [96]. The angle of the separation line with respect to the tangent of the airfoil surface periodically oscillates between 7.05° and 7.5°. These near-wall dynamics are summarized in Figure 38, where color-coded fluid tracers, the asymptotic separation profile and instantaneous streamlines are plotted for different integration times. Similar to the cylinder flow, the particles upstream of the asymptotic separation point undergo an upwelling motion and form a sharp spike that will be later guided by an attracting LCS in the flow.

The advected curvature change field at the final time, together with a set of material lines, is shown in Figure 39 for different integration times. Multiple spikes emerge on the suction side of the airfoil: a dominant ridge evolves along

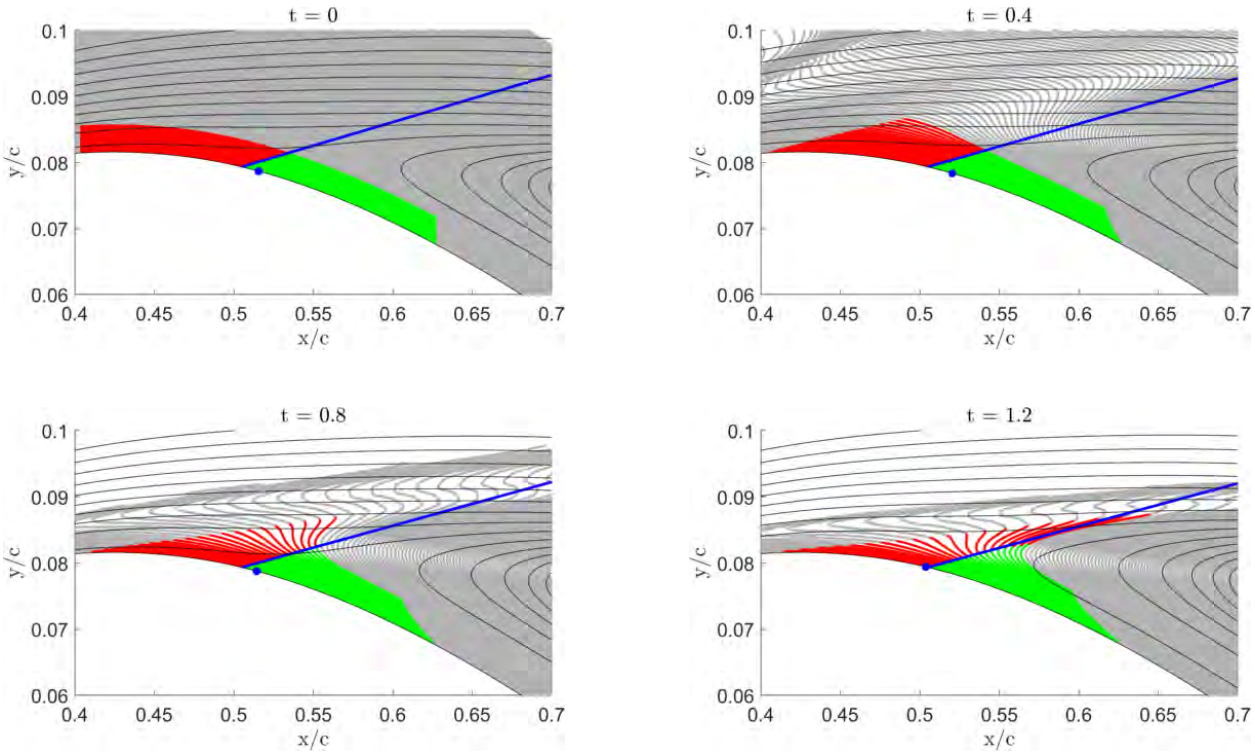

Figure 38: Advection of particles over the airfoil near the asymptotic separation point. Particles divided by the asymptotic linear separation line (blue) in upstream (red) and downstream (green) locations. Zero-skin-friction point in blue, streamlines in black.

the separating shear layer and several smaller spikes appear within the separated recirculation region. On the pressure (bottom) side, the flow remains attached and the fluid tracers are advected without breaking away from the boundary until the trailing edge is reached. Given that global separation occurs only on the suction side of the airfoil, we focus our analysis on the upper section of the profile. A magnified view of the curvature scalar field introduced in Figure 39, together with the backbone of separation $\mathcal{B}(t)$ and the asymptotic separation profile is given in Figure 40. Note that the y-axis is stretched to aid visibility of subtle features.

The backbone emerging at mid-cord is based on the upwelling of separating material lines in the vicinity of the asymptotic separation line and intersects the no-slip wall at s_p/c = 0.46. This location is slightly upstream of the asymptotic separation point at x/c = 0.5. Additional curvature ridges are detected within the separated recirculation region, but, given that the boundary layer has already separated, are of little interest for determining the start of Lagrangian flow separation.

Spiking phenomenon and FTLE The relation between the Lagrangian backbone of separation, material lines, and the backward-time FTLE field is illustrated in Figure 41 at different snapshots in time. To determine the backward-time FTLE field, again, we use an integration time interval equal to one vortex shedding period (T = 0.36). Material lines (black) and backbones (magenta) are advected forward in time from t = 0 to t = 0.05, 0.1, 0.2, 0.3, 0.4, and 0.5.

Similar to our findings for the cylinder flow, the material spike starts from the no-slip wall, crossing the FTLE ridge at short time scales. As the integration time increases, the material spike, along with the backbone of separation, aligns to the attracting FTLE ridge, which again governs the off-wall dynamics of the separated fluid tracers. The separation picture is then completed by the asymptotic separation line (green) and its connection to backward-time FTLE ridge (see Figure 41).

Extraction of spiking points We extract the spiking points of the separating airfoil flow from both their Lagrangian and wall-based Eulerian definitions. The curvature change field $\bar{\kappa}_{t_0}^{t_0+T}$ is given in Figure 42 for three different integration intervals in x and η coordinates, where η is the wall-normal distance. Besides the large ridges at mid-cord and

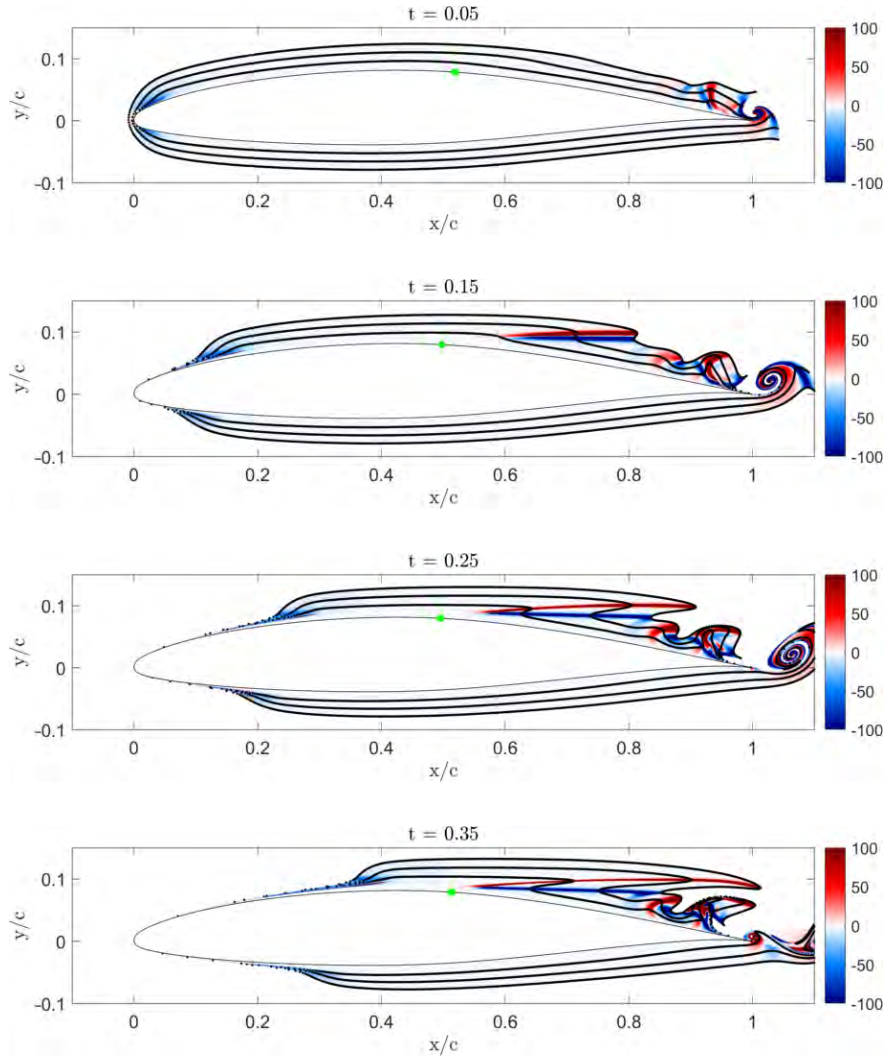

Figure 39: Advection of material lines and the curvature field $\bar{\kappa}_{t_0}^{t_0+T}$ around the airfoil for different integration times. Zero-skin-friction point in green.

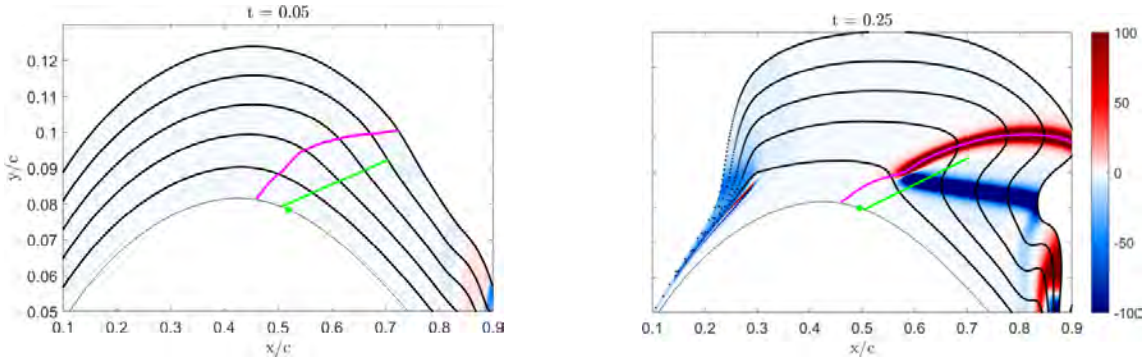

Figure 40: Advected curvature scalar field with material lines (black) and the Lagrangian backbone of separation $\mathcal{B}(t)$ (magenta). Zero-skin-friction point and linear separation line in green. Y-axis stretched.

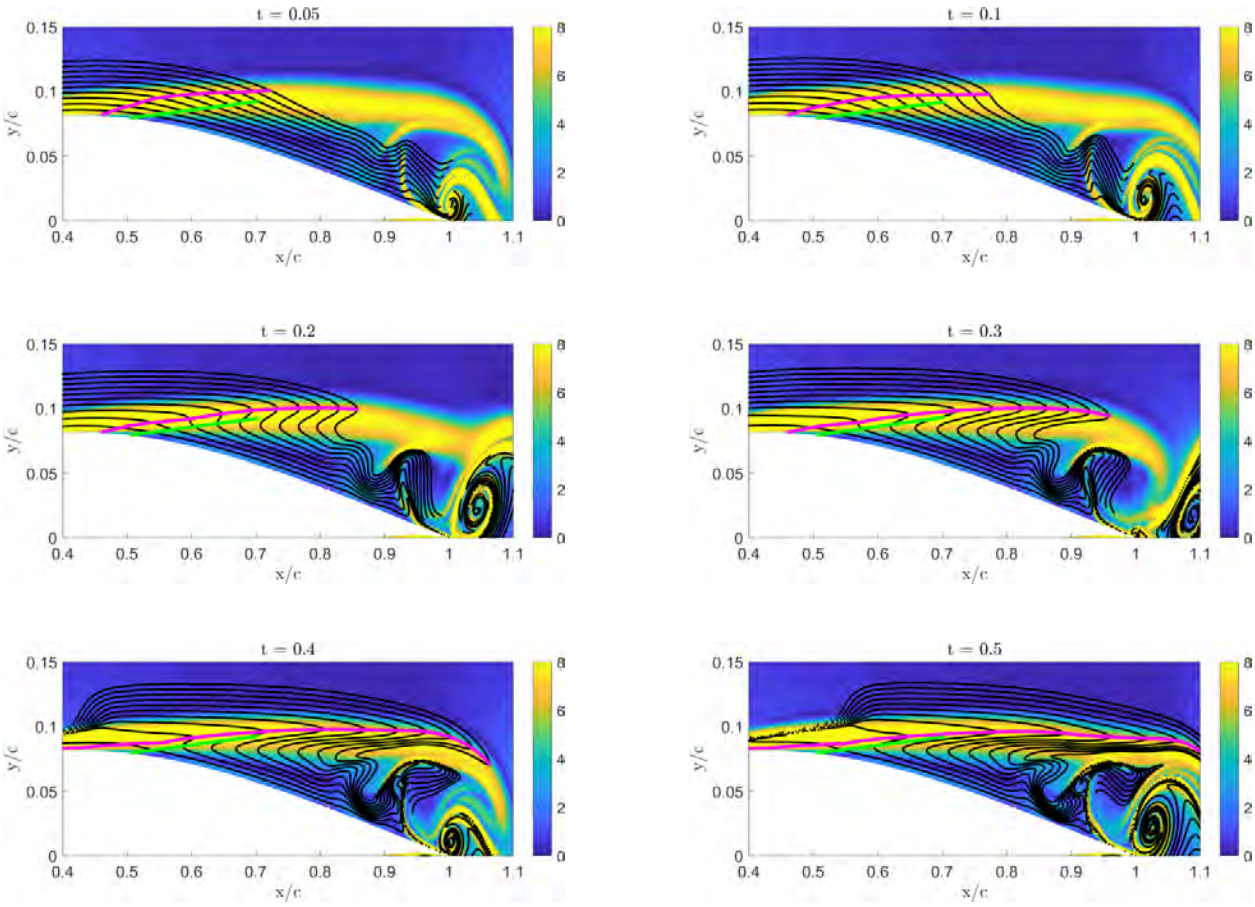

Figure 41: Backward-time FTLE field (contour plot) computed from t to $t - T$ over $T = 0.36$. Advected material lines from 0 to t in black and the Lagrangian backbone of separation in magenta. Asymptotic separation profile in green. Y-axis stretched.

at $x/c \approx 0.75$, a weak waviness in the curvature field exists upstream of the asymptotic separation point ($x/c = 0.5$). This oscillatory pattern is recovered in the Eulerian wall derivative $\int_0^{0.25} \partial_{\eta\eta ss}\hat{v}dt$, shown on left of Figure 43.

According to the conditions specified in Table 4, spiking points are located at local maxima of the function $-\int_{t_0}^{t_0+T} \partial_{\eta\eta ss}\hat{v}dt$, which identifies three locations upstream of the separation point in Figure 43 (a). Weak curvature ridges are present at these locations that we found are not contributing to material spiking and fluid break away in the context of flow separation. The oscillatory curvature field and associated ridges correlate directly with the piecewise linear curvature κ_0 of the airfoil surface representation (dashed line) that is inherent to the cubic spline boundary representation used for the design of the airfoil. The three ridges are hence a geometric artifact and should not be interpreted as significant spiking events.

We can reduce the oscillatory trend from the spline parametrization by filtering the function $\int_{t_0}^{t_0+T} \partial_{\eta\eta ss}\hat{v}dt$ with a kernel width based on the approximate distance between two spline segments. The filtered solution (red line) successfully recovers the underlying correct function and identifies a single spiking point at $x/c = 0.45$ (red circle) upstream of the separation point.

Figure 43 (b) shows the curvature scalar field $\bar{\kappa}_0^{0.25}$ at t_0 in x and y coordinates with the ridge highlighted in magenta and the spiking point from Eulerian on-wall quantities in red. With the close match of the backbone-wall intersection at $x/c = 0.46$ and the Eulerian criterion at $x/c = 0.45$, we demonstrate that the spiking point can be extracted from on-wall based quantities even with approximate parametrization of the boundary, as used in engineering applications.

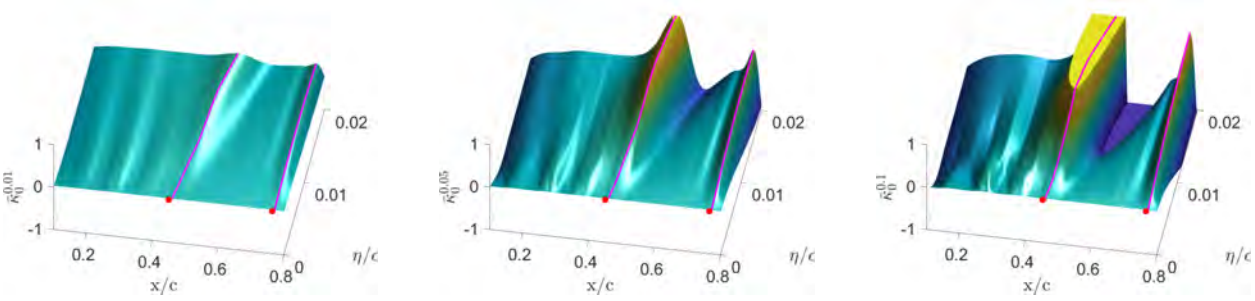

Figure 42: Surface plot of the curvature scalar field $\bar{\kappa}_{t_0}^{t_0+T}$ for T = 0.01, 0.05, and 0.10. Wall-normal coordinate on y-axis. Backbone in magenta, spiking point in red.

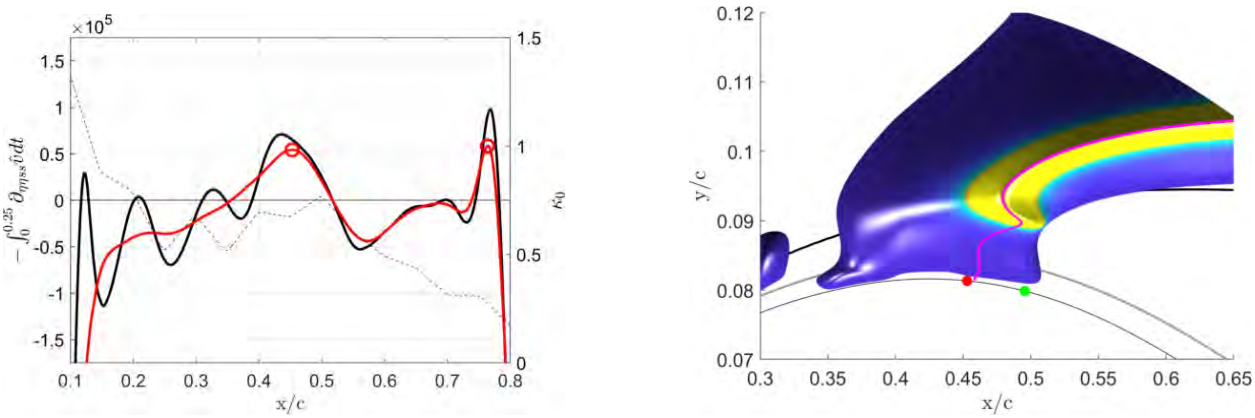

Figure 43: (a) $-\int_0^{0.25} \partial_{\eta\eta ss}\hat{v}dt$ in black. Filtered results and Spiking points in red. Surface curvature κ_0 as dashed line. (b) Curvature change field $log(\bar{\kappa}_0^{0.25})$ at $\mathbf{x}_0$ with backbone (magenta) and Lagrangian spiking point (red) identified from Eulerian on-wall quantities. Displacement thickness in black and momentum thickness in grey. Zero-skin-friction point in green.

9 A Combined Theoretical and Numerical Investigation of Airfoil Response Sensitivities

The theory of separation suggests that optimal control may not be at the asymptotic separation location but rather somewhere upstream from that location near the first upwellings of the flow at the origin of the backbone. Through a systematic computational and theoretical approach, we have explored optimal actuator locations for separation control from input-output response data, gathered from numerical simulations. This research has been submitted to Theoretical and Computational Fluid Dynamics [97].

9.1 Pulse response of separated flow

To understand general sensitivity of the Lagrangian separation and connected separation lines to control, we subject the NACA 65(1)-412 airfoil flow to pulse actuation in the boundary layer. The lessons learned from pulse actuation provide the basis for the determination of the optimal placement of actuators [98] and associated development of an active feedback control. A computational parametric study is performed on the effect of pulse location over the suction side of the airfoil. For most of the control location, the pulse induces a flow perturbation (Fig. 44a) that is transported along the top of the shear layer. To different degrees depending on the control location, the perturbation grows as it travels downstream (Fig. 44a-d) inducing a Kelvin-Helmholtz like instability (Fig. 44b). A vortex pair forms on the suction side of the airfoil (Fig. 44c). While one of these vortices, V_4, sheds quickly (Figs. 44c and d), the second vortex, V_3, resides in the circulation region and grows in size. Coinciding with the shedding of the first vortex, the separated LCS wraps around vortex V_3 in Figures 44c and d) and aligns with the airfoil surface. This corresponds to a downward deflection of the separated shear layer towards the airfoil surface. and a reduction of the size of the

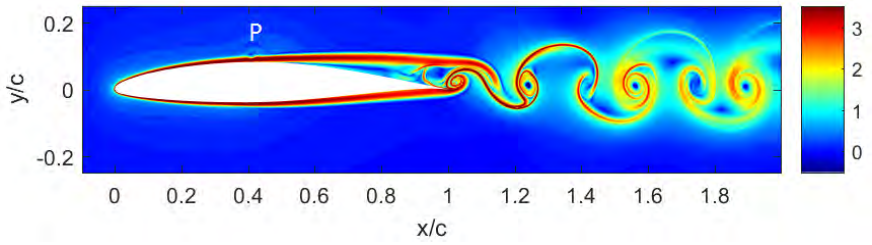

(a) t=10.01

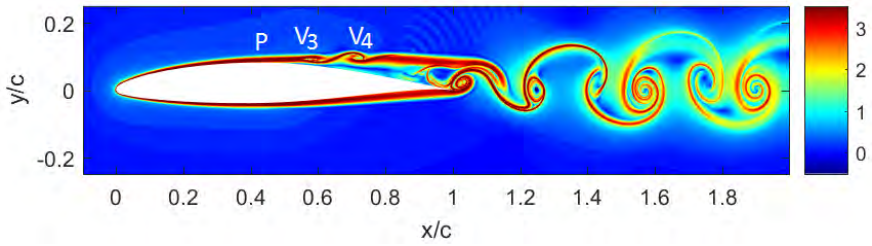

(b) t=10.4

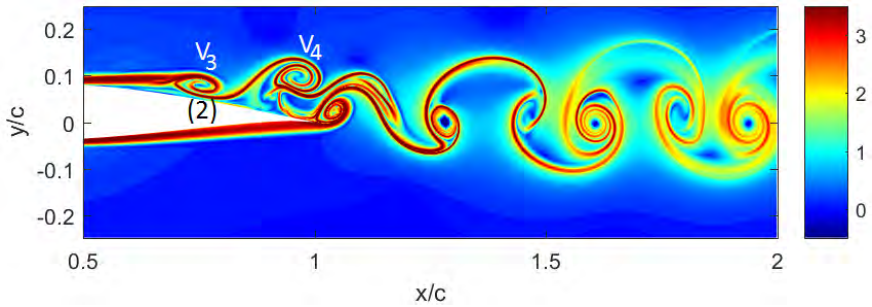

(c) t=10.8

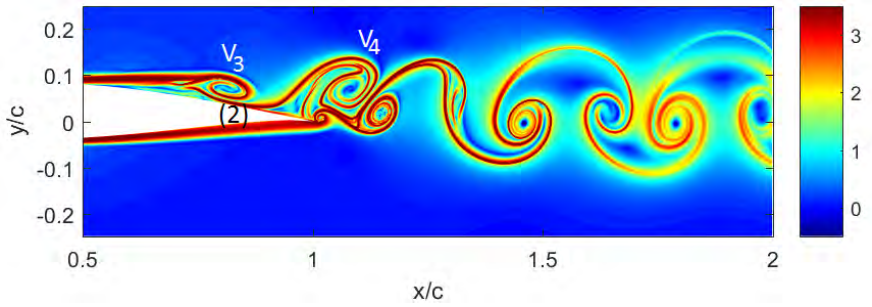

(d) t=11.0

Figure 44: NACA 65(1)-412, $\alpha = 4°$, $Re_c = 20,000$, backward-time FTLE field near the wake at (a) t=10.01, (b) t=10.4, (c) t=10.8, and (d) t=11.0 for the case with a pulse actuation at $x/c = 0.4$

recirculation area. This in turn yields a decrease in the pressure drag. Vortex V_4 also increases the vorticity in the recirculation area. This leads to an increase in the lift.

The time series of the lift coefficient for all cases is shown in Figure 45. Pulse actuation near the separation point, can increase the instantaneous lift coefficient up to 40%. This increase is accompanied by significant flow reattachment.

9.2 Eigensystem Realization Algorithm and optimal control location

Using the Eigensystem Realization Algorithm [99], state-space descriptions can be extracted from the lift response data associated with a candidate set of actuator locations. These system realizations form the basis for a theoretical analysis that determines the actuator location among the set that can drive the system output to an arbitrary value with

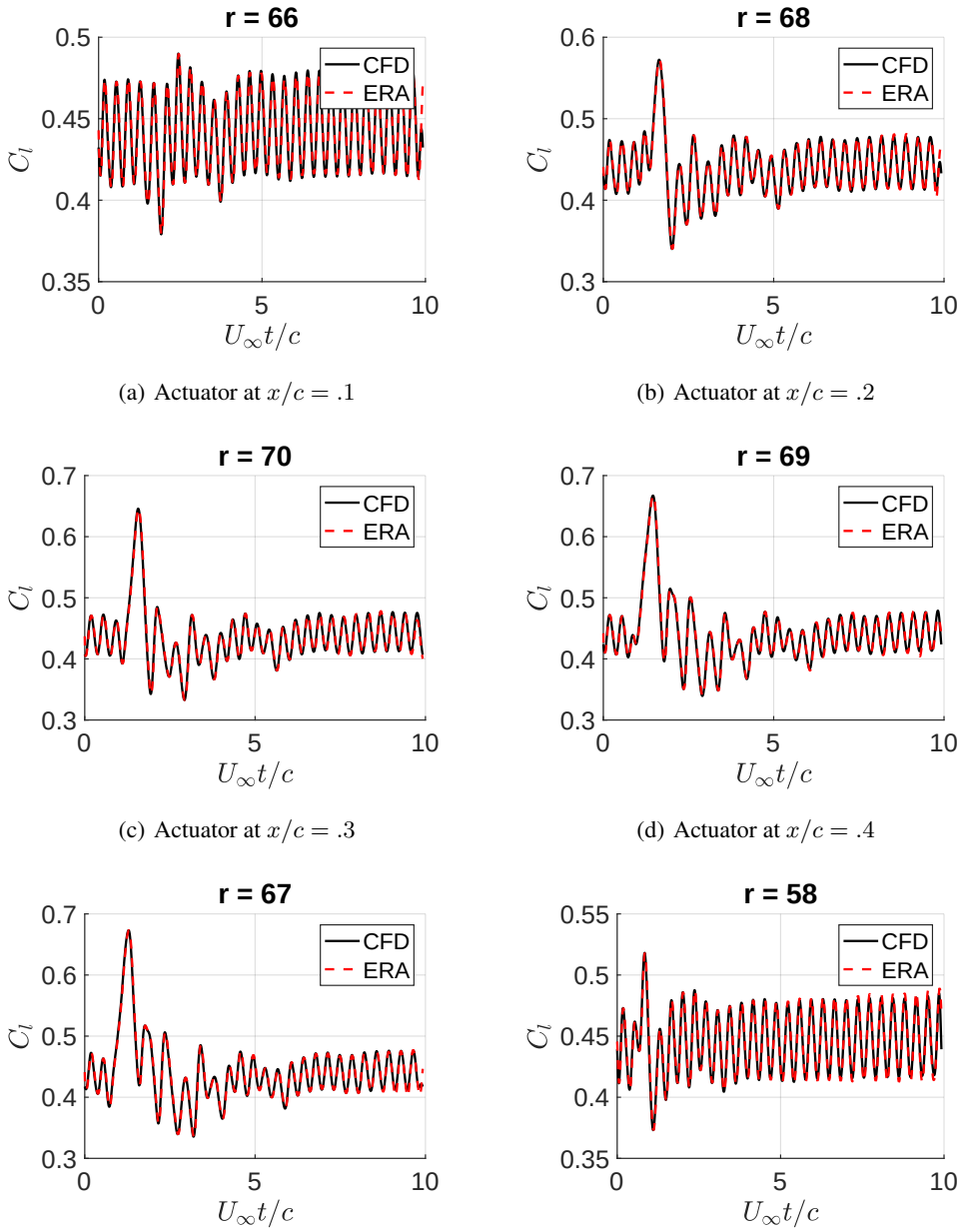

(a) Actuator at $x/c = .1$

(b) Actuator at $x/c = .2$

(c) Actuator at $x/c = .3$

(d) Actuator at $x/c = .4$

(e) Actuator at $x/c = .5$

(f) Actuator at $x/c = .6$

Figure 45: Lift coefficient pulse response data at each actuator location determined from CFD calculations and fitted with the Eigensystem Realization Algorithm (ERA). Each realization is minimal with order r.

minimal control effort. The solution of the corresponding minimum energy optimal control problem is evaluated by computing the generalized output controllability Gramian [100].

Specific steps involved in determining the optimal actuator location when the quantity of interest is the lift C_ℓ are as follows:

1. *Collect Data.* Collect sampled pulse response data $C_\ell^i(k)$ for each of the $i = 1, \ldots, N$ candidate actuator locations. Also, collect the uncontrolled baseline lift response $C_\ell^0(k)$ and compute its mean $\overline{C_\ell^0}$.

2. *Form Markov Parameters.* Subtract the uncontrolled baseline mean from each pulse response signal to obtain the associated sequence of Markov parameters $h_k^i = C_\ell^i(k) - \overline{C_\ell^0}$.
3. *Identify System Realizations.* Perform ERA on each sequence h_k^i to obtain a discrete-time system realization $\hat{G}^i = (\hat{A}^i, \hat{B}^i, \hat{C}^i)$. Convert this realization to a continuous-time realization $G^i = (A^i, B^i, C^i)$ via Tustin's approximation.
4. *Compute $\mathcal{H}_{2'}$ Optimality Measures.* For each system realization G^i, compute the generalized controllability Gramian P^i [100]. From this, compute the optimality measure $\|G^i\|_{2'} = \sqrt{C^i P {C^i}^\mathsf{T}}$ for each actuator location.
5. *Select Optimal Actuator.* Sort actuators according to decreasing $\mathcal{H}_{2'}$-norm. The optimal actuator location is the one associated with the largest value of $\|G^i\|_{2'}$.

The same procedure can be applied to analyze the optimal actuator location for controlling separation angle θ.

x/c	$\|G\|_{2'}$
.2	51.79
.6	31.31
.1	17.41
.5	15.81
.4	15.41
.3	13.41

Table 5: Optimality of actuator locations based on the generalized $\mathcal{H}_2$-norm, sorted from most to least optimal for different tolerance values used in minimal realization for lift response data.

Based on the $\mathcal{H}_{2'}$-norm as listed in Table 5, the optimal actuator location for lift control is $x/c = 0.2$. This location has the highest controllability among all six candidate locations.

As can be seen in Figure 45, the high order for the obtained minimal realizations, in all likeliness indicates that the system may have some degree of non-linearity in it, which is captured by a larger number of states. The peak frequency for all actuator locations is $fc/U_\infty = 6.12$, and corresponds to the wake frequency. Thus, it appears that among all actuator locations, $x/c = 0.2$ is able to induce a resonance by coupling with the flow dynamics at this forcing frequency. We find that the optimal location for controlling lift is different from the optimal location for controlling separation angle (see Table 6).

x/c	$\|G\|_{2'}$
.3	1.63×10^7
.5	3.99×10^4
.4	1059.57
.1	243.24
.6	91.95
.2	76.74

Table 6: Optimality of actuator locations based on the generalized $\mathcal{H}_2$-norm, sorted from most to least optimal for different tolerance values used in minimal realization for separation angle response data.

The results provide two interesting observations. First, the order of the minimal realizations obtained for the separation angle responses are an order of magnitude above the realizations associated with the lift responses. This suggests a greater degree of non-linearity associated with separation angle response than with lift response. Consistently, generalized $\mathcal{H}_2$-norms associated with these candidate locations (see Table 6) are greater than their lift counterparts. This is especially prominent for the higher ranked locations in the separation angle case.

In order to explain the physical mechanisms underlying these differences, we conduct controllability analyses of the flowfield by leveraging the dynamic mode decomposition with control algorithm [101]. These modal analyses of flowfield response data reveal that excitation of coherent structures in the wake benefit lift control; whereas, excitation of coherent structures in the shear layer benefit separation-angle control.

The most controllable flow structures for actuator location $x/c = 0.2$ and $x/c = 0.3$ are shown in Figure 46. Unlike the most controllable DMD modes, the most controllable flow structures identified by this Gramian-based analysis

are not associated with just a single-frequency; rather, these structures can exhibit rich dynamics that are associated with evolution along the most controllable direction in state-space. As such, the controllable subspace reveals a different description of control mechanisms than the modal controllability analysis. The optimal actuator location for lift control appears to activate vortex shedding in the wake, starting immediately at the trailing edge of the airfoil. This is consistent with the modal controllability analysis for actuation at $x/c = 0.2$. The fact that the wake is most sensitive to actuation at $x/c = 0.2$ is also consistent with physical intuition, since the transfer of bound vorticity into free vortcity in the wake is the physical mechanism for lift production.

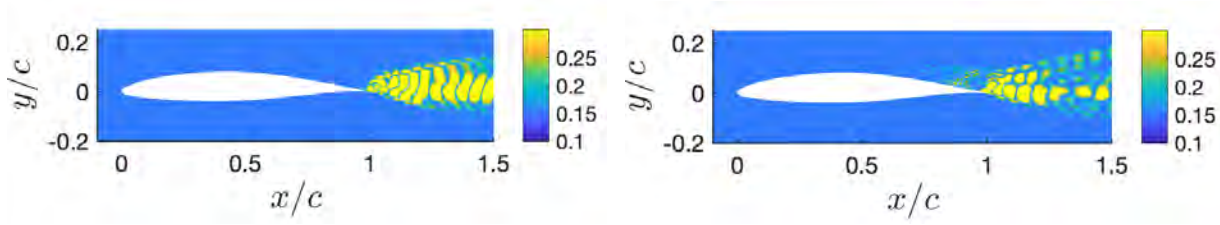

(a) $x/c = 0.2$ (b) $x/c = 0.3$

Figure 46: The magnitude of the first principal direction of the generalized controllability Gramian associated with actuation at $x/c = 0.2$ and $x/c = 0.3$, visualized using vorticity.

10 Conclusion and Outlook

Significant progress was made towards the development of an optimal Lagrangian flow based controller for external airfoil and wing aerodynamics. Primary contributions were made in three closely connected studies, that include

- A detailed benchmarking and study of a cambered airfoil, chosen based on practical application in turbomachinery, at low to moderate Reynolds number, using a mutual validation of computation with first-principle models and accurate experiments.
- Development and testing of a comprehensive theory and description of Lagrangian flow separation in unsteady external flows.
- Development of a theory for the identification of an optimal control of flow separation.

We discuss contributions made in each area followed by open questions that remain.

10.1 DNS and Experiment

This work paid close attention to the matching of equivalent experiment and DNS, both of which used state-of-the-art techniques. We found no agreement between any experiment in the literature at $Re = 5 \times 10^4$, or between current results, though we believe our data are the first to make sufficiently accurate measurements combined with computations over a broad range of parameters for genuine comparison. It turns out that aerodynamics at a particular range of Re, when laminar boundary-layer separation combines with possible transition to turbulence, are extremely sensitive to small disturbances – or to small differences between conditions in experiment and simulation. This makes direct comparison particularly challenging, and important, because these same sensitivities are responsible for abrupt changes in integrated quantities such as lift and drag, which in turn can be tracked down to variation in detailed separation line kinematics.

The primary focus was in testing and cross-checking of the flows around the NACA 65(1)-412 airfoil, which is important in turbine blade arrays.At lower α, the flow separates at around mid-chord and encloses a large region of recirculating fluid over the leeward wing section. A characteristic pattern of vortices is shed from the trailing edge and the flow transitions to a turbulent wake. With increasing α, instabilities develop in the separated shear layer, then break down and transition to turbulence over the wing itself. The time-averaged flow state is characterized by a laminar separation bubble with complete reattachment, and it is responsible for an abrupt increase in lift and decrease in drag as the time-averaged streamlines reattach and minimize wake losses. Experimentally, we show that this transition (which we have previously denoted an SI – SII transition [102]) occurs within a 0.3° range of α. We denote the center of this range as $\alpha_{textrmcrit}$.

The value of α_{crit} was not the same in experiment and computation. Numerous experimental and computational test cases were run to verify the result for varying spans, varying Mach number, and varying grid resolution. The computational result was robust to these changes. The experiment was not, and α_{crit} varies according to background turbulence levels (water channel vs. wind tunnel) and according to aspect ratio. AR in a wing with endplates will only be a parameter if end conditions are affecting the global flow transition.

Importantly, marginally resolved DNS of the compressor blade with aspect ratio $AR = 3$ and endwalls show that the flow develops large-scale three-dimensional structures within the separated region. It does this within a few convection times as disturbance propagate rapidly towards mid-span. The separation line shows a distinct spanwise curvature and oscillations that are absent in the simulations with periodic boundaries. These induced wall effects are significantly larger than the boundary layer thickness that develops along the transverse wall and decrease the lifting force substantially. The results indicate that approximately only one third of the wing shows flow conditions that resemble a quasi-periodic state. Having shown that the endplate condition can be far from the idealised two-dimensional equivalent, the further correct physical modelling of experimental wall conditions is perhaps not a very useful enterprise. A recommendation for future work is that focus should be on a geometrically-well specified finite wing, in both experiment and numerics.

The flow states before and after $alpha_{\text{crit}}$ were the same, as judged by both integrated force measurements and by streamline and separation line geometry. An equivalent experiment can be run in different physical or computational arrangements through specifying an equivalent $alpha_{\text{crit}}$. This equivalence can sensitively tested and checked through the geometry of the Lagrangian Particle fields, and the FTLE ridges that separate the different regions, and extensive work was performed in this area.

10.2 The Kinematics of Lagrangian Separation

We have investigated kinematic aspects of flow separation in external aerodynamics by extracting the initial motion of upwelling fluid material from the wall and its relation to the long-term attracting manifolds in the flow field. While the wall-bounded kinematics are governed by the formation of a material spike upstream of the asymptotic separation point and ejection of particles in direction of the separation line, we show that the off-wall trajectories of the fluid tracers are driven by attracting ridges in the finite-time Lyapunov exponents. We have therefore obtained the complete pathway of Lagrangian flow separation - from the initial upwelling at the spiking point over ejection of particles along the asymptotic separation profile to the attracting LCSs.

For the flow around a circular cylinder and a cambered NACA 65(1)-412 airfoil, we extract the footprint of initial material upwelling, the spiking points, by evaluating the curvature of Lagrangian fluid tracers and by extracting high-order on-wall derivatives of the normal velocity as proposed in [91]. An exact match of the Lagrangian and Eulerian criterion for the start of material line spiking verifies the Eulerian criterion and associated the principal location of material upwelling for the first time in test two test cases, i.e. the cylinder flow and the flow over an airfoil. For the latter, we recover the spiking point by appropriately filtering the spurious oscillations in the velocity derivative induced by the spline-based boundary parametrization of the NACA profile and show that this method is robust to noise. Determining the spiking points requires the extraction of the high-order derivatives that is challenging for general geometries and in experimental setting as it requires very high-resolution data and an accurate representation of the geometry. Most surprisingly, upwelling occurs well upstream of the asymptic separation point at the averaged zero skin friction location. Initial upwellings can occur one third of a chord upstream from the asymptote. In a circular cylinder for example upweeling occurs in the upstream half of the cylinder. For the NACA airfoil upwelling occurs at 20% chord while the asymptotic separation point is at at 50% chord.

With the ability to compute the birth of separation instantaneously from Eulerian on-wall data, the Lagrangian pathway from the spiking point to the asymptotic separation profile can be used as input parameters for dynamic flow controllers. The behavior of spiking in tubulent flow and three dimensions such as the blade configuration with endwalls is significantly more complicated. In future work, we aim to address the impact of turbulence modeling and geometry inthe application of the fluid spike extraction in unsteady flows and time-averaged flows at high-Reynolds numbers.

10.3 Lagrangian separation points and control

We developed a data-driven approach for determining the actuator location requiring the minimum control energy to drive an output quantity-of-interest. Given input-output response data for a candidate set of actuator locations, the eigensystem realization algorithm was used to extract state-space system descriptions suitable for solving a minimum input energy optimal control problem and computing the generalized $\mathcal{H}_2$-norm for each location. The method only requires access to input-output response data, making it relevant for numerical and experimental studies alike. The

method was used to investigate the optimal actuator location for airfoil separation control using data from high-fidelity numerical simulations of the NACA 65(1)-412 airfoil, with $\alpha = 4$ and $Re_c = 20,000$. Lift and separation angle response data to a pulse of localized body force actuation were used to determine the optimal location among a candidate set of six locations on the upper surface of the airfoil. It was found that the location $x/c = 0.2$ was optimal for controlling lift, whereas the location $x/c = 0.3$ was found to be optimal for controlling separation angle. This finding was made independent from the discovery of the early upwelling in Lagrangian separation that occurs at approximately the same location. It is hard to imagine this a coincidence and we hope to explore this connection in future work.

The analysis also revealed that the separation angle is more sensitive than lift to actuation from the associated optimal location, making separation angle the more attractive quantity to regulate in separation control applications. In order to identify physical mechanisms underlying these results, we presented a data-driven framework for conducting controllability analysis of the flowfield using dynamic mode decomposition with control (DMDc). A controllability analysis of the dominant single-frequency DMD modes confirmed greater controllability for the actuator placed at $x/c = 0.3$, which was the optimal location for separation angle control. Actuation from this location was found to excite flow structures within the shear layer, corroborating previous findings on the effectiveness of shear layer excitation for separation control. A complementary analysis of the controllable subspaces in the flowfield dynamics confirmed that coherent structures in shear layer were most sensitive to actuation applied at the optimal location for separation control ($x/c = 0.3$). In contrast, coherent structures in the wake were most sensitive to actuation applied at the optimal location for lift control ($x/c = 0.2$). The methods introduced in this paper are generally applicable for optimal actuator selection and controllability analysis.

A distinctive feature of the proposed optimal actuator selection method is that it is entirely data-driven. The approach does not require access to primal or adjoint simulations, which are often required to conduct similar analyses. This makes for a convenient analysis procedure that can be used to objectively assess the optimal actuator location from available or easy-to-acquire response data. Further, the data-driven nature of the method also makes it generally applicable, and should benefit investigations of other flow control configurations as well.

10.4 Open questions

The work objectives changed as challenges and unexpected opportunities emerged. Though data-driven control that was consistent with Lagrangian descriptions of the flow was demonstrated, it was not framed explicitly in terms of LCS, or LCS wall-signatures. Now we know much better what such wall signatures look like, then this possibility is open. The signatures requiring higher-order wall derivatives will clearly not be open to experiment, but we now know how certain integrated quantities from sensors that extend into the flow (such as hair sensors) might be used.

The potential for open loop control of the aerodynamics at these Reynolds numbers has been demonstrated but we have not yet arranged for closed-loop, optimised feedback control. Given the groundwork laid out here, this should be now within reach.

Finally, we have exposed some important fundamental differences that will underly any sufficiently detailed and careful comparison of experiment and numerical simulation at these extremely sensitive Reynolds numbers. The sensitivities act as both diagnostic and as control point. Though the sensitivity is extreme at this range of Re, the flow phenomena are general, and the lessons learned here will apply to areas where there is initially laminar flow, flow separation, and/or transition to turbulence. Few practical flows contain none of these conditions, and this work on the basic physical mechanisms and analysis, we feel has a great future. An extension to finite wings and to other canonical separated flows (cavities, delta wings) would be equally fruitful.

References

[1] M. Gad-el-Hak. *Flow Control: Passive, Active, and Reactive Flow Management*. Cambridge University Press, Cambridge, United Kingdom, 2000.

[2] D. R. Williams and D. G. MacMynowski. Brief history of flow control. In R. D. Joslin and D. N. Miller, editors, *Fundamentals and Applications of Modern Flow Control*, chapter 1, pages 1–20. American Institute of Aeronautics and Astronautics, Reston, VA, 2009.

[3] H. Schlichting and K. Gersten. *Boundary-Layer Theory*. Springer-Verlag, New York, 1999.

[4] L. N. Cattafesta and M. Sheplak. Actuators for active flow control. *Annual Review of Fluid Mechanicas*, 43:247–272, 2011.

[5] Roberto Sosa, Guillermo Artana, Eric Moreau, and Gérard Touchard. Stall control at high angle of attack with plasma sheet actuators. *Experiments in fluids*, 42(1):143–167, 2007.

[6] Jesse Little and Mo Samimy. High-lift airfoil separation with dielectric barrier discharge plasma actuation. *AIAA journal*, 48(12):2884–2898, 2010.

[7] JH Mabe, FT Calkins, B Wesley, R Woszidlo, L Taubert, and I Wygnanski. Single dielectric barrier discharge plasma actuators for improved airfoil performance. *Journal of Aircraft*, 46(3), 2009.

[8] C. Cerretelli and K. Kirtley. Boundary layer separation control with fluidic oscillators. *Journal ofTurbomachinery*, 131(4), 2009.

[9] J. Gregory and M. N. Tomac. A review of fluidic oscillator development. *AIAA Paper 2013-2474*, 2013.

[10] René Woszidlo and Israel Wygnanski. Parameters governing separation control with sweeping jet actuators. *AIAA Paper 2011-3172*, 2011.

[11] J. H. Seo, F. Cadieux, R. Mittal, E. Deem, and L. Cattafesta. Effect of synthetic jet modulation schemes on the reduction of a laminar separation bubble. *Phys. Rev. Fluids*, 3(3), March 2018.

[12] F. Ostermann, R. Woszidlo, C. N. Nayeri, and C. O. Paschereit. The interaction between a spatially oscillating jet emitted by a fluidic oscillator and a crossflow. *Journal of Fluid Mechanics*, 2018.

[13] Michael Amitay, Barton Smith, and Ari Glezer. Aerodynamic flow control using synthetic jet technology. *36th AIAA Aerospace Sciences Meeting and Exhibit*, 1998.

[14] Michael Amitay, Douglas R. Smith, Valdis Kibens, David E. Parekh, and Ari Glezer. Aerodynamic Flow Control over an Unconventional Airfoil Using Synthetic Jet Actuators. *AIAA Journal*, 39(3), March 2001.

[15] Ari Glezer and Michael Amitay. Synthetic Jets. *Annual review of fuid mechanics*, 34(1), 2002.

[16] Michael Amitay, Barton Smith, and Ari Glezer. Aerodynamic flow control using synthetic jet technology. In *36th AIAA Aerospace Sciences Meeting and Exhibit*, 1998.

[17] Ari Glezer and Michael Amitay. Synthetic jets. *Annual review of fluid mechanics*, 34(1):503–529, 2002.

[18] Maziar Hemati, Eric Deem, Matthew Williams, Clarence W Rowley, and Louis N Cattafesta. Improving separation control with noise-robust variants of dynamic mode decomposition. In *54th AIAA Aerospace Sciences Meeting*, page 1103, 2016.

[19] E.A. Deem, L.N. Cattafesta, H. Yao, M.S. Hemati, H. Zhang, and C.W. Rowley. Experimental implementation of modal approaches for autonomous reattachment of separated flows. In *AIAA Aerospace Sciences Meeting*, pages AIAA Paper 2018–1052, 2018.

[20] JH Seo, F Cadieux, R Mittal, E Deem, and L Cattafesta. Effect of synthetic jet modulation schemes on the reduction of a laminar separation bubble. *Physical Review Fluids*, 3(033901), 2018.

[21] S. Yarusevych, J. Kawall, and P. E. Sullivan. Airfoil performance at low Reynolds numbers in the presence of periodic disturbances. *Journal of fluids engineering*, 128(3), 2006.

[22] D. Postl, W. Balzer, and H. Fasel. Control of laminar separation using pulsed vortex generator jets: Direct numerical simulations. *Journal of Fluid Mechanics*, 676, 2011.

[23] O. Marxen, R.B. Kotapati, R. Mittal, and T. Zaki. Stability analysis of separated flows subject to control by zero-net-mass-flux jet. *Physics of Fluids*, 27(2), 2015.

[24] S. Yarusevych and M. Kotsonis. Steady and transient response of a laminar separation bubble to controlled disturbances. *Journal of Fluid Mechanics*, 813, 2017.

[25] R. Raju, R. Mittal, and L. Cattafesta. Dynamics of airfoil separation control using zero-net mass-flux forcing. *AIAA Journal*, 46(12), 2008.

[26] Rajat Mittal and Rupesh B Kotapati. Resonant mode interaction in a canonical separated flow. In *IUTAM Symposium on Laminar-Turbulent Transition*, pages 341–348. Springer, 2006.

[27] Rajat Mittal, Rupesh Kotapati, and Louis Cattafesta. Numerical study of resonant interactions and flow control in a canonical separated flow. In *43rd AIAA Aerospace Sciences Meeting and Exhibit, AIAA 2005-1261*, 2005.

[28] Chi-An. Yeh and Kunihiko Taira. Resolvent-analysis-based design of airfoil separation control. *Journal of Fluid Mechanics*, 867:572–610, 2019.

[29] Kunihiko Taira, Maziar S. Hemati, Steven L. Brunton, Yiyang Sun, Karthik Duraisamy, Shervin Bagheri, Scott T. M. Dawson, and Chi-An Yeh. Modal analysis of fluid flows: Applications and outlook, 2019. arXiv:1903.05750.

[30] Eric A Deem, Louis N Cattafesta, Hao Zhang, Clarence W Rowley, Maziar Hemati, Francois Cadieux, and Rajat Mittal. Identifying dynamic modes of separated flow subject to znmf-based control from surface pressure measurements. In *47th AIAA Fluid Dynamics Conference*, pages AIAA Paper 2017–3309, 2017.

[31] Maziar S Hemati, Clarence W Rowley, Eric A Deem, and Louis N Cattafesta. De-biasing the dynamic mode decomposition for applied koopman spectral analysis of noisy datasets. *Theoretical and Computational Fluid Dynamics*, 31(4):349–368, 2017.

[32] R. L. Simpson. Turbulent boundary layer separation. *Ann. Rev. Fluid Mech.*, 21:205–232, 1989.

[33] Vladimir V. Sychev, Anatoly I. Ruban, Victor V. Sychev, and Georgi L. Korolev. *Asymptotic Theory of Separated Flows*. Cambridge University Press, 1998.

[34] H. Schlichting and K. Gersten. *Boundary-Layer Theory*. Springer-Verlag, New York, 1999.

[35] G. Haller. Exact theory of unsteady separation for two-dimensional flows. *J. Fluid Mech.*, 512:357–311, 2004.

[36] M. Weldon, T. Peacock, G.B. Jacobs, M. Helu, and G. Haller. Experimental and numerical investigation of the kinematic theory of unsteady separation. *J. Fluid Mech.*, 611:1–11, 2008.

[37] George Haller. Determining material surfaces and coherent structures in three-dimensional fluid flows. *Physica D*, 149:248–277, 2001.

[38] G. Haller. Finding finite-time invariant manifolds in two-dimensional velocity fields. *Chaos*, 10:99, 2000.

[39] G. Haller. Lagrangian coherent stuctures from approximate velocity data. *Phys. Fluids*, 14:1851, 2006.

[40] George Haller. A variational theory of hyperbolic Lagrangian Coherent Structures. *Physica D*, 240(7), March 2011.

[41] S. C. Shadden, F. Lekien, and J. E. Marsden. Definition and properties of Lagrangian coherent structures from finite-time Lyapunov exponents in two-dimensional aperiodic flows. *Physica D*, 212:271–305, 2005.

[42] Bjoern F. Klose, Gustaaf B. Jacobs, and Mattia Serra. The kinematics of lagrangian flow separation in external aerodynamics. *AIAA Journal (submitted)*, 2019.

[43] G. B. Jacobs. *Numerical Simulation of Two-Phase Turbulent Compressible Flows with a Multidomain Spectral Method.* PhD thesis, University of Illinois at Chicago, 2003.

[44] G. B. Jacobs, D. A. Kopriva, and F. Mashayek. A comparison of outflow boundary conditions for the multidomain staggered-grid spectral method. *Num. Heat Transfer, Part B*, 44:225–251, 2003.

[45] G. B. Jacobs, D. A. Kopriva, and F. Mashayek. Validation study of a multidomain spectral element code for simulation of turbulent flows. *AIAA J.*, 43(6):1256–1264, 2004.

[46] G. B. Jacobs, D. A. Kopriva, and F. Mashayek. A conservative isothermal wall boundary condition for the compressible Navier-Stokes equations. *J. Sci. Comp.*, 30(2):177–192, 2005.

[47] H. Abassi, F. Mashayek, and G.B. Jacobs. Shock-capturing with entropy-based artificial viscosity for staggered-grid discontinous spectral element method. *Computers & Fluids*, 2014.

[48] K. Sengupta, G.B. Jacobs, and F. Mashayek. Large eddy simulation using a high-order nodal discontinuous Galerkin method on unstructured grids. ASME Paper IMECE-2006-16050, American Society for Mechanical Engineers, 2006.

[49] K. Sengupta, G.B. Jacobs, and F. Mashayek. Direct simulation of turbulent flows using spectral methods. AIAA Paper 2008-1450, American Institute of Aeronautics and Astronautics, 2008.

[50] K. Sengupta, B. Shotorban, G.B. Jacobs, and F. Mashayek. Spectral-based simulations of particle-laden, turbulent flow. *Int. J. Multiphase Flow*, 35(9), 2009.

[51] H. Kanchi, K. Sengupta, G.B. Jacobs, and F. Masahayek. Large-Eddy Simulation of compressible flow over backward-facing step using Chebyshev multidomain method. AIAA Paper 2009-0922, 2010.

[52] Jan S. Hesthaven and Tim Warburton. *Nodal Discontinuous-Galerkin Methods: Algorithms, Analysis, and Applications*. Springer, New York, 2008.

[53] D.A. Kopriva. *Implementing Spectral Methods for Partial Differential Equations*. Springer-Verlag, Berlin, 2009.

[54] M. Zabat, S. Farascaroli, F.K. Browand, M. Nestlerode, and J. Baez. Drag measurements on a platoon of vehicles. Technical Report UCB-ITS-PRR-93-27, California Partners for Advanced Transit and Highways (PATH), Inst. of Transportation Studies, Univ. of California, Berkeley, CA, 1994.

[55] G.R. Spedding and J. McArthur. Span efficiencies of wings at low Reynolds number. *J. Aircraft*, 47:120–128, 2010.

[56] A. Surana, G.B. Jacobs, and G Haller. Extraction of separation and reattachment surfaces from 3d steady shear flows. *AIAA J.*, 45:1290–1302, 2007.

[57] G.B. Jacobs, A. Surana, T. Peacock, and G. Haller. Identification of flow separation in three and four dimensions. AIAA Paper AIAA-2007-401, American Institute of Aeronautics and Astronautics, 2007.

[58] A. Surana, G.B. Jacobs, O. Grunberg, and G. Haller. An exact theory of three-dimensional fixed separation in unsteady flows. *Phys. Fluids*, 20(10), 2008.

[59] M. Weldon, T. Peacock, G.B. Jacobs, M. Helu, and G. Haller. Experimental and numerical investigation of the kinematic theory of unsteady separation. *J. Fluid Mech.*, 2007. submitted.

[60] E. A. Thomson. Mit solves 100-year-old engineering problem: insights on fluid flow could impact fuel efficiency. 2008. MIT news press release.

[61] Tecplot. Tecplot 360 helps scientists better understand flow separation and shed new light on century-old issues in the identification of flow separation. 2009. Contours Newsletter-http://www.tecplot.com/showcase/contours/article.aspx?issue=47&article=1.

[62] M. Kilic, G.B. Jacobs, G. Haller, and J.S. Hesthaven. Reduced Navier-Stokes equations near a flow boundary. *Physica D*, 217(2):161–185, 2006.

[63] Gustaaf. B. Jacobs. Inertial Particle Behavior in an Unsteady Separated Flow. 46th AIAA Aerospace Science Meeting and Exhibit, January 9 2008. Reno.

[64] G.B. Jacobs and K. Armstrong. Inertial particle dispersion in the lagrangian wake of a square cylinder. AIAA Paper AIAA-2009-1026, American Institute of Aeronautics and Astronautics, 2009.

[65] D. Nelson and G.B. Jacobs. Dg-ftle: Lagrangian coherent structures with higher-order discontinous galerkin methods. *Journal of Computational Physics*, 2015. to appear.

[66] Daniel A. Nelson and Gustaaf B. Jacobs. DG-FTLE: Lagrangian Coherent Structures with High-Order Discontinuous-Galerkin Methods. *Journal of Computational Physics*, 295:65–86, August 2015.

[67] David A. Kopriva. *Implementing Spectral Methods for Partial Differential Equations*. Springer, New York, 2009.

[68] Gregor J. Gassner, Andrew R. Winters, Florian J. Hindenlang, and David A. Kopriva. The br1 scheme is stable for the compressible navier–stokes equations. *Journal of Scientific Computing*, Apr 2018.

[69] P. Roe. Approximate Riemann solvers, parameter vectors, and difference schemes. *Journal of Computational Physics*, 135(2):250–258, 1997.

[70] G. Gassner and D. A. Kopriva. A comparison of the dispersion and dissipation errors of gauss and gauss–lobatto discontinuous galerkin spectral element methods. *Society for Industrial and Applied Mathematics*, 33(5):2560–2579, 2011.

[71] D. A. Kopriva and G. Gassner. On the quadrature and weak form choices in collocation type discontinuous Galerkin spectral element methods. *Journal of Scientific Computing*, 44(2):136–155, 2010.

[72] G. J. Gassner, A. R. Winters, and D. A. Kopriva. Split form nodal discontinuous Galerkin schemes with summation-by-parts property for the compressible Euler equations. *Journal of Computational Physics*, 327:39–66, 2016.

[73] Sergio Pirozzoli. Numerical Methods for High-Speed Flows. *Annual Review of Fluid Mechanics*, 43:163–194, 2011.

[74] J. McArthur. *Aerodynamics of Wings at Low Reynolds Number*. "Ph.D. Tthesis", Department of Aerospace and Mechanical Engineering, University of Southern California, Los Angeles, CA, 2007.

[75] S. L. Yang and G. R. Spedding. *J. Aircraft*, 50:791—797, 2013.

[76] J.B. Barlow, W. H. Rae, and A. Pope. *Low-Speed Wind Tunnel Testing*. Wiley, 1999.

[77] Bjoern F. Klose, Gustaaf B. Jacobs, and David A. Kopriva. Assessing standard and kinetic energy conserving discontinuous galerkin formulations for marginally resolved navier-stokes flows. *Computers & Fluids (submitted)*, 2019.

[78] Daniel A. Nelson, Gustaaf B. Jacobs, and David A. Kopriva. Effect of Boundary Representation on Viscous, Separated Flows in a Discontinuous-Galerkin Navier-Stokes Solver. *Theoretical Computational Fluid Dynamics*, 30:363–385, March 30 2016.

[79] Bjoern F. Klose, Gustaaf B. Jacobs, Joseph Tank, and Geoffrey Spedding. Low Reynolds number airfoil aerodynamics: three different flow patterns within an angle of attack range of four degrees. *AIAA AVIATION Forum*, 2018.

[80] Joseph Tank, Bjoern F. Klose, Gustaaf Jacobs, and Geoffrey R. Spedding. Computer and laboratory studies on the aerodynamics of the naca 65(1)-412 at reynolds number 20 000. Aiaa scitech 2019 forum, 2019.

[81] Daniel Alan Nelson. *High-Fidelty Lagrangian Coherent Structures Analysis and DNS with Discontinuous-Galerkin Methods*. PhD Thesis, University of California, San Diego in conjuction with San Diego State University, San Diego, CA, Month unknown 2015. http://escholarship.org/uc/item/2cv4f732.

[82] L. E. Jones, R. D. Sandberg, and N. D. Sandham. Direct numerical simulations of forced and unforced separation bubbles on an airfoil at incidence. *Journal of Fluid Mechanics*, 602:175–207, 2008.

[83] Ponnampalam Balakumar. Direct numerical simulation of flows over an naca-0012 airfoil at low and moderate reynolds numbers. *AIAA Fluid Dynamics Conference*, 47, June 2017.

[84] H. Shan, L. Jiang, and L. Chaoqun. Direct simulation of flow separation around naca 0012 airfoil. *Computers & Fluids*, 34:1096–1114, 2005.

[85] Miguel R. Visbal. Numerical investigation of deep dynamic stall of a plunging airfoil. *AIAA Journal*, 49(10):2152–2170, 2011.

[86] Wei Zhang, Wan Cheng, Wei Gao, Adnan Qamar, and Ravi Samtaney. Geometrical effects on the airfoil flow separation and transition. *Computers & Fluids*, 116:60 – 73, 2015.

[87] M. Gageik, I. Klioutchnikov, and H. Olivier. Comprehensive mesh study for a direct numerical simulation of the transonic flow at rec = 500,000 around a naca 0012 airfoil. *Computers & Fluids*, 122:153 – 164, 2015.

[88] S.M. Hosseini, R. Vinuesa, P. Schlatter, A. Hanifi, and D.S. Henningson. Direct numerical simulation of the flow around a wing section at moderate reynolds number. *International Journal of Heat and Fluid Flow*, 61:117 – 128, 2016.

[89] A. Chaudhuri, G.B. Jacobs, W.S. Don, H. Abbassi, and F. Mashayek. Explicit discontinuous spectral element method with entropy generation based artificial viscosity for shocked viscous flows. *J. Comp. Phys.*, 32:99–117, 2017.

[90] Nicholas J. Georgiadis, Donald P. Rizzetta, and Christer Fureby. Large-eddy simulation: Current capabilities, recommended practices, and future research. *AIAA Journal*, 48(8), August 2010.

[91] Mattia Serra, Jerome Vetel, and George Haller. Exact theory of material spike formation in flow separation. *Journal of Fluid Mechanics*, 845:51–92, June 25 2018.

[92] Ketan Mittal, Som Dutta, and Paul Fischer. Nonconforming schwarz-spectral element methods for incompressible flow. *Computers and Fluids*, 191:104237, 2019.

[93] C. Williamson. Vortex dynamics in the cylinder wake. *Ann. Rev. Fluid Mech.*, 28:477–539, 1996.

[94] M. P. Rockwood and M.A. Green. Real-time identification of vortex shedding in the wake of a circular cylinder. *AIAA J.*, 57(1):223–238, 2019.

[95] Kamran Mohseni, Doug Lipinski, and Blake Cardwell. A Lagrangian Analysis of a Two-Dimensional Airfoil with Vortex Shedding. *Journal of Physics A: Mathematical and Theoretical*, 41(34):1–22, August 11 2008.

[96] Martin H. Kamphuis, Gustaaf B. Jacobs, Kevin K. Chen, Geoffrey Spedding, and Harry W. M. Hoeijmakers. Pulse Actuation And Its Effects On Separated Lagrangian Coherent Structures For Flows Over A Cambered Airfoil. *Proceedings of the ASME 2017 International Design Engineering Technical Conferences & Computers and Information in Engineering Conference*, November 2017.

[97] Debraj Bhattacharjee, Bjoern Klose, Gustaaf B. Jacobs, and Maziar S. Hemati. Data-driven selection of actuators for optimal control of airfoil separation. *Theoretical and Computational Fluid Dynamics (submitted), pre-print, arXiv:1910.04937*, 2019.

[98] K. K. Chen and C. W. Rowley. Heuristics for effective actuator and sensor placement in feedback flow control. In R. King, editor, *Active Flow and Combustion Control*, volume 127 of *Notes on Numerical Fluid Mechanics and Multidisciplinary Design*, pages 115–130. Springer International Publishing Switzerland, 2014.

[99] J.-N. Juang and R. S. Pappa. An eigensystem realization algorithm for modal parameter identification and model reduction. *J. Guid. Control Dyn.*, 8:620–627, 1985.

[100] Kemin Zhou, Gregory Salomon, and Eva Wu. Balanced Realization and Model Reduction for Unstable Systems. *International Journal of Robust and Nonlinear Control*, 9:183–198, 1999.

[101] Joshua L Proctor, Steven L Brunton, and J Nathan Kutz. Dynamic mode decomposition with control. *SIAM Journal on Applied Dynamical Systems*, 15(1):142–161, 2016.

[102] S.L. Yang and G.R. Spedding. Spanwise variation in circulation and drag of wings at moderate Reynolds number. *J. Aircraft*, 50:791–797, 2013.